UNIVERSITAT
POLITÈCNICA
DE VALÈNCIA

Signal Modality Characterization: from Phase Space Reconstruction to Real Applications

Doctoral Thesis

by

Alicia Carrión García

Supervisor:

Prof. Ramón Miralles Ricós

Valencia, Spain
June 2018

Abstract

The characterization of the modality of a signal is a new concept, which has been the subject of recent research. Its main purpose is to identify any changes in the nature of a real signal. The term 'nature of a signal' refers to the underlying model that generates the signal from the point of view of two main characteristics: determinism and linearity. In this thesis, the modality of a signal is used for the advanced processing of acoustic signals, and in particular, in non-destructive tests of non-homogeneous materials, such as concrete.

The problem of the characterization of the modality begins with the correct reconstruction of the phase space (Chapter 2). This new domain allows identifying the different states of a signal, as to whether they are recurrent or not, depending on whether they are deterministic, respectively, random. In the field of non-destructive testing based on ultrasound, the material is excited with a purely deterministic signal. However, the nature of the received signal depends on the internal structure of the material. This working hypothesis allows us to propose measuring the degree of determinism as a complementary alternative to the usual ultrasound parameters such, as attenuation and speed. The level of determinism has been found to be proportional to the level of porosity in cementitious materials (Chapter 3). It also allows characterizing the level of damage of mortar test pieces subjected to different kinds of damaging processes: external attack by sulphates, and loading processes (Chapter 4).

The study of the non-linearity or complexity of a time series is initially presented blindly (without having information about the input signal) through hypothesis tests: generating surrogate data and applying a statistical test. Significant progress has been made in adapting this approach to non-stationary data, a common feature of real non-linear signals. The main results in this regard have been achieved in the characterization of the complexity of oscillatory signals of limited duration (Chapter 5).

The concept of signal modality has also been used to perform a detailed study of the non-linear phenomenon of acoustic impact spectroscopy. This analysis has allowed understanding the variables involved, and thus, proposing a mathematical model that characterizes the phenomenon. The understanding of the phenomenon and the model have allowed proposing a new

processing algorithm equivalent to the usual NIRAS technique, but optimal in its application. This processing alternative may mean significant advances, especially in industrial applications where time and effort are variables to be optimized (Chapter 6).
This thesis demonstrates that the characterization of the modality of a signal not only presents an alternative to the characterization of complicated real phenomena, but it also opens a new research perspective within the field of signal processing. The measure of determinism and the FANSIRAS algorithm have shown that the modality of a signal is an interesting tool for future research into the characterization of cementitious materials.

Keywords: Signal Modality, Determinism, Non-linearity, Recurrence Plots, Recurrence Quantification Analysis, Delay Vector Variance, surrogates, Non-Destructive Testing, concrete, damage, FANSIRAS

Resumen

La caracterización de la modalidad de la señal es un nuevo concepto objeto de recientes trabajos de investigación cuyo principal propósito es identificar cambios en la naturaleza de señales reales. Con el término naturaleza de las señales se hace referencia al modelo subyacente que genera una señal desde el punto de vista de dos características principales: determinismo y linealidad. En esta tesis se emplea la modalidad de la señal para el procesado avanzado de señales acústicas, y en particular, en ensayos no destructivos de materiales no homogéneos como el hormigón.

El problema de la caracterización de la modalidad comienza con la correcta reconstrucción del espacio de fases (Capítulo 2). Este nuevo dominio permite identificar los diferentes estados de una señal, recurrentes o no en función de su naturaleza determinista o aleatoria, respectivamente. En el ámbito de los ensayos no destructivos basados en ultrasonidos, el material se excita con una señal puramente determinista, sin embargo, la naturaleza de la señal recibida depende y es proporcional a la estructura interna del material. Esta hipótesis de trabajo permite plantear la medida del grado de determinismo como una alternativa complementaria a parámetros habituales de ultrasonidos como la atenuación y la velocidad. El nivel de determinismo ha resultado ser proporcional al nivel de porosidad en materiales cementantes (Capítulo 3). También permite la caracterización del nivel de daño de probetas de mortero sometidas a diferentes procesos de daño: ataque externo de sulfato y procesos de carga (Capítulo 4).

El estudio de la no linealidad/ complejidad de una serie temporal se plantea inicialmente de forma ciega (sin tener información de la señal de entrada) mediante tests de hipótesis: generando datos surrogados y aplicando un test estadístico. Importantes avances se han logrado adaptando este enfoque a datos no estacionarios, característica habitual de señales no lineales reales. Los principales resultados en este sentido se han conseguido en la caracterización de la complejidad de seales oscilatorias de duración limitada (Capítulo 5).

El concepto de la modalidad de la señal también se ha empleado para realizar un detallado estudio del fenómeno no lineal de espectroscopía acústica por impacto. Este análisis ha permitido entender las variables involucradas y plantear así un modelo matemático que caracterice el fenómeno. La com-

prensión del fenómeno y el modelo han permitido plantear un nuevo algoritmo de procesado equivalente a la técnica habitual NIRAS, pero óptimo en su aplicación. Esta alternativa de procesado puede suponer significativos avances sobre todo en aplicaciones industriales donde el tiempo y el esfuerzo son variables óptimas (Capítulo 6).
Esta tesis demuestra que la caracterización de la modalidad de la señal no solo supone una alternativa a la caracterización de complejos fenómenos reales, sino que abre una nueva perspectiva de trabajo dentro del ámbito del procesado de señal. La medida del determinismo y el algoritmo FANSIRAS han demostrado que la modalidad de la señal es una interesante herramienta para futuros trabajos de caracterización de materiales cementantes.

Palabras Clave: Modalidad de la señal, Determinismo, No Linealidad, Representaciones Recurrentes, Cuantificación de Recurrencias, Vector de Varianzas Retardadas, datos surrogados, Ensayos No Destructivos, hormigón, daño, FANSIRAS

Resum

La caracterització de la modalitat del senyal és un nou concepte, objecte de recents treballs de recerca amb el propòsit d'identificar canvis en la natura de senyals reals. Amb el terme natura dels senyals es fa referència al model subjacent que genera un senyal des del punt de vista de dues característiques principals: determinisme i linealitat. En aquesta tesi es fa servir la modalitat del senyal per al processament avançat de senyals acústics i, en particular, en assajos no destructius de materials no homogenis com ara el formigó.

El problema de la caracterització de la modalitat comença amb la correcta reconstrucció de l'espai de fase (Capítol 2). Aquest nou domini permet identificar els diferents estats d'un senyal, recurrents o no en funció de la seva natura determinista o aleatòria, respectivament. Dins l'àmbit dels assajos no destructius basats en ultrasons, el material s'excita amb un senyal purament determinista, tanmateix, la natura del senyal rebut depèn i és proporcional a l'estructura interna del material. Aquesta hipòtesi de treball permet plantejar la mesura del grau de determinisme com una alternativa complementària a paràmetres habituals dels ultrasons com ara l'atenuació i la velocitat. El nivell de determinisme ha resultat ésser proporcional al nivell de porositat en materials cementants (Capítol 3). També permet la caracterització del nivell de dany de provetes de morter sotmeses a diferents processos de dany: atac extern de sulfat i processos de càrrega (Capítol 4).

L'estudi de la no linealitat/ complexitat d'una sèrie temporal es planteja inicialment de forma cega (sense tindre cap informació del senyal d'entrada) mitjançant tests d'hipòtesi: generant dades subrogades i aplicant un test estadístic. Avanços importants s'han aconseguit adaptant aquest enfoc a dades no estacionàries, característica habitual de senyals no lineals reals. Els principals resultats en aquest sentit s'han aconseguit en la caracterització de la complexitat de senyals oscil·latoris de durada limitada (Capítol 5).

El concepte de modalitat del senyal també s'ha emprat per realitzar un detallat estudi del fenomen no lineal d'espectroscòpia acústica per impacte. Aquesta anàlisi ha permet entendre les variables involucrades i plantejar llavors un nou algoritme de processament equivalent a la tècnica habitual NIRAS, però òptim en la seva aplicació. Aquesta alternativa de processa-

ment pot suposar significatius avanços sobretot en aplicacions industrials, on el temps i l'esforç són variables òptimes (Capítol 6).
Aquesta tesi demostra que la caracterització de la modalitat del senyal no solament suposa una alternativa a la caracterització de complexes fenòmens reals, sinó que obri una nova perspectiva de treball dins l'àmbit del processament de senyal. La mesura del determinisme i l'algoritme FANSIRAS han demostrat que la modalitat del senyal és una ferramenta interessant per a futurs treballs de caracterització de materials cementants.

Paraules Clau: Modalitat del senyal, Determinisme, No Linealitat, Representacions Recurrents, Quantificació de Recurrències, Vector de Variàncies Retardades, dades subrogades, Assajos No Destructius, formigó, dany, FANSIRAS

To my family

Acknowledgements

En primer lugar, me gustaría agradecer la oportunidad brindada por mi director de tesis, Prof. Ramón Miralles Ricós. Agradezco su trabajo, dedicación y generosidad ante todos los retos que nos han surgido a lo largo de estos años. Además, me gustaría hacer una mención especial al Prof. Jorge Gosálbez Castillo, quien también me ha guiado y enseñado su saber hacer.

Esta tesis no habría alcanzado su máxima aplicación sin la excelente colaboración mantenida con el GIQUIMA-ICITECH, en particular, con el Prof. Jordi Payá Bernabeu y Vicente Genovés Gómez. Sin duda, junto a ellos se ha logrado demostrar la sinergia perfecta que supone la ciencia multidisciplinar.

I would also like to thank Prof. Danilo Mandic, who hosted me at Imperial College of London. I really appreciate the opportunity he gave me and his kind support during the months I spent working with his team. I am also very grateful to Prof. J. Ramis from the Universidad de Alicante, Prof. J. S. Popovics from the University of Illinois and Prof. I. Cornel from the GIPSA-Lab for serving as reviewers of this thesis.

En el largo camino que supone la realización de una tesis doctoral juega un papel fundamental el ecosistema que rodea al investigador. Agradezco encarecidamente el apoyo recibido siempre y por todo el Grupo de Tratamiento de Señal (GTS-iTeAM). Son infinitas la cantidad de anécdotas vividas, y que, por supuesto, forman parte de este trabajo. Gracias a Guille y Gonzalo por acompañarme todo el tiempo. A los que estuvieron: Jorge Moragues, Arturo, Patricia, Elena, David, Guille Pérez y Jose Vicente. Y a los que están: Santi, Jordi, Carles, América y Nacho.

Por último, me gustaría agradecer y dedicar este trabajo a mi familia: mis padres, Juan Benito y Esther, y mis hermanos, Juan Francisco y Ana Esther. Ellos son mi motivación por querer seguir avanzando cada día. Esta tesis va también dedicada a la persona que me acompaña cada día y cuya confianza en mí no flaquea en ningún instante. Gracias Pascual por enseñarme a vivir la ciencia.

Contents

Introduction and Objectives 1

1.1 Background

The term signal modality is employed to refer to the different techniques and algorithms which can be used to gain information about the nature of a signal and the underlying model which gives rise to it. In this thesis, the study of the modality of a signal has mainly focused on two particular features: determinism and linearity. Thus, this new concept tries to identify the different regions of the hypothetical two-dimensional space defined by these two features. The range of signals defined to date, based on their levels of determinism and linearity, are summarized in Figure 1.1 [1], [2]. In this scheme there are small well known regions that tend to be the extremes of nature, namely, the purely non-linear deterministic signals (chaos), or the random and linear signals represented by the autoregressive moving average models (ARMA). However, these extremes do not cover most of the real-world signals, and unknown horizons remain. The presence of factors, such as different sources of noise, leads to the fact that most of the real-world signals appear in the still unknown areas of Figure 1.1, for example, those indicated by the signs (a), (b), and (c). The level of stationarity in a signal might also be studied as a modality feature. However, in this thesis, non-stationarity has been considered as the result of external artefacts, and not

as much a particular characteristic of the system (i.e. changes in the path travelled by the signal, channel fading, amplitude modulation, etc.).

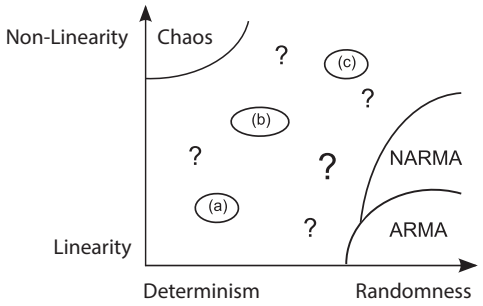

Figure 1.1. Distribution of real world signals according to their deterministic/random nature vs. linear/non-linear nature [1], [2].

The applications of signal modality are becoming increasingly significant in signal processing and machine learning. Knowing this type of information can facilitate the selection of the most appropriated model, avoiding unnecessary complexity. To date, the study of the nature of a signal has provided great advances in biomedical applications through the analysis of electroencephalographic signals (EEG) and in applications related to meteorological information [3]. However, this new paradigm is not common in acoustic applications, nor in non-destructive inspection techniques.

Most physical phenomena can be modelled as the response of a system to an excitation. Under this approach, the excitation corresponds to a input signal $x(t)$, with $y(t)$ the response of the system to that input signal or excitation. A traditional ultrasonic inspection layout is represented in the following scheme in terms of a system:

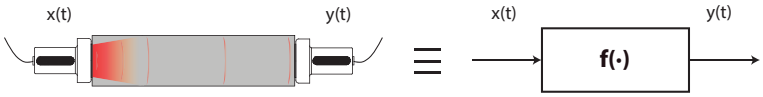

Figure 1.2. Traditional ultrasonic layout represented in terms of a system.

Thus, the concept of the system $\mathbf{f}(\cdot)$ may be seen as the mathematical expression which describes the relation between the excitation input, $x(t)$, and the output $y(t) = \mathbf{f}(x(t))$.

A system is said to be deterministic when no randomness is involved in the response to the input signal. In a deterministic model, thus, the output can be mathematically predicted given the excitation, and it always produces the same output from a given starting condition or initial state. Otherwise, the system is said to be random. Therefore, an output response signal $y(t)$ is deterministic when it comes from a deterministic system.

The definition of non-linear system may be studied as the absence of linearity. The theory of linear systems has been widely used in several areas of engineering since they model a multitude of physical phenomena (propagation, reverberation, filters ...) and they are perfectly characterized by their impulse response $h(n)$. In order to see whether a system is linear or not, we need to test whether it obeys certain rules that all linear systems obey. The two main properties of linearity are homogeneity and additivity, which taken together, are referred to as the principle of superposition. Given a linear system $\mathbf{f}(\cdot)$, whose input is $x(t)$ and output $y(t)$, the properties may be enunciated as follows:

- Homogeneity: A scaling by α of the input signal is reflected in the output signal's being scaled by α as well. This property may also be called the scalar rule of linear systems (Fig. 1.3).

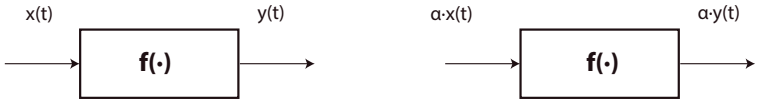

Figure 1.3. Graphical representation of the homogeneity property of linear systems.

- Additivity: An input obtained as the sum of two inputs, $x_1(t)+x_2(t)$, results in an output equivalent to the sum of the two outputs obtained from each input separately, $y_1(t) + y_2(t)$ (Fig. 1.4).
- Superposition: This is the result of the combination of the two previous properties.

Throughout this thesis, we use the phrase degree of determinism (or linearity) to refer indistinctly to the signal under study, or to the system which it comes from.
Different approaches can be taken to the problem of characterizing the

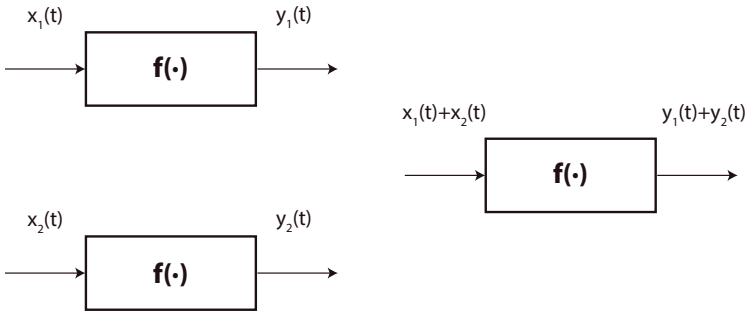

Figure 1.4. Graphical representation of the additivity property of linear systems.

modality of a signal, depending on whether we can gain access to the input and output of the system or only to the output (blind characterization). In many real life situations, having access to the input of the underlying system is not possible (i.e. think about the vibration of the vocal cords in voice production systems), or although the excitation is known, it does not represent the real input due to multipath effects, e.g. the ultrasound (US) inspection of complex structures. In most of this thesis, it is intended to analyse the modality of the signal blindly, that is, not knowing the input signal, which is most of the time not available. For this, it is necessary to reconstruct the phase space of the underlying dynamic system (Chapter 2). This approach is used for the study of the degree of determinism (Chapters 3 and 4) and the linearity/complexity of the signals (Chapter 5). In contrast, the last chapter (Chapter 6) takes a close look at a non-linear application where the system is excited with an impact seen as a Dirac Delta signal ($x(t) = \delta(t)$), and the system does not respect the property of homogeneity.

This work was carried out within a broader research project that unifies the signal processing group (GTS) of the Institute of Telecommunications and Multimedia Applications (ITEAM) and the materials chemistry group (GIQUIMA) of the Institute of Science and Technology of Concrete (ICITECH). This research seeks to find the optimal synergy between both disciplines and institutions by the application of the concept of the modality of the signal to the field of the processing of acoustic signals, and in particular, to the non-destructive tests of concrete.

1.1.1 Non-Destructive testing of non-homogeneous materials

Concrete is a non-homogeneous material that results from the mixture of cement, aggregate, and water. Its use is fundamental in civil engineering. Due to its heterogeneity, its structure presents interfaces between the aggregate and the cement paste, air voids, microcracks, etc., even before suffering any damage. This material is the most important component in buildings and civil structures, where it is exposed to different types of extreme conditions: thermal damage, freeze–thaw cycles, chemical attacks, etc. Its safety and control over its life time is critical.

The standard methods for detecting defects in a concrete structure involve the use of drilled core samples [4]. Some of the traditional methods are strength tests, compressive strength determination, elastic modulus determination, etc. These methods are the most immediate approaches, but have the disadvantage of being strongly biased by the constraints of the procedure, being inexact in terms of the real response of the material. Also, the destructive nature of these methods only allows evaluating a small portion of the structure. Hence, there is a need for researching non-destructive methods for material characterization and damage detection. Owing to their non-invasive nature, non-destructive testing (NDT) appears as a reliable tool for detecting and characterizing different types of damage.

NDT may be classiffied into many different categories, such as visual, magnetic field, electrical, acoustic, etc. [5, 6]. In this thesis, we are going to focus on two of the so-called global methods, which quantify the healthiness of a structure (or part of it) by examining changes in the propagation of ultrasonic waves, or in its vibrational characteristics.

Because of the heterogeneous nature of concrete, scattering phenomena occurs at each interface between the aggregate and the matrix [7]. Thus, ultrasonic waves traveling through concrete are both modulated and attenuated. The most common ultrasonic measurements are the propagation velocity (ultrasonic pulse velocity, UPV) and the ultrasonic waveform attenuation introduced by the material. These parameters have been widely used not only in traditional through-transmission layouts but also in ultrasonic imaging and travel wave tomography [8, 9]. Both the propagation velocity and the attenuation are based on the linear theory of the propagation signal (the frequency components of the emitted pulse and the received pulse are similar). However, the presence of non-linear terms in

the elastic response of a granular medium is considered an indicator related to the presence of any kind of damage. Many techniques have been presented to extract non-linear features from ultrasound, based on many different approaches, such as higher-order harmonics [10], subharmonics [11], and sidebands [12]. Non-linear ultrasonics are also being studied by the Scaling Substraction Method (SSM), a novel technique that allows correlating damage with the loss of linearity based on amplitude scaling in a through-transmission layout [13, 14].

Because of its granular and inhomogeneous structure, concrete can be considered a synthetic rock, with static and dynamic behaviours similar to other materials studied in geophysics and soil engineering. Recent studies have focused on detecting non-linearities in mechanical waves in cementitious materials, due to a sensitivity to damage, including the use of vibration spectroscopy. Non-linear Elastic Wave Spectroscopy (NEWS) techniques are based on the non-linear decreasing of the fundamental frequency with the increasing amplitude of excitation. With these techniques, thermal damage, alkali-silica reactions, sulphate attack, and other distributed damage in concrete have been successfully monitored [15, 16, 17, 18]. Acoustic Emission techniques have also exhibited good results in detecting the focus of microcracking process and the location of flaws when energy is released during mechanical tests [19, 20].

1.2 Objectives

Taking into account the background and the motivation, the main goals of this thesis are the following:

- Making an exhaustive revision of the available approaches for signal modality characterization, particularly, for the different routines to quantify the degree of determinism, linearity, complexity, etc. The proposed concept of signal modality encompass many different concepts that have been traditionally studied, but called by different names.
- Verification of the hypothesis of applying signal modality characterization as a new approach for acoustic signal detection/characterization both on bioacoustic signals, and/or non-destructive testing

experiments. Prior to the beginning of this research, this approach to applications was merely a working hypothesis.

- Delving into the traditional NDT for concrete, as well as their layouts, experimental problems, needs, etc. Getting knowledge about the drawbacks of this field might result in the development of new approaches from the signal processing point of view.

- Application of the knowledge given by the signal modality features for a better understanding of the underlying non-linear phenomena. The signal modality may help the optimization of available signal processing algorithms.

1.3 Organization of the Thesis

This thesis is structured in 7 sections that describe the developed research. It is important to remark that this thesis involves the two aforementioned disciplines, signal processing and acoustics, especially, applied to non-destructive testing. Consequently, it has been deemed appropriate to introduce the basic concepts of both fields in order to ease the reading by specialists in each field. The chapters are arranged and presented as follows:

- Chapter 2: The first part of the chapter contains some preliminaries related to dynamical systems. The concept of phase space and, accordingly, the problem of its reconstruction, is addressed. Furthermore, the signal processing tool known as Recurrence Plots (RP) and the Recurrence Quantification Analysis (RQA) are also reviewed. A new reconstruction approach is raised, applied and compared to the traditional techniques when reconstructing a set of well-known dynamical systems and stochastic processes.

- Chapter 3: This chapter presents a detailed description of some techniques used to estimate the degree of determinism of a signal. Moreover, an alternative index based on higher statistics is also developed. All the methods are applied and compared in the second part of the chapter, where the degree of determinism is presented as an indicator of the porosity of cementitious materials by means of ultrasonic

waves. Finally, the RP based on the angular distance approach is also studied for the characterization of cement pastes.

- Chapter 4: In this chapter, the degree of determinism is evaluated as an indicator for the characterization of damage. A detailed analysis of this new approach is carried out for concrete specimens under an external sulphate attack and different levels of load. Special attention is paid to traditional ultrasonic NDT measures, such as velocity and attenuation, not only for direct measuring configurations but also indirect ones.

- Chapter 5: This chapter addresses the problem of detecting non-linearities. The chapter includes a detailed description of the bootstraping surrogate generation algorithms. Some modifications related to surrogates and a statistical test are proposed to deal with the possible non-stationarities appearing in real data. In addition, a complexity test for short time oscillatory signals is also developed, based on the aforementioned bootstraping method. Finally, it is applied to the characterization of dysphonic dog barking sounds.

- Chapter 6: This chapter contains a detailed analysis of the non-linear phenomenon of the impact spectroscopy of inhomogeneous materials such as concrete. A new method, based on a special windowing, the so-called FANSIRAS, is presented. Additionally, thermal damage NDT experiments are evaluated by means of the traditional resonance procedures and the recently proposed FANSIRAS algorithm.

- Chapter 7: This chapter contains the main conclusions and publications derived from the work developed in this thesis. Finally, some possible lines of future research are given.

2 Phase Space Reconstruction

Phase Space Reconstruction 2

2.1 Introduction

In mathematics, a dynamical system is a function which describes the time dependence of a point in a geometrical phase space. Examples include the mathematical models that describe the swinging of a clock pendulum, the flow of water in a pipe, and population dynamics [21]. For example, at any given instant of time n_0, the dynamical system plotted in Figure 2.1 has a state represented by a point in an appropriate state space, $\vec{X}[n_0] = [x[n_0], y[n_0], z[n_0]]$. The rule for the evolution of the dynamical system describes the future states following the current state, $\vec{X}[n_0 + 1]$.

The phase space (also called the state space) is a finite dimensional vector space $\mathbb{R}^m$ that collects all the possible states of the system useful for determining the future evolution of a signal. A state is specified by a vector of real numbers, $\vec{X} \in \mathbb{R}^m$. Depending on the nature of the time variable, the dynamical system can be classified as:

- A continuous system, where time is a continuous variable and the dynamics are described by an explicit system of m first-order ordinary differential equations:

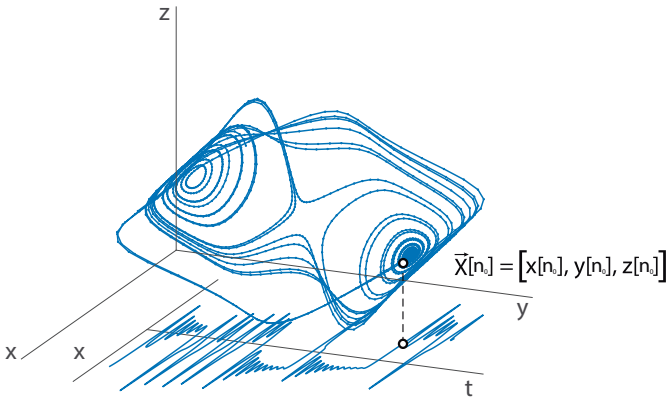

Figure 2.1. Example of a dynamical system, such as the Lorenz attractor: phase space and the data extracted from the values of the x-component.

$$\frac{d}{dt}\vec{X}(t) = \mathbf{f}\left(\vec{X}(t)\right) \tag{2.1}$$

- A discrete system, where time is a discrete variable and the dynamics are described by a discrete $m-$dimensional map:

$$\vec{X}[n+1] = \mathbf{F}\left(\vec{X}[n]\right) \tag{2.2}$$

The functions $\mathbf{f}(\cdot)$, respectively, $\mathbf{F}(\cdot)$ describe the rules for the evolution over time, in the continuous, respectively, discrete domains. In this thesis, the discrete time formulation has been found more convenient, since, after all, time series we have to deal with are given at discrete time steps. Moreover, the numerical integration of differential equations with a finite time step Δt yields a discrete map.

Commonly, what we observe in any experiment is not the set of states that make up the phase space, $\vec{X}[n]$, but a time series, $x[n]$. Most usually, this is a sequence of scalar measurements of some quantity which depends on the current state of the system, $\vec{X}[n]$, taken at multiples of a fixed sampling time, $t_n = n \cdot \Delta t$:

$$x[n] = \mathbf{s}\left(\vec{X}(n \cdot \Delta t)\right) + \eta[n]$$

where $\mathbf{s}(\cdot)$ ($\mathbb{R}^m \to \mathbb{R}$) represents the measurement function through which we look at the experiment and $\eta[n]$ is the measurement noise. Therefore, the time observations must be seen as projections of the underlying dynamical system. In Figure 2.1, the real world observations of the Lorenz attractor can be the x-component of the system.

One of the recurrent problems when dealing with dynamical systems is the reconstruction of the phase space, from which comes the observed real time series. Although this problem has been theoretically solved by the Takens embedding theorem [22], the practical application is still an open issue. Many authors have tried to address this problem from different perspectives [23, 24, 25, 26], however, none of the techniques has established a algorithm robust against the modality of the signal when estimating the optimal reconstruction parameters.

The remainder of this chapter is organised as follows. In Section 2.2, the delay embedding dimension theorem is introduced. Then, a signal processing tool based on the recurrences of the signal is presented in Section 2.3. In Section 2.4, a new reconstruction approach is presented, applied, and compared to the traditional techniques when applied to a set of well-known dynamical systems. Finally, the conclusions are summarized in Section 2.5.

2.2 Delay Embedding Theorem

A delay embedding theorem gives the conditions under which a chaotic dynamical system can be reconstructed from a sequence of observations of the state of a dynamical system. In [27], Deyle provided analytical proofs to generalize the Takens embedding theorem and demonstrated how multiple time series can be used in attractor reconstructions. This work opens a potential growth area for Phase Space Reconstruction (PSR) applications to a wide selection of the applied sciences.

There are two main aspects to the problem of the embedding of scalar data $x[n]$ into some $\mathbb{R}^m$, so as to build the corresponding phase space $\vec{X}[n]$. First, for every time n, there must be constructed m independent variables from the scalar time series. The second aspect is that of finding an embedding of an $m-$dimensional curve into a Cartesian space. This was accomplished in [28]. Whitney proved that every $m-$dimensional smooth manifold can be embedded in $\mathbb{R}^{2m+1}$. The problem of the independent variables was solved

by the theorem of Takens.

Let $\vec{X}[n]$ be the state vector at time n, $\mathbf{s}(\cdot)$ the measurement function, and $\mathbf{F}(\cdot)$ the map representing the dynamics, $\vec{X}[n+1] = \mathbf{F}(\vec{X}[n])$. Then a delay vector is

$$\vec{X}\left[n\right] = \left[\mathbf{s}\left(\vec{X}\left[n\right]\right), \mathbf{s}\left(\mathbf{F}\left(\vec{X}\left[n\right]\right)\right), \mathbf{s}\left(\mathbf{F} \circ \mathbf{F}\left(\vec{X}\left[n\right]\right)\right), \ldots\right]$$

Knowing $x[n] = \mathbf{s}(\vec{X}[n])$ at successive time samples n is equivalent to knowing a set of different coordinates at a single moment if the map $\mathbf{F}(\cdot)$ couples the different degrees of freedom. Finally, for an observed time series $x[n]$, the *delay* state space reconstruction in an m-dimensional space is formed by the delay vectors $\vec{X}_{L,m}[n]$, given by

$$\begin{aligned}\vec{X}_{L,m}\left[n\right] = \left[x\left[n\right], x\left[n-L\right], \ldots, x\left[n-(m-1)\cdot L\right]\right]^T, \\ n = 1, \ldots, N-(m-1)\cdot L\end{aligned} \tag{2.3}$$

where N is the total number of points, L is the time difference, in terms of the number of samples (or in time units, $\tau = L \cdot \Delta t$), between adjacent components (also called the lag or time delay), m is the number of independent components used in the reconstruction, in other words, the embedding dimension, and the superscript T indicates the transpose matrix.

The main problem in the application of the Takens theorem is that it only postulates the existence of the parameters L and m, but does not provide a method to calculate them. The most common procedures used for estimating these parameters are presented below. There are two theoretical concepts associated with the pursuit of the parameters: the concept of mutual information (Section 2.2.1) and the concept of false neighbours (Section 2.2.2).

2.2.1 The Time Delay

The time delay L between successive elements in a delay vector is not a subject of the embedding theorem. Although this choice is arbitrary from the mathematical point of view, in practice, a good choice of L facilitates the analysis. If L is small compared to the internal scale of the system, the

successive elements of the delay vector are strongly correlated. All vectors $\vec{X}[n]$ are then clustered around the diagonal $\mathbb{R}^m$. This is called redundancy [29, 30]. However, if L is very large, successive elements are almost independent and the points fill a large cloud in $\mathbb{R}^m$, but the characteristic structures may be confined to small scales. In this case, the reconstructed attractor may become unnecessarily complicated, even if the true attractor is simpler.

In order to obtain uncorrelated sequences from the observed data, many different approaches have been developed. The first zero of the autocorrelation function, $R\,[L]$, often yields a good approximation.

$$R\,(L) = R\,(x\,[n]\,, x\,[n+L]) = \sum_{i=1}^{N-L} x\,[i] \cdot x\,[i+L]^* \tag{2.4}$$

This well-known function only takes into account the linear relations between the samples. However, when working with chaotic or just non-linear functions, the signal must be uncorrelated not only for second order statistics but also for those of higher order. A more refined version of the autocorrelation function looks for the first local minimum of the time delayed Mutual Information (MI) [31]. Based on Shannon's concept of entropy [32], the mutual information between two delayed sequences, $I(x[n], x[n+L])$, represents the mean number of bits of the time series $x[n+L]$ that can be estimated from $x[n]$. Applying the expression for the mutual information to the time delay reconstruction results in $M[L]$:

$$M(L) = I(x[n], x[n+L]) = \sum_{i=1}^{N-L} P_{x,x}(i, i+L) \cdot log_2 \left[\frac{P_{x,x}(i, i+L)}{P_x(i) P_x(i+L)} \right] \tag{2.5}$$

where $P_x(i)$ is the probability that the signal $x[n]$ assumes a value inside the ith bin of the histogram , and $P_{x,x}(i, i+L)$ is the probability that the signal $x[n]$ assumes a value inside the ith bin of the histogram and the signal $x[n+L]$ is in bin $i+L$.

It is customary to use a fixed resolution for binning the data, although alternative algorithms using adaptive partitioning are also available. Since the interest is in the dependence of $M(L)$ on L, coarse binning is not such

a big issue. In Section 2.4, the mutual information, $M(L)$, of some well-known functions will be analysed.

2.2.2 The Embedding Dimension

The time series obtained by a measurement process is a projection of the unobserved internal variables of the analysed system onto the real axis. Takens's embedding theorem guarantees that there exists a dimension m such that the vectors $\vec{X}[n]$ are equivalent to the phase space. The term equivalent does not imply the reconstruction of the original phase space, but constructing a new space such that the attractor in this space is equivalent to the original one. Under this assumption, several algorithms have been developed to find the optimal embedding dimension m.

There are many different approaches in the literature to determining the optimal embedding dimension. Here, the three main approaches will be described.

- The computation of some invariant of the attractor [23]. The value of the correlation integral, the Lyapunov exponents, and/or entropies, stop changing after a certain dimension m, and these values are then supposed to be identical to those in the original phase space. This approach has the disadvantage of being data intensive and time consuming.

- A singular value decomposition [24]. This approach identifies orthogonal directions in the embedding space visited by the reconstructed trajectory. The main directions are identified by their large singular values and the dimension of the smallest space that contains the trajectory. This identification may depend on the details of the embedding and the accuracy of the data.

- The method of false nearest neighbours (FNN) [33]. This exploits the idea that if an m-dimensional embedding yields a faithful representation of the state space, every $m' > m$ does so as well. This idea, studied locally in the neighbourhood of a single point, means that any two points which are close in the m-dimensional state space will still be close in the $m+1$ dimensional reconstructed space. Such pairs of points are called true neighbours. Otherwise, they are called

false neighbours. Perfect embeddings means that no false neighbours exist.

After analysing the many different approaches, we opted to go deeper into the FNN technique, although here it is presented in a modified version, which avoids any choice of threshold [25]. So far, the variable m has been used to refer to the dimension of the original phase space. Hereinafter, we will analyse the estimation of the equivalent phase space dimension E. An auxiliary variable, denoted by e, will be used in an iteration process.

The implementation of the modified FNN algorithm begins with the phase space reconstruction of the minimum embedding dimension e, $\vec{X}_{L,e}(n)$, and the following one $e+1$, $\vec{X}_{L,e+1}(n)$. The parameter L must be a priori computed no matter what method is used (the mutual information algorithm is suggested). For each vector state $\vec{X}_{L,e}(i)$, the nearest (in the sense of some distance) neighbour $\vec{X}_{L,e}(n(i,e))$ in the e-dimensional space must be found. For each pair of neighbouring points, the following distance must be measured:

$$a(i,e) = \frac{\left\|\vec{X}_{L,e+1}(i) - \vec{X}_{L,e+1}(n(i,e))\right\|_{max}}{\left\|\vec{X}_{L,e}(i) - \vec{X}_{L,e}(n(i,e))\right\|_{max}} \tag{2.6}$$

The authors in [25] suggest the use of the maximum norm:

$$\left\|\vec{X}_{L,e}(i) - \vec{X}_{L,e}(j)\right\|_{max} = \max_{0\leq k\leq e-1} \left\|x_{i+kL} - x_{j+kL}\right\| \tag{2.7}$$

where $\left\|\cdot\right\|$ is the Euclidean distance. Note that $n(i,e)$ in the numerator of Equation 2.6 is the same as that in the denominator, but in a higher dimensional space $(e+1)$. In order to avoid any choice of threshold, the mean value $Q(e)$ of all $a(i,e)$ is defined by

$$Q(e) = \frac{1}{N - e\cdot L}\sum_{i=1}^{N-e\cdot L} a(i,e) \tag{2.8}$$

This quantity is dependent only on the dimension e and the lag L. To investigate its variation from e to $e+1$, $Q1(e)$ is defined:

$$Q1\,(e) = \frac{Q\,(e+1)}{Q\,(e)} \tag{2.9}$$

They found that $Q1\,(e)$ stops changing when e is greater than some value e_0. Then $e_0 + 1$ is the minimum embedding dimension sought for, E. The minimum embedding dimension E is chosen to be when the fraction of false points is smaller than 2%. Recall that the obtained optimal embedding dimension, E, gives us an equivalent phase space, which does not have to be the original m-dimensional phase space. From now on, we refer to the phase space as the equivalent reconstruction computed substituting the embedding parameters (L, E) in Equation 2.3, $\vec{X}_{(L,E)}[n]$.

The parameter L is a parameter which must be given before the minimum embedding dimension is determined numerically, no matter what methods are used. Different values of L may lead to different minimum embedding dimensions, especially for continuous time series. In further examples, different choices will be analysed and the results are not strongly influenced if both parameters are properly computed. For many practical purposes, the most important embedding parameter is the product $E \cdot L$ of the delay time and the embedding dimension, rather than the embedding dimension E or the time delay L alone. The reason is that $E \cdot L$ is the time span represented by an embedding vector. We are discussing the choice of E and L separately but a joint choice can also be done [26]. In this chapter a detailed joint determination of E and L is proposed and discussed.

2.3 Recurrence Plots

From the beginning of this chapter it has been pointed out that the starting point of signal processing are sequences of measured data, which become a phase space after an embedding process. No one has yet described the properties of the optimal phase space, but intuitively all of us are able to identify a correct embedding when looking at the evolution of the *trajectory* of the states in the phase space. Different definitions can be found for the word trajectory:

- In aerodynamics, a trajectory is the path that a moving object follows

through *space as a function of time*.

- In control theory, a trajectory is a *time-ordered set of states* of a dynamical system.
- In discrete mathematics, a trajectory is a *sequence of values* calculated by the iterated application of a mapping $\mathbf{F}(\cdot)$ to an element x.

The three definitions suggest the concept of *states* at different positions as function of *time*. Furthermore, an approximate repetition of a state is called a recurrence: the return of the trajectory in state space to a neighbourhood of a point where it has been before.

In 1987, Eckmann introduced a tool called Recurrence Plots (RP), allowing visualizing the recurrence of states which make up the phase space of a signal $x\,[n]$ [34]. The quantification of the number and duration of the recurrences allows us to study significant properties of the underlying dynamic system: laminar phases [35], unstable periodic orbits [36], etc.
The RP of a signal $x[n]$ begins with the E-dimensional phase space reconstruction, $\vec{X}_{L,E}\,[n]$, discussed in Section 2.2. Among the different variants for computing the RP, the most common way is defining a Distance Plot (DP) matrix based on the Euclidean distance using Equation 2.10:

$$DP\,(n_1, n_2) = ||\vec{X}\,[n_1] - \vec{X}\,[n_2]\,||, \qquad n_1, n_2 = 1, \ldots, N_s \tag{2.10}$$

where N_s is the number of considered states $\vec{X}\,[n]$. One of the main advantages of the RP is that they allow the E-dimensional phase-space trajectory to be investigated through a binary two-dimensional representation of the recurrences of the states. The binary expression is computed by the posterior thresholding (Eq. 2.11):

$$RP\,(n_1, n_2) = \Theta\,(\varepsilon - DP\,(n_1, n_2))\,, \qquad n_1, n_2 = 1, \ldots, N_s \tag{2.11}$$

where ε is a threshold distance, and $\Theta\,(\cdot)$ is the Heaviside step function.

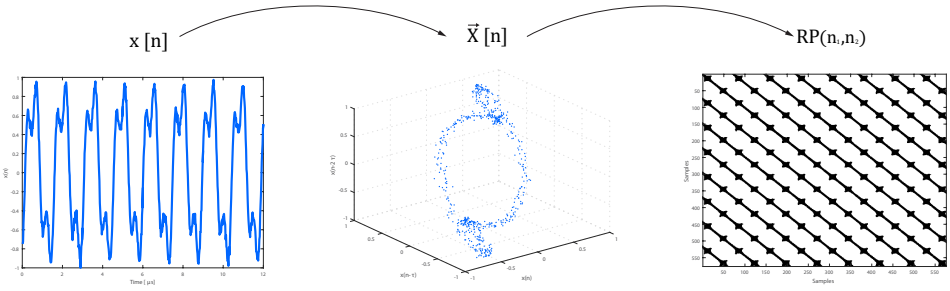

Figure 2.2. Steps of Recurrence Plot analysis: Left) Time representation of the signal $x[n]$; Center) Phase space representation of the signal, $\vec{X}[n]$; Right) Computation of the recurrence plot $RP\,(n_1, n_2)$. In this example, the phase space is obtained using $E = 3$ and $L = 4$.

$$\Theta(x) = \begin{cases} 0 & \text{si} \quad x < 0 \\ 1 & \text{si} \quad x \geq 0 \end{cases}$$

Figure 2.2 summarizes the generic steps of the recurrence plots analysis for a signal $x[n]$. First, the time representation of the signal, $x[n]$. Second, the phase space reconstruction, $\vec{X}[n]$, using the optimal parameters E and L (Eq. 2.3). Third, the computation of the recurrence plot, $RP\,(n_1, n_2)$. At a glance, a characteristic matrix of the 0's and 1's can be seen. Black dots represents the recurrent points, and white dots the non-recurrent points for a fixed point in the time signal (each column).

The recurrence plots exhibit characteristic large-scale and small-scale patterns that are caused by typical dynamic behaviour easily identified as patterns of vertical and diagonal lines (Fig. 2.2). The appearance of vertical black lines (and horizontal lines) means that the trajectory does not change its state for some time [37], whereas the appearance of black diagonal lines is related to a similar local evolution of different parts of the trajectory. Table 2.1 graphically illustrates the appearance of vertical and diagonal lines for continuous and discrete functions. Vertical lines (first row in Table 2.1) may be seen as static relations between a fixed point in the phase space (black dot in the phase space and the corresponding column in the RP) and the rest of the points. Time samples closed in the time domain and in the state domain are identified as vertical lines around the main diagonal (green dots). The rest of the vertical lines correspond

to static positions of the trajectory of the dynamical system in the rest of the time interval (red dots). Diagonal lines allow identifying dynamic relations within a signal: different time intervals similarly evolving in the phase state. In the case of continuous functions (second row in Table 2.1), similar trajectories may be easily identified. However, in the discrete maps (third row), the diagonal structures highlight hidden structures due to the physical distance between consecutive time points. Magenta diagonal lines in the RP represent the dynamical correlations between the green and red points marked in the phase space.

In order to quantify the structures appearing in the RPs, Webber developed Recurrence Quantification Analysis (RQA) [38]. RQA defines measures using the recurrence point density and the diagonal structures in the recurrence plot: the recurrence rate (RR), the average length of the diagonal structures (L_d), and the entropy ($ENTR$) (see Table 2.2). The recurrent points delineate the number of embedded vector pairs that are near each other in the E-dimensional space; however, the measures related to the diagonal patterns distinguish between points individually dispersed and those that represent parts of the signal where it similarly evolves. Gao et al. [40, 41] carried out a detailed analysis of the reasons for the appearance of vertical lines (and horizontal lines for fixed values of ε) and its relation with the appearance of square-like textures in RPs. Marwan et al. [37, 39] extended this to the vertical structures and defined measures of complexity based on the distribution of the lengths of the vertical lines: the percentage of points that form vertical lines, also called laminarity (LAM), and the average length of the vertical lines or Trapping Time (TT) (see Table 2.2). These variables have been widely applied to identify laminar states and their transitions between regular and chaotic regimes [42], as well as to detect the presence of the unstable singularities which are often found in biological dynamics [37, 43]. In this thesis, we have pioneered the use of RPs (and its extension, the RQA) in different fields of science.

2.4 Phase Space Reconstruction based on RQA

In Section 2.2, the traditional methods for determining the optimal embedding parameters were analysed, whereby the optimal time lag L and embedding dimension E are optimised separately. This way, the time lag

Table 2.1. Graphical explanation of the appearance of vertical and diagonal lines in the RPs.

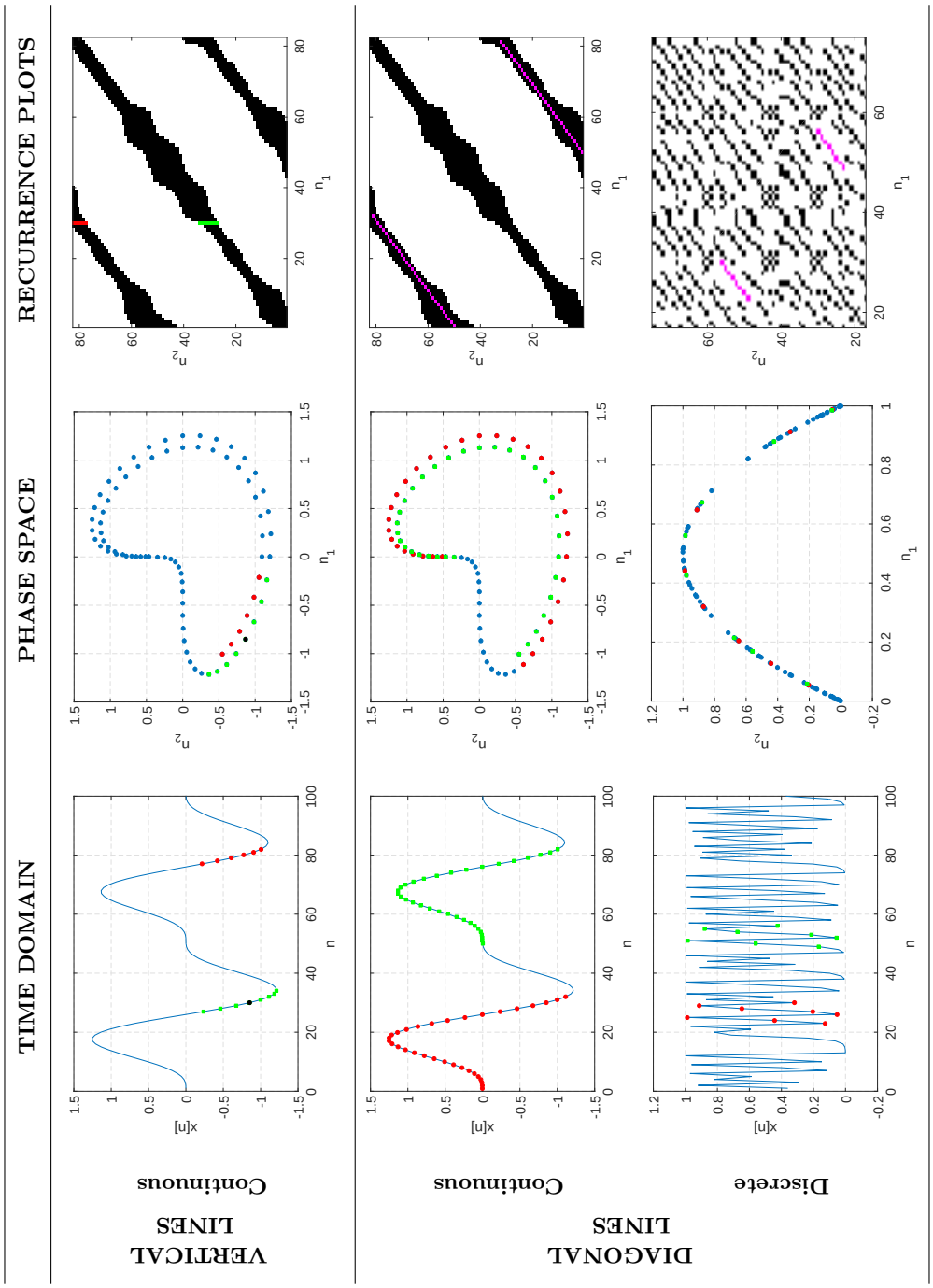

Table 2.2. Some measures for the Recurrence Quantification Analysis (RQA). [37, 38, 39]

SYMBOL	DESCRIPTION	EQUATION
RR	Recurrence rate: density of recurrence points.	$\frac{1}{N^2}\sum_{i,j=1}^{N} R_{i,j}$
L_d	Averaged diagonal line length. [a]	$\frac{\sum_{l=l_{min}}^{N} l \cdot P(l)}{\sum_{l=l_{min}}^{N} P(l)}$ (2.12)
$ENTR$	Shannon entropy of the length of recurrence points that form diagonal lines. [a]	$\sum_{l=l_{min}}^{N} P(l) \cdot lnP(l)$
LAM	Laminarity: Percentage of recurrence points that form vertical lines. [b]	$\frac{\sum_{v=v_{min}}^{N} v \cdot P(v)}{\sum_{v=1}^{N} v \cdot P(v)}$
TT	Averaged vertical line length. [b]	$\frac{\sum_{v=v_{min}}^{N} v \cdot P(v)}{\sum_{v=v_{min}}^{N} P(v)}$ (2.13)

[a] $P(l)$ is the histogram of the lengths l of the black diagonal lines, and l_{min} is the minimal length of what should be considered to be a diagonal line (typically, $l_{min} = 2$).
[b] $P(v)$ is the histogram of the lengths v of the black diagonal lines, and v_{min} is the minimal length of what should be considered to be a vertical line (typically, $v_{min} = 2$).

is first determined as that for which the mutual information between time samples separated by L, that is $x[n]$ and $x[n+L]$, is minimal. Using this optimal L, the optimal embedding dimension is found next based on the FNN algorithm. We refer to the combination of the time delayed mutual information and false nearest neighbour methods as the MI/FNN method. An interpretation of the first step is that the axes of the 2D phase space signal representation are being chosen to be as independent as possible, not necessarily a good criterion if the embedding dimension exceeds two [44]. To this end, we propose a unified and unambiguous optimisation procedure for simultaneously determining both the time lag L and the embedding dimension E, based on the recurrence analysis. The RP allows quantifying the integrity of the trajectories, and therefore, choosing the optimal pair of embedding parameters. Among the different RQA measures available, we have chosen the mean of the vertical lines, TT (Eq. 2.13), the value of the longest vertical line, vL_{max}, and the mean of the diagonal lines, L_d (Eq. 2.12).

In this section, different simulated time series are used to assess the efficiency of the traditional reconstruction algorithms as well as the RQA measures. There is no rule of thumb for all signals' nature when applying the MI/FNN. Therefore, an exhaustive analysis for a representative set of continuous/discrete, deterministic/stochastic signals has been done (see Fig. 2.3). For each simulations, the selection of the minimum embedding dimension E according to the FNN algorithm is chosen as the fraction of false points smaller than 2%, and the threshold (ε) of the RP was chosen to be 50% of the total amount of points making up the RP.

2.4.1 Continuous Functions

The Rössler system, the Lorenz system, the Van der Pol system, and a sum of sinusoidal signals have been considered as the continuous examples. All of them have been discretized using a sample period Δt, so the real time delay τ expressed in time units equals $L \cdot \Delta t$. In order to ease the understanding, the time lag is expressed in discrete terms as the number of samples L.

The Rössler Atractor

The Rössler system defines a chaotic dynamical system associated with the fractal properties of the attractor originally studied by Rössler [45]. In this

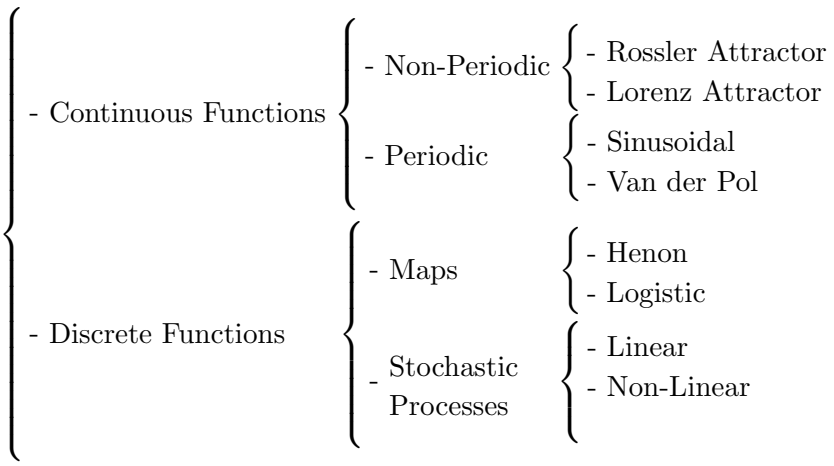

Figure 2.3. Simulated time series studied and their classification taking into account the time variable and their deterministic/stochastic nature.

experiment, we analyse the $\dot{x}$-component of the Rössler equation system:

$$\begin{cases} \dot{x}(t) = -\left(y(t) + z(t)\right) \\ \dot{y}(t) = x(t) + a \cdot y(t) \\ \dot{z}(t) = b + \left(x(t) - c\right) \cdot z(t) \end{cases} \tag{2.14}$$

where $a = 0.2$, $b = 0.2$ and $c = 5.7$. The system is integrated using a 4^{th}-order Runge–Kutta algorithm with integration step $\pi/100$. The first 2000 points are discarded to ensure the vanishing of all transients.

Figure 2.4 shows the application of the MI/FNN method to a 3000-point long simulated Rössler time series. The MI algorithm shows a first local minimum at $L = 32$. The FNN algorithm sets the corresponding optimal value of the embedding dimension $E = 2$.

RQA measures also allow analysing the structure of the reconstructed phase space. The mean and the maximal values of the vertical lines, TT and vL_{max}, respectively, give an idea about the trapping time of the system. On the other hand, the diagonal lines analyse similar trajectories in the phase space. For this example, the TT presents local maxima at different points, indicating that there are several possible pairs of values (L, E) for the reconstruction: (42,2), (30,3), (22,4), (17,5), etc., marked on the

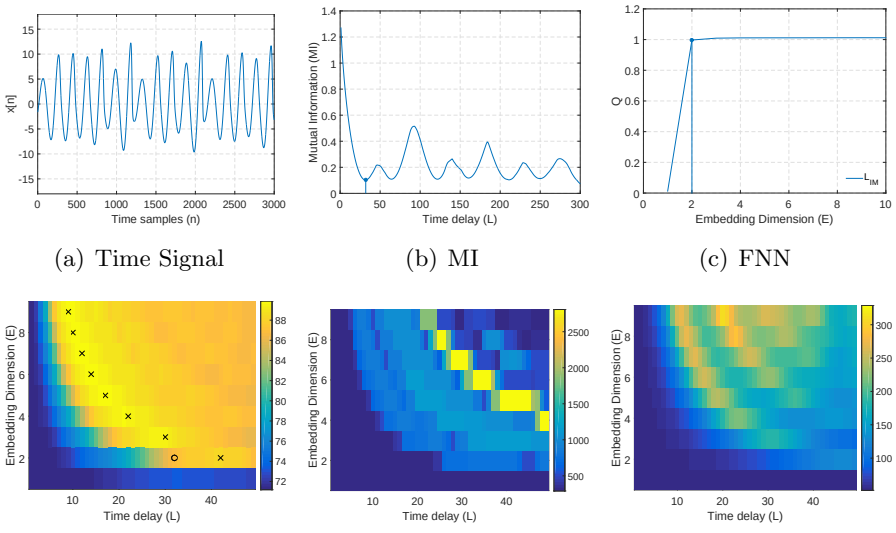

(a) Time Signal (b) MI (c) FNN

(d) RQA/TT (e) RQA/vL$_{max}$ (f) RQA/L$_d$

	L	**E**
MI/FNN	32	2
RQA/TT	30	3

Figure 2.4. PSR analysis of the Rössler Attractor. Data extracted from the values of the $\dot{x}$-component of the Rössler attractor. The table presents the embedding parameters obtained with each method.

RQA/TT diagram with black crosses. Note that the result given by the MI/FNN method (marked with a black circle) approximately coincides with an absolute maximum signalled by the TT measure (30, 3). The maximum vertical line diagram presents a similar trend, but it is easier to find the optimal reconstruction parameters by looking at the TT results. The mean of the diagonal lines also identifies a similar trend, where the values of the local maxima coincide with the values pointed to by the TT measure.

Figure 2.5 compares the reconstructed phase space using the optimal parameters following the MI/FNN algorithm with that obtained from those provided by the TT measure: $(32, 2)$ and $(30, 3)$, respectively. According to the number of independent variables in the Rössler equation system, the

3-dimensional reconstruction allows unfolding new trajectories unidentified in the previous one.

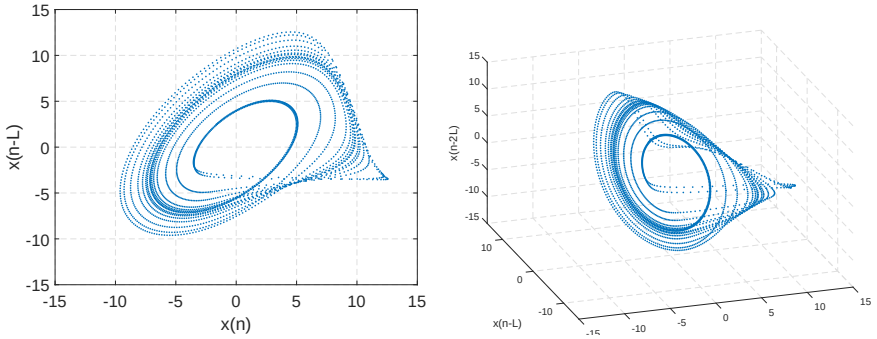

(a) $L = 32$, $E = 2$ (b) $L = 30$, $E = 3$

Figure 2.5. Examples of the Rössler reconstructed phase space.

The Lorenz Attractor

Another well-known chaotic dynamical system is the Lorenz attractor. This chaotic system models the movement of the convection currents in the terrestrial atmosphere [46]. Particularly, the $\dot{x}$-component of the following equation systems has been analysed:

$$\begin{cases} \dot{x}(t) = \sigma\left(y(t) - x(t)\right) \\ \dot{y}(t) = -x(t) \cdot z(t) + \rho \cdot x(t) - y(t) \\ \dot{z}(t) = x(t) \cdot y(t) - \beta \cdot z(t) \end{cases} \tag{2.15}$$

where $\sigma = 10$, $\rho = 28$, and $\beta = 8/3$. The system is integrated using a 4^{th}-order Runge–Kutta algorithm with integration step 0.01 and sampling rate 2, after all transients have diminished.

Figure 2.6 shows the time evolution of the $\dot{x}$-component of the system. The pair of optimal embedding parameters suggested by the MI/FNN method is (10, 3). The RQA/TT measures also identify a group of possible pairs of embedding parameters: (10,3), (9,4), (8,5), (7,6), (5,8). The MI/FNN pair is the lowest dimensional one.

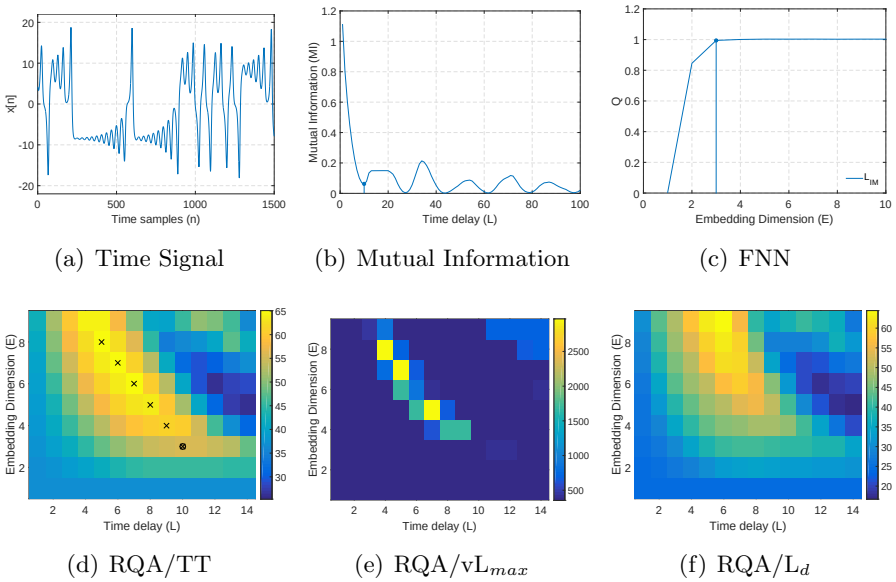

(a) Time Signal (b) Mutual Information (c) FNN

(d) RQA/TT (e) RQA/vL$_{max}$ (f) RQA/L$_d$

	L	**E**
MI/FNN	10	3
RQA/TT	10	3

Figure 2.6. PSR analysis of the Lorenz Attractor. Data extracted from the x-component. The table presents the embedding parameters obtained with each method.

The previous noise-free chaotic systems were easy to reconstruct based on the optimal embedding parameters, since any of their points returned to an arbitrarily small neighbourhood (chaotic behaviour). Next, two strong periodic signals will be studied, in order to truly understand the difficulties in the PSR when similar trajectories appear and are not adequately separated. There is an unwritten law for periodic signals which claims that the optimal time lag L is $T/4$, where T is the period of the signal expressed in terms of the number of samples [47]. In the following examples, both the optimal value of L found by the MI, L_{MI}, and $L_{T/4}$ are analysed.

Sinusoidal Signals

A strong periodic 3000-point signal was generated:

$$x(t) = sin\left(2\pi \cdot f_1 \cdot t + \frac{\pi}{2}\right) + 0.5 \cdot sin\left(2\pi \cdot f_2 \cdot t + \frac{\pi}{2}\right) \tag{2.16}$$

where $f_1 = 1$ Hz and $f_2 = 2f_1$. The discrete time series version $x[n]$ is obtained using a sample period of $\Delta t = 0.01$. The period of the signal T in number of samples is 100, and $T/4$ equals 25.

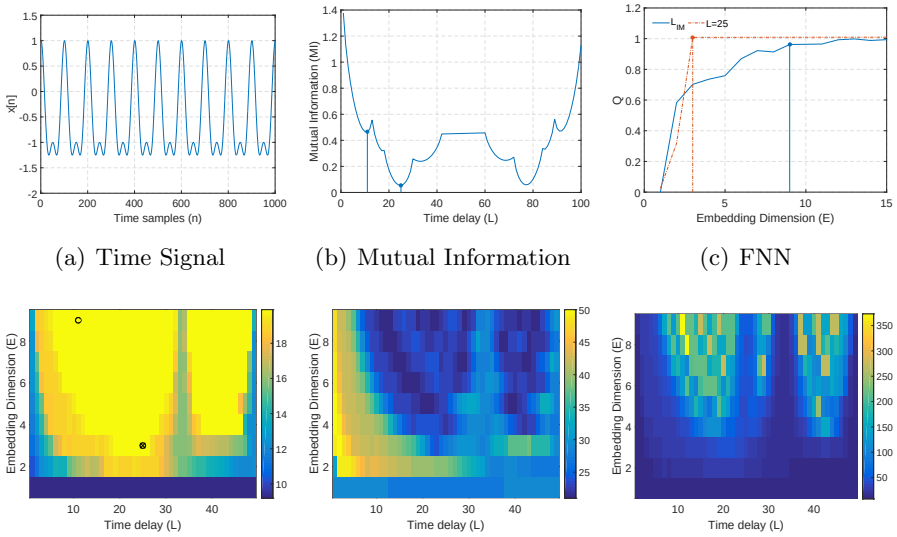

(a) Time Signal (b) Mutual Information (c) FNN

(d) RQA/TT (e) RQA/vL$_{max}$ (f) RQA/L$_d$

	L	**E**
MI/FNN	11	9
L=T/4/TT	25	3
RQA/TT	25	3

Figure 2.7. PSR analysis of a sinusoidal signal. The table presents the embedding parameters obtained with each method.

When analysing a periodic signal, different local minima may appear in the MI analysis. In this case, two local minima are identified in the MI: L_{MI} is 11 and $L_{T/4}$ is 25 (Fig. 2.7(b)). The FNN identifies two different embedding parameters in each case: $L_{MI} = 11$ and $E = 9$; and $L_{T/4} = 25$,

$E = 3$. The RQA/TT measure (Fig. 2.7(d)) clearly identifies the lowest order optimal pair $(25, 3)$, marked with a black cross. The second identified pair (11,9) may also be seen as a maximum but with higher computational cost $(11 \cdot 9 > 25 \cdot 3)$.

In the following section, these results will be contrasted with a strong non-linear periodic signal.

Van der Pol

In dynamics, the Van der Pol oscillator is a non-conservative oscillator with non-linear damping. It evolves in time according to the second order differential equation

$$\begin{cases} \dot{x}(t) = y(t) \\ \dot{y}(t) = \mu y(t)(1 - x(t)^2) - \mu x(t) \end{cases} \tag{2.17}$$

where the $\dot{x}$-component is the position coordinate as function of the time t, and $\mu = 5$ is a scalar parameter indicating the non-linearity and the strength of the damping. The system is integrated using a 4^{th}-order Runge–Kutta algorithm with integration step $\pi/100$. The period of the signal expressed in number of samples is 136, and $T/4$ equals 34.

In this case, two local minima have been identified: L_{MI} is 15 and the previously mentioned $L_{T/4}$ is 34. Applying the FNN algorithm, E is 2 in both cases. The RQA analysis allow understanding the differences between these choices. The TT measure does not identify the first pair (15,2) as a maximum (hollow black circle), but it does so with the second pair (34,2). When studying the maximum length of the vertical lines, the first local minimum in the MI function (15,2) is clearly identified as a maximum. Hence, the differences can be concluded to be related to the statistics of the vertical lines.

Figure 2.9 compares the three PSR: (15,2), (34,2), (21,3). Although at first glance, the three PSRs seem similar (figures in first row), the RPs show different patterns (figures in second row), which are easier to identify in the histograms for the vertical lines (figures in third row). For the case (15,2), the RP pattern does not correspond to a quasi sinusoidal signal where long diagonal lines must predominate; the second case does so but the corresponding histogram seems to identify the two sides of the rectangle

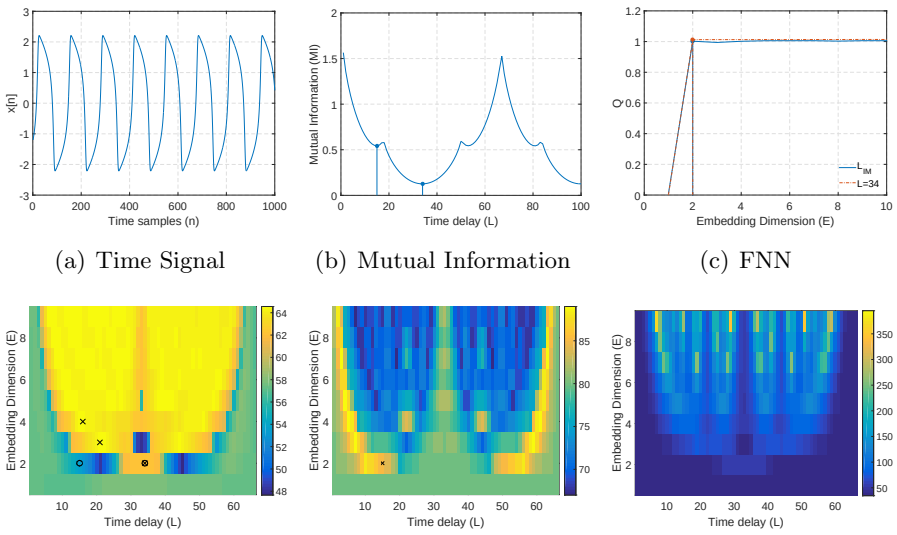

(a) Time Signal (b) Mutual Information (c) FNN

(d) RQA/TT (e) RQA/vL$_{max}$ (f) RQA/L$_d$

	L	**E**
MI/FNN	15	2
L=T/4/TT	34	2
RQA/TT	21	3

Figure 2.8. PSR analysis of the Van der Pol Attractor. Data extracted from the $\dot{x}$-component. The table presents the embedding parameters obtained with each method.

appearing in the phase space, which means that the trajectories are broken at the vertices of the phase space; finally, the third case really shows the right pattern and the histogram shows a maximum in the half of the period of the signal (T/2=68 samples) since the RP threshold is set to correspond with 50% of the points. The FNN algorithm would also have obtained $E = 3$ for L equals 21. However, the MI has not detected that delay as a possible value. According to the expression of the Van der Pol oscillator, there would correspond an embedding of 2, however, the RQA/TT analysis seems to have found an optimal pair which really unfolds the trajectories in the phase space. Both combinations would properly work in future applications where phase space reconstruction is needed.

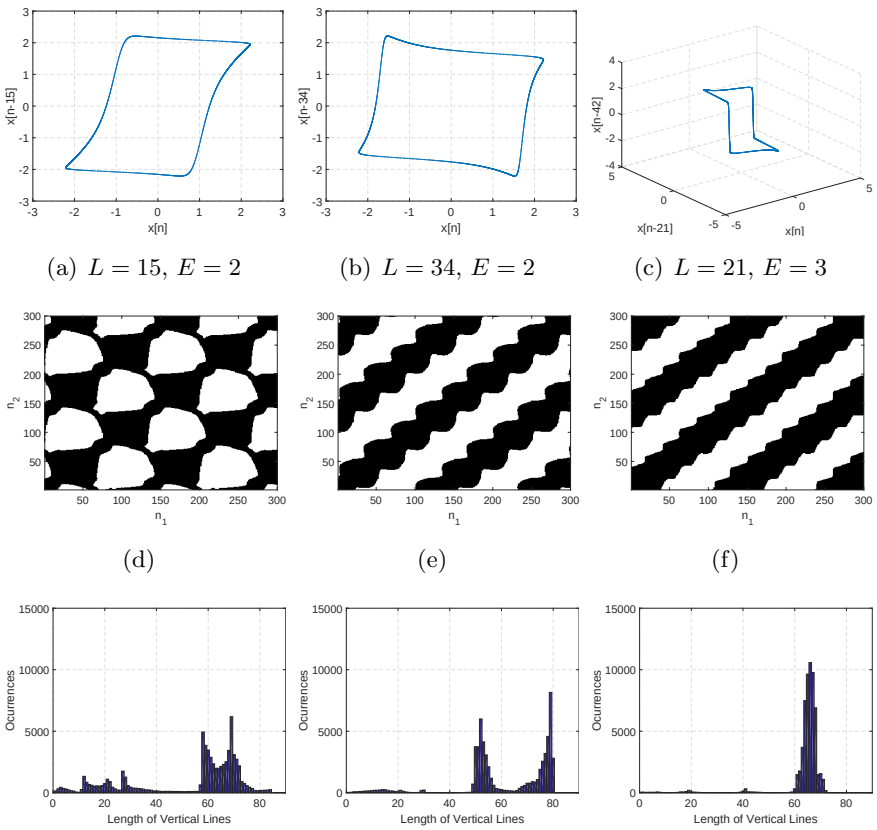

(a) $L = 15$, $E = 2$ (b) $L = 34$, $E = 2$ (c) $L = 21$, $E = 3$

(d) (e) (f)

(g) (h) (i)

Figure 2.9. Van der Pol PSR analysis for different embedding paramters: first column (15,2), second column (34,2) and third column (21,3). First row corresponds to the resulting PSR, second row corresponds to a section of the RP, and third row corresponds to the vertical length histogram.

This analysis suggests that for strong periodic signals, the use of an L equal to one-fourth of the period ($L = T/4$) is an acceptable approximation. However, the analysis of the TT measure may find a different optimal value. In order to easily identify the period of the signals, the use of the autocorrelation function is suggested (Eq. 2.4).

2.4.2 Discrete Maps

We now analyse two deterministic discrete signals, also known as maps; a subgroup of signals which need to be studied in detail to understand its particular dynamics. Theoretically, it would have been thought that in the case of pure discrete signals no vertical lines would appear (no significant static relations), and that the statistics of the diagonal lines would be the criterion to be optimized to identify the optimal embedding parameters. However in this application, an exhaustive search for a fixed number of points in the RP hides potential optimal pairs of reconstruction parameters when looking at the TT measure. Due to the discrete nature of the signal, the literature claims that the time delay must be equal 1 for discrete maps [25]. In this section, the first local minimum of both the MI and L equal to 1 are analysed.

The Henon map

Figure 2.11(a) represents the time evolution of a realization of the Henon map. This deterministic signal is computed from the well-known chaotic Henon map defined by

$$\begin{cases} x[n+1] = 1 - a \cdot x[n]^2 + y[n] \\ y[n+1] = b \cdot x[n] \end{cases} \tag{2.18}$$

where $a = 1.4$ and $b = 0.3$. According to the FNN algorithm, E is 3 when L is 3; and E is 2 when L is 1. RQA analysis suggests that the pairs (1,4) and (1,5) may be possible optimal embedding parameters. In order to understand the differences in terms of the phase space, three reconstructions are plotted in Figure 2.11. The use of the L suggested by the MI algorithm breaks the structure. However, for $L = 1$, simpler trajectories are identified. The TT measure has also identified alternative valid reconstruction parameters without a priori fixing the time lag L to be 1. According to the expression of the Henon map, the combination $L = 1$ and FNN seems the be the optimal option ($E = 2$). The RQA/TT combination seems to be more conservative compared to the FNN algorithm due to the fact that the FNN only takes into account the nearest neighbour (Eq. 2.6).

In this case the analysis of the maximal vertical line does not give too much information. The diagonal lines when L is lower than 3 grow linearly. This is a particular and characteristic behaviour of discrete systems. The

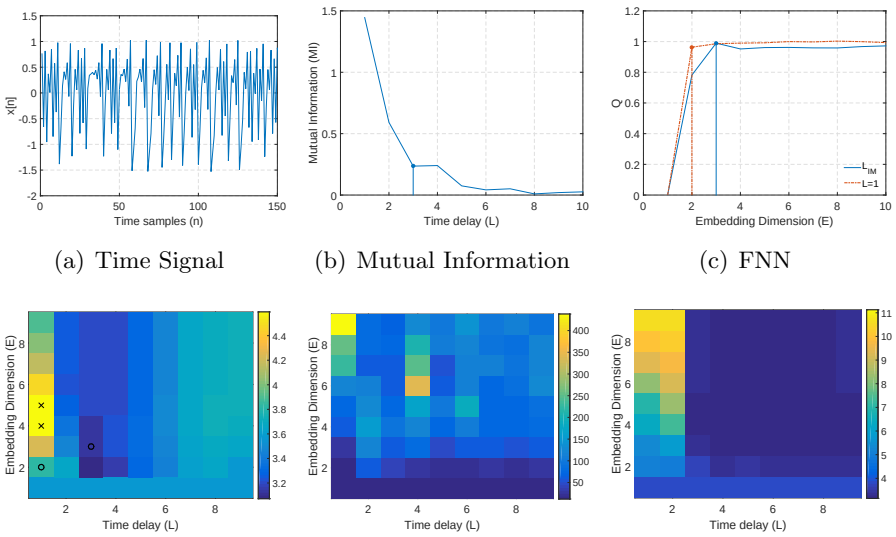

(a) Time Signal (b) Mutual Information (c) FNN

(d) TT (e) vL$_{max}$ (f) L$_d$

	L	**E**
MI/FNN	3	3
L=1/FNN	1	2
RQA/TT	1	4

Figure 2.10. PSR analysis of the Henon Map. The table presents the embedding parameters obtained with each method.

increasing number of dimension implies a larger distance between trajectories closely evolving. Hence, the analysis was done for a fixed percentage of points in the RP: when E is increased, the number of points in the same path is increased, making the average of diagonal lines larger.

The logistic map

The logistic function is given by

$$x[n+1] = a \cdot x[n] \cdot (1 - x[n]) \tag{2.19}$$

where $a = 3.8$ and the initial value $x[0] = 0.23$. This expression results from a simple demographic model that explains that the dynamics of a

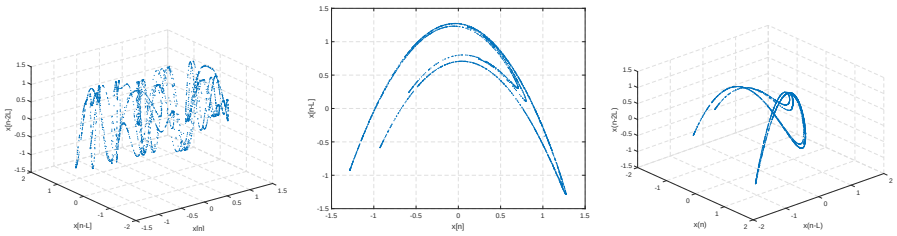

(a) $L = 3$, $E = 3$ (b) $L = 1$, $E = 2$ (c) $L = 1$, $E = 3$

Figure 2.11. Examples of the Henon map reconstructed phase space.

population grows increasingly more slowly as it approaches a number of individuals considered as a limit [21].

As was done in the previous section, two values of L are studied: $L_{MI} = 2$, and $L = 1$. According to the FNN algorithm, E is 2 in both cases. In this case, the TT measure coincides with the optimal pair. However, the maximal vertical length and the diagonal lines do not give any significant information. Note also the high value of the parameter Q in the FNN analysis for $E = 1$ (Eq. 2.9, Fig. 2.12(c)). This is due to the fact that this signal is computed by a single dimensional map.

It can be concluded that for discrete maps, the different sequences used in the phase space reconstruction do not have to be independent components. Despite getting from the MI a value of L different from 1, the optimal value of L for deterministic discrete time series is 1.

2.4.3 Stochastic Processes

Stochastic processes are more complicated to analyse from the perspective of the phase space since a well-defined structure cannot be seen at a glance. It is necessary to apply all the concepts learned from the prior analysis related to deterministic signals. Next, two random signals are analysed: a linear and a non-linear coloured noise signal.

Stochastic processes can be analysed initially as done for maps (Section 2.4.2). However, the presence of strong correlations between samples forces them to be studied as continuous functions where the uncorrelation between sequences is needed (Section 2.4.1). For deterministic continuous signals,

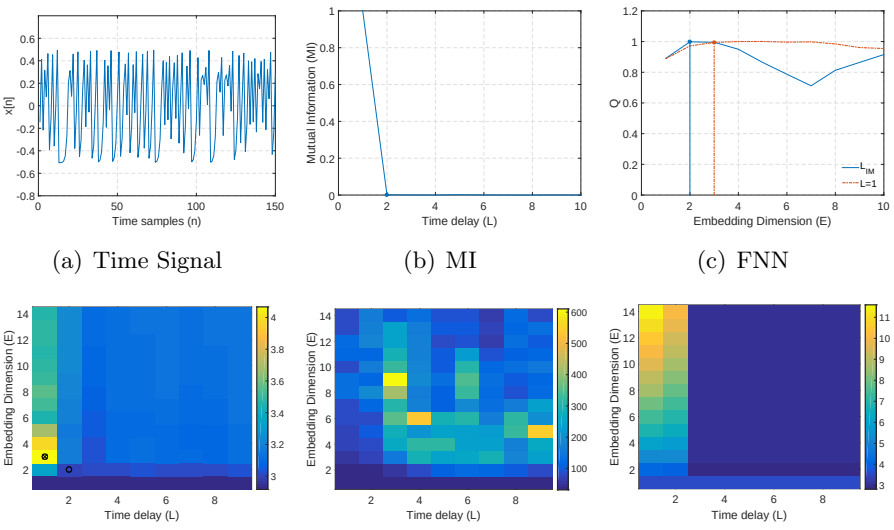

(a) Time Signal (b) MI (c) FNN

(d) TT (e) vL$_{max}$ (f) L$_d$

	L	**E**
MI/FNN	2	3
L=1/FNN	1	3
RQA/TT	1	3

Figure 2.12. PSR analysis of the Logistic Map. The table presents the embedding parameters obtained with each method.

the first local minimum of the MI is a non-null value. However, in the case of stochastic processes, the MI presents a value from which the function becomes null. As in previous studies, the FNN algorithm has been analysed not only for the first local minimum but also for L equal to 1, due to the discrete nature of the signals. The optimal embedding parameter is generally found at higher values of E than in the previous examples since the points are randomly placed and false neighbours are easily found. For the following examples, the RQA measures are plotted in conventional xy graphs instead of using pseudo-colour maps to avoid losing any information due to the high dynamical range of the RQA parameters.

Linear Stochastic Processes

The first stochastic process is a linear correlated signal described by

$$x[n+1] = 1.79 \cdot x[n] - 1.85 \cdot x[n-1] \\ +1.27 \cdot x[n-2] - 0.41 \cdot x[n-3] + \eta[n] \tag{2.20}$$

where $\eta[n]$ is a white Gaussian noise (WGN) of zero mean and unit variance.

The resulting MI is plotted in Figure 2.13(b). Although L equal to 3 seems to be a good approximation, the rule of the first local minimum has been followed. The FNN algorithm has been analysed for L equal to 4 and

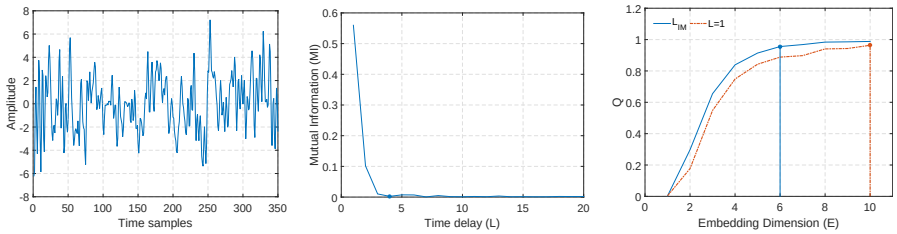

(a) Time Signal (b) MI (c) FNN

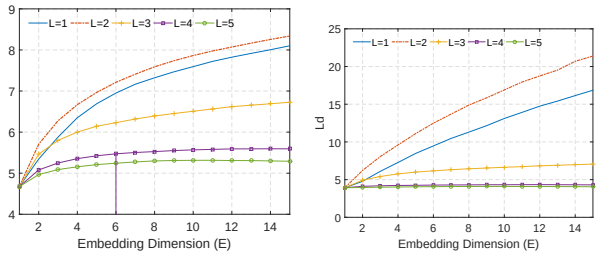

(d) TT (e) L_d

	L	**E**
MI/FNN	4	6
L=1/FNN	1	10
RQA/TT	4	6

Figure 2.13. PSR analysis for a linear correlated stochastic realization. The table presents the embedding parameters obtained with each method.

L equal to 1, and the optimal embedding dimension is found sooner for uncorrelated sequences (higher values of L): $L = 4$, $E = 6$; $L = 1$, $E = 10$.

RQA measures have been analysed for a wide range of values of L, although only the most interesting values have been plotted ($L = 1, L = 2, L = 3, L = 4, L = 5$). A characteristic trend can be seen as the value of the embedding dimension grows. For L equal to 1 and 2, the value of the TT does not stop increasing. However, for L greater than or equal to 3, the TT converges to a maximum value. The optimal value obtained by the FNN approximately coincides with the change in trend found for L equal to 4 and E equal to 6. A similar trend is observed for the mean of the diagonal lines.

Note that the optimal pair of embedding parameters in the previous deterministic signals (Eqs 2.14, 2.15, 2.16, 2.17, 2.18, 2.19) was chosen at the maximum value of the mean of vertical lines (TT). However for random signals, the optimal pair corresponds to the lowest dimensional pair of values where the mean of vertical lines converges. When working with random signals, special care must be taken not to confuse real neighbours in the state space with neighbours wrongly placed due to the correlations between sequences. This is the reason why TT and L_d do not reach a maximum when $L < L_{MI}$.

Figure 2.14 compares two reconstructed phase spaces: $L < L_{MI}$, (1,3); and $L = L_{MI}$, (4,3). Due to the correlations between samples, the cloud

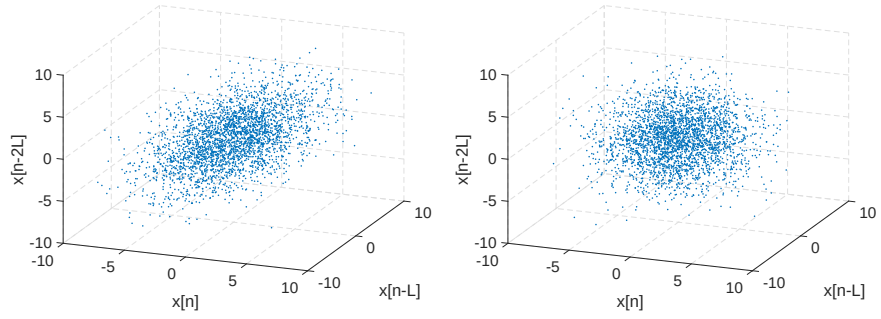

(a) $L = 1$, $E = 3$. (b) $L = 4$, $E = 3$.

Figure 2.14. Linear stochastic process reconstructed phase space.

of points is clustered at the diagonal of the 3-dimensional space and false neighbours are continually found. However, when the sequences are independent, the cloud fills the whole space. Independent components are needed in order to correctly study the nature of the signal.

Non-Linear Stochastic Processes

A non-linear random process has also been analysed:

$$x[n+1] = \frac{x[n-1]^2\,(x[n-1]+2.5)}{1+x[n-1]^2+x[n-2]^2} + \eta[n] \tag{2.21}$$

where $\eta[n]$ is a white Gaussian noise (WGN) of zero mean and unit variance.

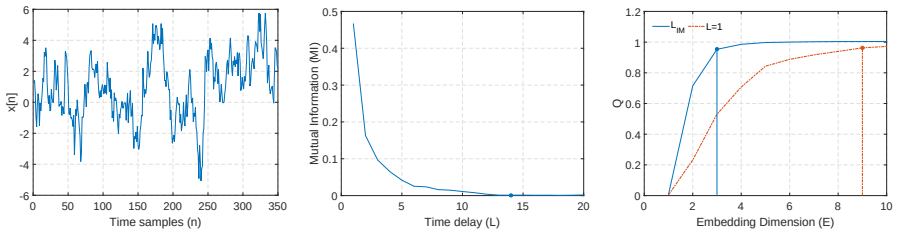

(a) Time Signal (b) MI (c) FNN

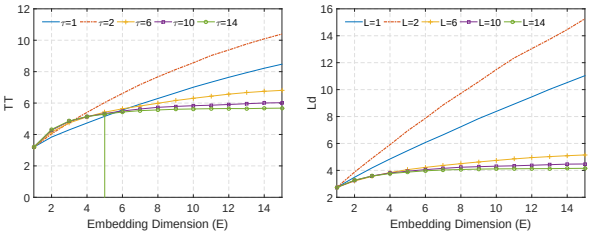

(d) TT (e) L_d

	L	**E**
MI/FNN	14	3
L=1/FNN	1	9
RQA/TT	14	5

Figure 2.15. PSR analysis of a non-linear correlated signal. The table presents the embedding parameters obtained with each method.

A similar and expected trend has been observed. The MI analysis finds the first null value for L to be 14. Its corresponding embedding dimension is 3. For L equal to 1, E is 9. The TT measure finds convergence values from L equal to 14, and the corresponding embedding dimension is 5 (Fig. 2.15).

In summary, the pair of embedding parameters given by the combination of the MI and the FNN algorithms approximately coincides with the RQA analysis for random signals. The slight differences are due to RQA measures' analysing the whole of the time series, whereas the FNN just takes into account the closest neighbours. The RQA analysis is a more conservative criterion in that sense.

2.5 Conclusions

The phase space reconstruction problem was assessed through traditional techniques. The different techniques to find the optimal time lag and embedding dimension were investigated. An alternative joint search for both optimal parameters, based on the RQA, has been developed. From the standpoint of phase space reconstruction, RQA measures exhibited a significantly better ability to adapt to the different natures of signals than traditional techniques. For instance, in those signals involving strong periodicities, an exhaustive search is needed since both embedding parameters have to be found together. In the case of discrete deterministic maps, the time lag must be fixed to 1, although the mutual information yielded a higher value. Finally, it has been shown that RQA measures are suitable for identifying the optimal embedding dimensions, and thus are a feasible alternative to the traditional techniques for any kind of signals.
Table 2.3 summarizes the analysed set of signals as well as the traditional and the proposed criterion applied to estimate the phase space reconstruction embedding parameters. In the following, the corresponding parameters are applied to each situation.

The analysis done in this chapter has shown one of the main motivations of the study of the modality of the signal: the need to identify the nature of the signals to improve its modelling and/or its analysis.

Table 2.3. Summary of the PSR criterion as a function of the nature of the signal and the applied technique.

NATURE OF THE SIGNAL		**TRATIONAL TECHNIQUES**	**RQA MEASURE**
Continuous Functions	Non-Periodic	L_{MI} FNN	Maximum TT
	Periodic	$L_{T/4}$ FNN	
Discrete Functions	Maps	$L = 1$ FNN	
	Stochastic Processes	L_{MI} FNN	Convergence TT

3 Determinism

Determinism 3

3.1 Introduction

Physical phenomena are naturally characterized by specific measures which progress in time. This evolution is quantified for the observer in recorded time series. Hereby, those recordings carry information along with disturbances described by stochastic, deterministic, chaotic processes, etc. [48]. There are several examples of acquired data which apparently may seem random but, in reality, an added stochastic process hides an underlying deterministic behaviour which may predict the forecast for the following day. Examples of that situation might be the aforementioned Henon map (Eq. 2.18) when adding a low amplitude stochastic process. At a glance, it might seem random, however, its phase space reconstruction reveals its underlying deterministic state space. Another example corresponds to the record of the air-conditioning in a warm summer. Its normal distribution corresponds to an apparently white noise, however, its state space shows the hidden periodic vibration of the corresponding machine engine.

Our work continues with this line of thought and proposes a new approach that attempts to extract information about the nature of the signal, thereby

characterizing the degree of determinism on ultrasonic signals. When scattering materials are subject to ultrasonic non-destructive testing (NDT), the deterministic ultrasonic pulse undergoes some variations that are related to the internal grain microstructure of the specimen. Each grain behaves like a scattering center, producing an echo that when superimposed on other echoes coming from other grains can even hide the echoes produced by a possible defect. Similar situations are found in other related fields such as ultrasound B-mode scans (where the grain noise is called speckle) and in radar with clutter [49].

In the literature, a wide range of solutions has been proposed to enhance the detection of small cracks or defects and to reduce (or even eliminate) the effect discussed in each of the above situations. Some of these solutions are signal averaging, auto- and cross-correlation, matched filtering, frequency spectrum analysis [50], spectral correlation [51], and wavelet transformations [52]. The aforementioned analyses discard the information encoded in the grain noise; however, this information can be used to recognize potential differences among materials, tissues, or surfaces. This approach has been employed to characterize materials by extracting temporal signal statistics [49], the resonance frequency [53], and even the penetration depth [54]. In this chapter, we propose a novel and completely different approach to the problem of scattering material characterization: measuring the degree of determinism of the time series. Measuring predictability can provide information of the signal strength of the deterministic component of the time series in relation to the whole time series acquired.

The remainder of this chapter is organised as follows. Section 3.2 describes and mathematically formulates three algorithms that are typically employed in chaos theory when studying determinism. Furthermore, Section 3.2.4 proposes an alternative index based on higher order statistics which avoids some of the drawbacks when measuring predictability. All these algorithms are tested in Section 3.3 with a theoretical ultrasound model. In Section 3.4, we focus on a real ultrasonic application where different kinds of scattering materials are classified by measuring their degree of predictability. A further step is done in Section 3.5 where a new approach of the Recurrence Plots based on angular distance is studied for cement pastes characterization. Finally, the conclusions are summarized in Section 3.6.

3.2 Algorithms

Having access to the input and the output of a system, the level of determinism of a system might be quantified as the difference between the predicted output computed from the input, however, in a blind approach the study of a deterministic signal relies on the phase space reconstruction. A time series $x[n]$ is said to be deterministic if its reconstructed phase space is smooth and can be modelled as a continuous function. In the bibliography can be found different algorithms which have tried to measure the continuity of the phase space, Kaplan-Glass method (Section 3.2.1), or its smoothness, Jeong et al. method (Section 3.2.2).

3.2.1 Modified Kaplan-Glass Method

Wayland et al. [55] developed a method that detects determinism by testing the continuity in the reconstructed phase space. This algorithm finds the nearest neighbours and computes the average distance between consecutive points.
Let $\vec{X}[n_0]$ be a fixed phase space vector that is computed as in Equation 2.3 (Section 2.2), and let $\vec{X}[n_1], \vec{X}[n_2], \ldots, \vec{X}[n_K]$ be its K nearest neighbours. If the time series under study is deterministic, the displacement vector defined as

$$\vec{V}[n_k] = \vec{X}[n_k + 1] - \vec{X}[n_k] \tag{3.1}$$

for each one of the K neighbours and its consecutive vectors is expected to be almost the same.

To quantify this similarity, we compute the average of the translation vectors $\vec{V}[n_k]$

$$\left\langle \vec{V} \right\rangle = \frac{1}{K+1} \sum_{k=0}^{K} \vec{V}[n_k] \tag{3.2}$$

The translation error that is used as the predictability index is computed as shown in Equation (3.3)

$$DMKG_{n_0} = \frac{1}{K+1} \sum_{k=0}^{K} \frac{\left\| \vec{V}[n_k] - \left\langle \vec{V} \right\rangle \right\|^2}{\left\| \left\langle \vec{V} \right\rangle \right\|^2} \tag{3.3}$$

This calculation is extended to a subset $\vec{X}[p] \subset \vec{X}[n]$ of N_{res} random centres (defined by $\vec{X}[n_0]$) of the phase space (a quarter of the total number of points is an accurate solution). The median of these values will be called $DMKG$ and it provides a robust measure of the continuity of the "phase space".

$$DMKG = \underset{\vec{X}[n_0] \in \vec{X}[p]}{\text{Median}} \left[DMKG[n_0] \right] \tag{3.4}$$

With this algorithm, we are able to quantify the spread of the phase space based on the vector translations. If the time series is predictable, $\vec{V}[n_k]$ will be nearly equal and the continuity index using the Modified Kaplan-Glass Method ($DMKG$) will be very small. Otherwise, $\vec{V}[n_k]$ will be different and the resulting continuity index will be larger.

3.2.2 The Method of Jeong et al.

Jeong et al. [56] also computed the phase space, proposing a new predictability measure that is based on the angles between consecutive vectors, eliminating the need to search for neighbouring points.

Let

$$\vec{V}[n] = \vec{X}[n+1] - \vec{X}[n] \tag{3.5}$$

be the tangent between consecutive vectors in the phase space; the angles are computed as

$$\cos(\theta_n) = \frac{\vec{V}[n+1] \cdot \vec{V}[n]}{\left\| \vec{V}[n+1] \right\| \left\| \vec{V}[n] \right\|} \tag{3.6}$$

where $\vec{V}[n+1] \cdot \vec{V}[n]$ denotes the scalar product of vectors $\vec{V}[n+1]$ and $\vec{V}[n]$. The predictability index is obtained by averaging the computed angles in the whole phase space:

$$DJM = \frac{1}{S}\sum_{n=1}^{S}\cos(\theta_n) \tag{3.7}$$

where $S = (N - (E-1)\cdot L) - 2$, and N is the total number of samples.

If the time series is deterministic, the trajectory in the state space is smooth and most of the cosine values are close to 1 (or larger than 0.7). Otherwise, if the time series is stochastic, cosine values are near 0 (or smaller than 0.3). The intermediate case (0.3-0.7) is known to sometimes arise from time series having different degrees of predictability.

3.2.3 Recurrence Plots

In Section 3.2.3, the Recurrence Plots were introduced, which allow visualizing the recurrence of states $\vec{X}[n]$ in a phase space. This tool may also be used to study the degree of determinism since a diagonal line in the RP appears when a segment of the trajectory runs parallel to another segment. The length of this diagonal line is determined by the duration that the two trajectory segments have a similar evolution. As a result, the presence of diagonal lines that run parallel to the mean diagonal (line of identity) indicates that the evolution of states is similar at different times and that the process could be deterministic. The percentage of recurrence points that form diagonal lines can be used to measure predictability. This percentage can be computed as follows:

$$DRP = \frac{\sum_{j=j_{min}}^{N_s} j\cdot P(j)}{\sum_{n_1,n_2=1}^{N_s} RP[n_1,n_2]} \tag{3.8}$$

where N_s is the number of possible states, $P(j)$ is the number of diagonal lines of length j and j_{min} is the minimum number of points to be considered as a diagonal line (in this work, $j_{min} = 2$ is used).

3.2.4 Determinism based on higher order statistics

Ultrasonic scattered signals are not simply deterministic or stochastic, but rather a combination of both [57]. Predictability can be viewed as the signal strength of the deterministic component of the time series with respect to the whole time series. A feasible alternative for characterizing

the predictability of the signal is to use the correlation between points. Second-order correlation (autocorrelation) cannot give enough information about higher order interactions among parameters that govern the model which leads to the time series. Due to the complex physical interactions taking place in the ultrasonic inspection of a highly scattering material, we propose using higher order statistics to measure the predictability of the time series.

Let us model the ultrasonic register as a discrete stationary stochastic process $\{\tilde{x}[n]\}$. We can define what will be called a displacement sequence,

$$\{\tilde{S}_m[n]\} = \{\tilde{x}[n]\} - \{\tilde{x}[n+m]\} = \{\tilde{x}[n]\} * h[n] \tag{3.9}$$

where m is the time delay, $*$ denotes the discrete convolution of the stochastic process $\{\tilde{x}[n]\}$ with the linear time-invariant system $h[n] = \delta[n] - \delta[n+m]$, and $\delta[n]$ is the discrete Dirac delta function.

The statistical properties of $\{\tilde{S}_m[n]\}$ can be analysed as a function of the statistics of the input process $\{\tilde{x}[n]\}$ and the impulse response of the filter $h[n]$, previously defined. We can obtain the 4^{th} order cumulant of $\{\tilde{S}_m[n]\}$ ($c_4^{S_m}(k_1,k_2,k_3) = E[S_m[n]S_m[n+k_1]S_m[n+k_2]S_m[n+k_3]]$) using filter relationships of a colored process [58]:

$$c_4^{S_m}(k_1,k_2,k_3) = \sum_{m_1}\sum_{m_2}\sum_{m_3} c_4^x(k_1-m_1,k_2-m_2,k_3-m_3)\cdot c_4^h(m_1,m_2,m_3) \tag{3.10}$$

where

$$c_4^h(m_1,m_2,m_3) = \sum_l h(l)h(l+m_1)h(l+m_2)h(l+m_3) \tag{3.11}$$

In Equation 3.10, k_1, k_2 and k_3 are the time lags where the 4^{th} order cumulant of the process $\{\tilde{S}_m(n)\}$ is evaluated and m_1, m_2, m_3 are also time lags varying in the region of support of the 4^{th} order cumulant. If Equation 3.10 is particularized for $k_1 = k_2 = k_3 = 0$, the kurtosis ($\gamma_4^{S_m}$) of the displacement sequence is obtained (see Equation 3.12).

$$c_4^{S_m}(0,0,0) = \gamma_4^{S_m} = \sum_{m_1}\sum_{m_2}\sum_{m_3} c_4^x(-m_1,-m_2,-m_3)\cdot c_4^h(m_1,m_2,m_3) \tag{3.12}$$

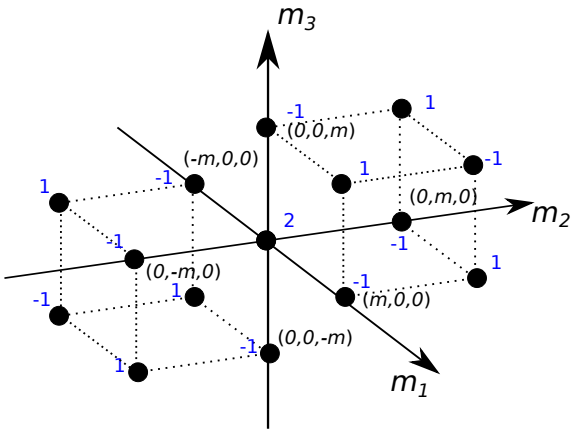

Figure 3.1. Graphical representation of the 4^{th} order cumulants of $h[n]$. The black dots indicate unique values where $c_4^h[m_1, m_2, m_3]$ is non zero (the blue numbers next to the dots indicate the amplitude of the cumulants at these lags).

The deterministic 4^{th} order cumulants $c_4^h(m_1, m_2, m_3)$ are only non zero for some specific lags as illustrated in Fig. 3.1. Using this property and also taking into account the symmetry properties of the 4^{th} order cumulants, Equation (3.12) can be simplified into Equation (3.13).

$$\begin{aligned}\gamma_4^{S_m} &= 2 \cdot \Big(c_4^x(0,0,0) - c_4^x(m,0,0) - c_4^x(0,0,m) - c_4^x(0,m,0) + \\ &\quad c_4^x(m,m,0) + c_4^x(m,0,m) + c_4^x(0,m,m) - c_4^x(m,m,m) \Big) \\ &= 2 \cdot \Big(c_4^x(0,0,0) - c_4^x(m,m,m) + 3 \cdot c_4^x(m,m,0) - 3 \cdot c_4^x(m,0,0) \Big)\end{aligned} \tag{3.13}$$

Thus, evaluating the 4^{th} order central moment (kurtosis) of the displacement sequence $\{\tilde{S}_m[n]\}$ provides a simple way of measuring how the 4^{th} order cumluants of $\{\tilde{x}[n]\}$ change with the time lag m. This time lag defines the side of the cube whose vertexes are the points where $c_4^x(k_1, k_2, k_3)$ is evaluated. In order to obtain a clear indication of how the higher order correlations evolve as the time lag increases, the vertex of this cube must increase. In this work, we propose using an averaged kurtosis of the dis-

placement sequence obtained for different time lags m as an estimator of the predictability:

$$DAKDS = \frac{1}{M} \sum_{m=1}^{M} \gamma_4^{S_m} \tag{3.14}$$

where M is the maximum lag introduced whose choice depends on the sample frequency and the size of the observation window; however, this choice is not critical. DAKDS are the acronyms of Determinism based on the Average Kurtosis of the Displacement Sequence. It is worth noting that the 3^{rd} order statistic moment (skewness) has not been applied since its equivalent expression to Equation 3.13 would be null for all kind of signals, whether they are deterministic or stochastic. The 4^{th} order cumulant is the lowest statistic which allows predictability to be measured taking into account higher order interactions.

The conventional way of measuring the kurtosis consists of assuming ergodicity and computing the time averages of $\frac{E[(S_m[n]-\mu)^4]}{\sigma^4} - 3$, where μ is its mean and σ is its standard deviation of $\{\tilde{S}_m[n]\}$. Kurtosis can be interpreted as a measure of the dispersion of a distribution around the values $\mu \pm \sigma$, which can be large when the probability mass is concentrated either near the mean or in the tails of the distributions. To solve this, a robust alternative to estimate the kurtosis was proposed in [59] and will be used here:

$$\gamma_4^{S_m} = RK(S_m(n)) = \frac{(E_7 - E_5) + E_3 - E_1}{E_6 - E_2} - 1.23 \tag{3.15}$$

where E_j is the j^{th} octile of the distribution of a realization $\{\tilde{S}_m(n)\}$. The estimator RK is consistent and unbiased. A detailed analysis of this estimator for different types of distributions is done in [60]. Additionally, RK it is not even influenced by the presence of outliers since it is based on octiles, which converge to the true values reasonably quickly.

3.3 Determinism on Ultrasonic Signals

In order to apply signal modality algorithms to ultrasonic signals, a brief review of the typical noise sources that appear in ultrasonic inspection must be made. The vast majority of noise sources can be approximated by random processes (thermal noise, quantification, etc.), but some of the sources have a distinctly deterministic pattern (vibrations, grain noise, or speckle). Figure 4.1 illustrates how coherent and incoherent noises are combined as a function of the inner material structure in a typical ultrasonic inspection of scattering materials. Measuring the predictability of the resulting signals can give information about this blend and, thus, about the material characteristics.

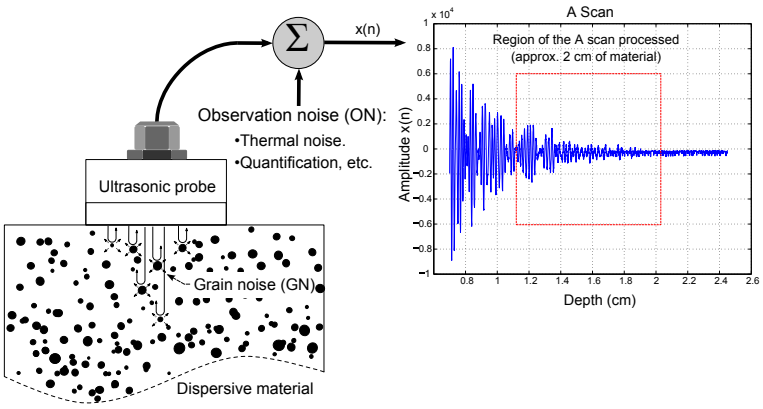

Figure 3.2. Pulse-echo model of an ultrasonic inspection of scattering materials and an example of the resulting signals.

Firstly, we analyse the results achieved by applying the four methods described above on simulated ultrasound signals. The simulated signals were obtained using the model presented in [49] and reproduced in Equation 3.16. This equation simulates a backscattered ultrasonic signal at time t for a given transducer position $\mathbf{z}$.

$$x(t,\mathbf{z}) = \sum_{i=1}^{N_e(\mathbf{z})} A_i(\mathbf{z}) \cdot p(t-\tau_i(\mathbf{z})) \cdot cos(w_0(t-\tau_i(\mathbf{z}))) + \{\tilde{n}(t)\} \qquad (3.16)$$

where

$$p(t-\tau_i(\mathbf{z})) = p_0(t-\tau_i(\mathbf{z}))\cdot e^{-\alpha\cdot(t-\tau_i(\mathbf{z}))} \tag{3.17}$$

Equation 3.16 computes the backscattered signal (A-scan) as the sum of all contributions from the $N_e(\mathbf{z})$ scatters characterized by their reflectivity $A_i(\mathbf{z})$ placed randomly ($\tau_i(\mathbf{z})$) inside the sample, with $p_0(t)$ being the pulse envelope at the origin, and w_0 being the carrier frequency. Note that, due to attenuation $\alpha(dB/cm)$, the amplitude of $p(t-\tau_i(\mathbf{z}))$ will decrease exponentially as the ultrasonic pulse propagates deeply into the material (Eq. 3.17). The stochastic process $\{\tilde{n}(t)\}$ models the Observation Noise (ON), and it is incorporated to model the instrumentation noise or other effects that are not related to material properties (Fig. 3.2). Thus, the resulting simulated signals are the sum of a material dependent Grain Noise (GN) plus a random ON. Due to the different grain echoes and the attenuation with depth, the registered A-scans show characteristic waveforms whose amplitude decays until GN collapses below the ON level. As a result, the signals have a decreasing GOR (Grain-to-Observation-Noise-Ratio), which is characteristic of the sample being tested. When two specimens with different amounts of grain are compared, the nature of the reflected signal will be different. In the case of fewer grain echoes, the reflections or echoes will be similar to the incident signal. However, in the presence of more scatters, the energy will be dispersed and there will be a large number of contributions which will give rise to different levels of predictability. In order to prevent predictability measures being from the result of attenuation and signal amplitude changes, the signal resulting from the model have been normalized in amplitude without varying the rest of the properties.

The four methods described in Section 3.2 have been evaluated using the the ultrasonic backscattered signal of Equation 3.16. The parameters employed in the simulation were: $w_0 = 2\cdot\pi\cdot 10\ MHz$, attenuation 10 dB/cm, percentage of scatterers 40%, and K-Type amplitude distributed reflections with shape parameter 0.5. The estimated indexes were computed for 50 Monte Carlo realizations for each attenuation level. The data length is 1500 points. We present Figure 3.3 to analyse the behaviour of the predictability indexes against different attenuation values. Figure 3.3(a) shows that $DMKG$ (Eq. 3.4) and DJM (Eq. 3.7) do not allow the level of signal attenuation to be identified from predictability since the curves reach constant values above a certain level of attenuation (1 dB/cm and 4.5 dB/cm, respectively). When attenuation increases, the maximum GOR

decreases; therefore, both methods fail to provide a characteristic measure that allows predictability identification for high noise levels. However, Figure 3.3(b) shows the resulting curves for DRP (Eq. 3.8) and $DAKDS$ (Eq. 3.14) that allow us to determine the value of the characteristic attenuation based on the predictability measured. Both curves show that despite high attenuation levels, both methods are able to distinguish signals even if they are random. This results are justified because of the binarization process that the RP plots undergo through the Heaviside function (DRP parameter) and because of the insensitivity of the higher order statistics to Gaussian noise (DAKDS parameter).

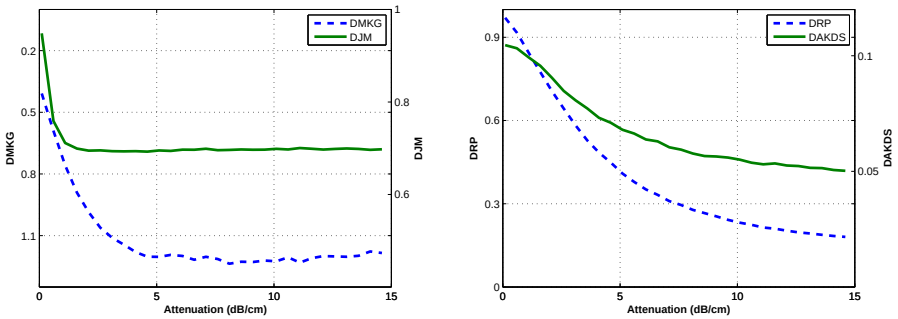

(a) (b)

Figure 3.3. Degree of predictability as a function of the attenuation values (dB/cm) for the ultrasonic model. The data length is 1500 points, and 50 Monte Carlo realizations are used for each attenuation level and each model. The ultrasonic model parameters are: carrier frequency f_0 equals 10 MHz, reflectivity 40% and the statistic of the reflectivity is K-Type. a) DMKG (left) and RJM (right), b) DRP (left) and DAKDS (right).

3.4 Cement Pastes Characterization I

We applied the proposed parameters in a real application to measure the degree of porosity of different cement paste probes. This is an important problem because cement paste is the main component of mortar and

concrete [61]. The vulnerability (and, thus, the durability) of these construction materials to external agents is very dependent on the porosity of the cement [62].

3.4.1 Experimental

We consider cement paste to be composed of a hydrated gel matrix with pore cavities that are incrusted within and not occupied by gel. Porosity is dependent upon the water/cement ratio (w/c) and cement composition. In this study, we chose two types of cement with the same mineral composition and identical percentage of added limestone (about 17% of substitution), but with a different specific surface of grain. Therefore, we had two different mechanical strength categories, namely 32.5 and 42.5 MPa. We used the notation CEM 32.5 and CEM 42.5 and considered two different w/c ratios (0.4 and 0.5), so that there were four cement paste types.

We built 32 test samples (8 for each type of cement paste), which were prisms of a size $4 \times 4 \times 16$ (cm^3) (Fig. 3.4). Four of them were used for measuring (in a destructive manner) the porosity of each type of cement paste following the method described in [63]. Table 3.1 shows the porosity mean value obtained (the average of the four test samples) for each type of cement paste. The other four test samples were used to perform ultrasonic non-destructive testing.

Table 3.1. Porosity mean values corresponding to the four types of test samples.

	Water/Cement ratio	
Type of cement (MPa)	0.4	0.5
32.5	30.73 %	37.63 %
42.5	27.36 %	33.65 %

Ultrasonic testing in pulse-echo mode involves one transducer (also called probe) sending an ultrasonic pulse wave into the part under inspection and receiving the reflected echoes (Fig. 3.5). The transducer is directly coupled to the specimen's surface with gel as coupling medium. At boundaries between materials that differ on density and ultrasonic velocity, the acoustic impedance, part of the wave is transmitted and part of the wave is

reflected. The received echoes are converted to voltage in the transducer due to the direct piezoelectric effect. These can be shown against time as a so-called amplitude scan or A-scan on a screen, similar to an oscilloscope. In each sample, we collected 20 A-scans of backscattering noise along the two sides of the prism that were uniformly spaced. One of this A-Scan is shown in Figure 3.2. The ultrasonic equipment and the most significant acquisition settings were: ultrasound pulser-receiver card (IPR-100, Physical Acoustics, Princeton, USA); transducer (Krautkramer KBA-10 MHz, Huerth, Germany); digitalisation (Osciloscope Tektronix TDS-3012, Wilsonville, USA); and sampling frequency (250 MHz).

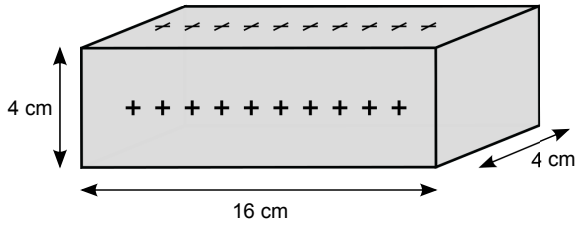

Figure 3.4. Example of cement paste specimen and the places where the 20 A-scan were measured.

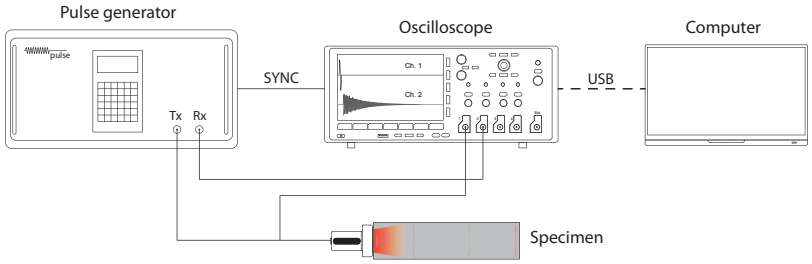

Figure 3.5. Pulse-echo model of an ultrasonic inspection of scattering materials

The selection of the 10 MHz transducer was justified by the need to obtain enough grain noise in the collected records. Using the mercury intrusion method, we verified that, at 10 MHz, $E[D]/\lambda$ varied between 0.026 and 0.071 for the different types of cement paste considered, where λ is the wavelength, D is the grain size and $E[\cdot]$ is the expected value operator. Therefore, we are working in the Rayleigh region [64], and we have a moderate, but sufficient, amount of grain noise (Fig. 3.6). When the frequency increases, it produces an attenuation that is too large; when the

frequency decreases, it reduces the level of GN (the ultrasound pulse propagated better, but there were no echoes from the inner microstructure). Having enough information about the inner composition of the probes is paramount in classifying the probes as a function of the predictability measured on the echo pulses.

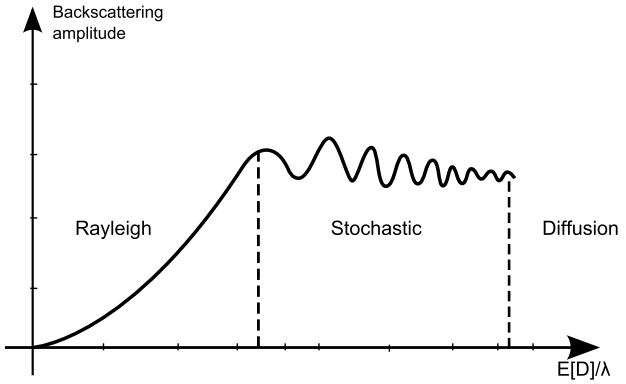

Figure 3.6. Behavior of the dispersion coefficient in ultrasound as a function of the normalized grain diameter ($E[D]/\lambda$).

3.4.2 Results

As mentioned in Section 3.3, the degree of predictability must be proportional to the number of pores in the material. Figure 3.7 compares the phase space of ultrasound signals measured in two different specimens. It must be highlighted that the trajectories followed similar paths, but the plot on the left is smoother than one on the right. If there is a higher number of pores, the signal is more irregular, which is a clear sign of randomness.

Accordingly, we must be able to estimate the percentage of pores in each of the resulting samples of different materials or different manufacturing processes by applying the reviewed methods. For this purpose, the four algorithms were applied on the 20 signals measured in each specimen. For each record, we considered an interval of 1300 points, removing the initial transient and long end tails, which had been subjected to a process of normalization in amplitude. Those points covered a depth distance of 2 cm (an average propagation velocity of 3500 m/s was used to convert time scale into depth scale).

For each method, the parameters introduced in the mathematical formu-

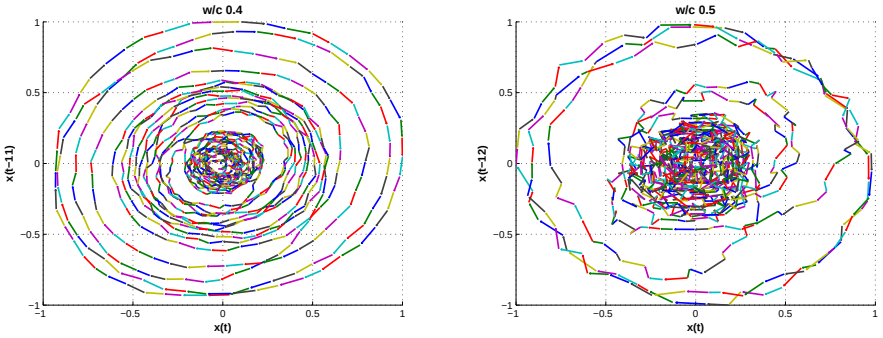

(a) (b)

Figure 3.7. a) Phase space of an ultrasound signal measured in a w/c 0.4 sample. b) Phase space of an ultrasound signal measured in a w/c 0.5 sample. E=2 and L=11.

lation were configured as follows. For the reviewed methods ($DMKG$, DRP, and DJM), the embedding parameters were chosen according to the analysis done in Chapter 2. Being strong periodic signals, the embedding dimension E was equal to 2 and the time lag L corresponds to the forth of the period T expressed in number of samples, $T/4$. It might be computed as the first null of the non-bias autocorrelation function of the signal. Moreover, in $DMKG$, $K = 5$ neighbors and $N_{res} = 100$. In DRP, ε was equal to 60% of the mean Euclidean distance of the phase space vectors [65]. From the above, it can be deduced that the reviewed methods require a greater number of input parameters than the proposed method which eliminates having to calculate the autocorrelation, and the result was weighted to a maximum lag M equal to 400 points.

Figure 3.8 shows the boxplots obtained for each test sample and each method. Note that we tested 4 specimens of each class indicated on the x-axis. The red marks represent the median value of the 20 measures, and the blue box boundaries are the 25^{th} and 75^{th} percentiles. At a glance, it can be observed that the four methods group each specimen sample so that a cluster can be identified for each type of material. If we compare the predictability values obtained and the results using the theoretical simulation (Fig. 3.3), it can be concluded that all recorded signals had low attenuation levels (below 5 dB/cm), and, therefore, excellent GOR rela-

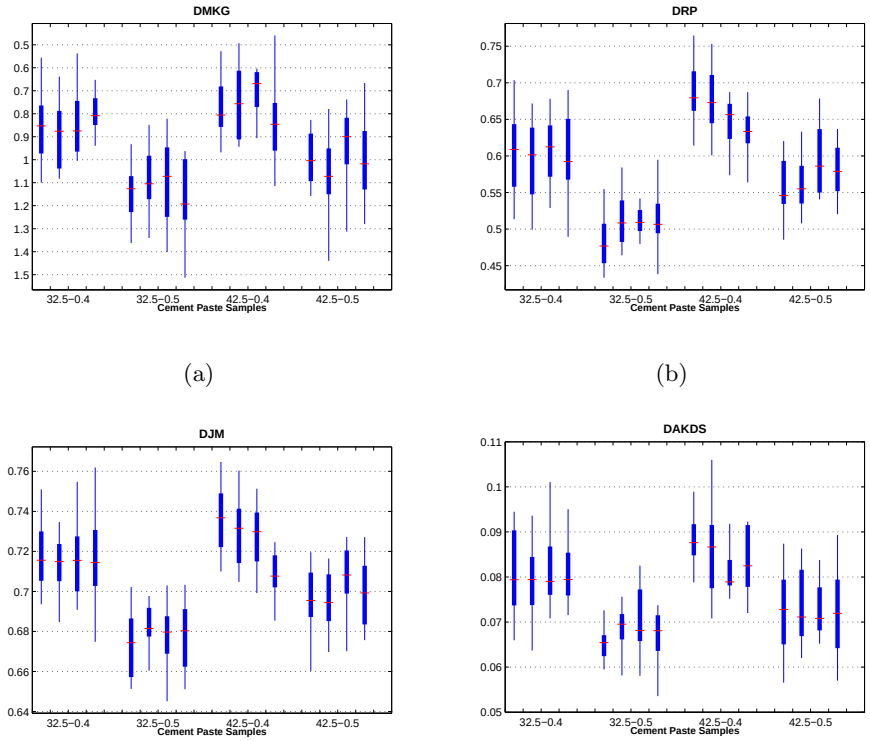

Figure 3.8. Plot of the predictability measures versus the different cement paste samples. The red marks represent the median value and the blue box boundaries are the 25^{th} and the 75^{th} percentiles. a) DMKG, b) DRP, c) DJM, d) DAKDS.

tions. Then, all four methods were able to identify the different materials in this interval. Moreover, the trend coincided in all of the methods and indicated that the specimens with w/c ratio 0.4 were classified with greater predictability values; however, the specimens of w/c ratio equal to 0.5 were more random, which is correlated with the higher percentage of porosity presented in Table 3.1.

In order to further analyse the relation between predictability and the percentage of pores, the results were adjusted to a linear equation whose representation is plotted in Figure 3.9. The plot illustrates the linear approx-

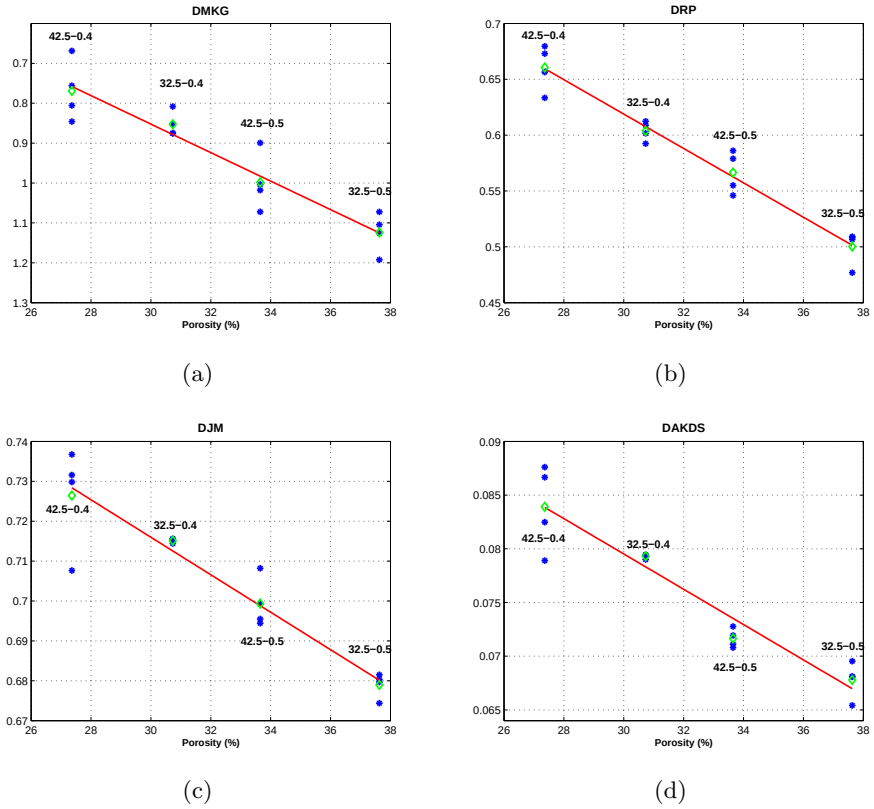

Figure 3.9. Plot of the predictability measures versus the porosity for each type of cement paste. The blue marks represent the median value for each sample, the green marks represent the median value for each class, and the red lines represent the linear approximation computed for each method. a)DMKG, b) DRP, c) DJM, d) DAKDS.

imation estimated for each method as well as the median predictability index obtained for each specimen of each class (blue marks). Furthermore, the median value for each class (green diamonds) is also shown. Table 3.2 highlights the excellent linear fitting obtained in all cases regarding the regression error. To compute this quality measure, the resulting linear approximations and the measures were normalized to the interval between 0 and 1. The proposed robust DAKDS algorithm obtained results that are comparable to other published methods.

Table 3.2. Linear regression error corresponding to the four algorithms.

	DMKG	**DRP**	**DJM**	**DAKDS**
Error	0.3559	0.1378	0.2978	0.2875

3.5 Cement Pastes Characterization II

Standard methods for detecting porosity with NDT using ultrasonic pulse-echo inspection include the evaluation of the back-wall echo (BWE) from the side opposite to the ultrasonic probe, or the grain noise signals mentioned in Section 3.1. Both approaches are based on the analysis of the received echoes against time, the so-called amplitude scans or A-scans. These standard techniques fail in special situations: complex geometries like wedge or curved parts, sandwich structures with multiple echoes, etc. Therefore, new robust techniques not depending on the signal amplitude or attenuation need to be studied.

In Section 3.4.2, it has been highlighted that in order to avoid depending on the received amplitude and intrinsic material attenuation, the signals had been normalized in amplitude. In the current section, the amplitude dependence of the RP is analysed in detail and the use of an alternative RP approach based on the angular distances is developed.

3.5.1 RP based on Angular Distance

In order to illustrate the sensitivity of the RP to the amplitude, Eqs 2.10 and 2.11 must be recalled (Section 2.3). Figure 3.10 graphically explains the concept of applying the Euclidean distance in the expression of the Recurrence Plots. The diagonal lines in the DP (and the RP after threshold) computed by Euclidean distance represent states where a section of the trajectory of the dynamical system runs nearly parallel to another section of the trajectory, or more exactly, in a region with the shape of a tube (of radius ε) around the other section. The Euclidean distance causes only the closest points in the phase space to be taken into account as recurrence points, and not those that also follow similar paths but with different values of the amplitude.

Figure 3.10(b) plots an example DP computed by the Euclidean distance for a representative ultrasonic A-scan. It must be noted that the diagonal lines are not equally distributed over the whole time signal, but are focussed on a temporal interval that correspond to the higher amplitudes of the signal. Furthermore, this characteristic distribution makes it difficult to choose the Euclidean distance threshold, ε. Figure 3.11 compares the choice of two different thresholds and the resulting RPs: a large one and a small one. The decaying amplitude of the original time series apparently leads to a trajectory which falls for later instants of time completely into the ball with radius ε in state space (almost black regions on the upper right corner). Therefore, the Euclidean distance cannot reveal recurrences in the case of signals having similar time-shifted components but with different amplitudes. Using a non-Euclidean distance may help to alleviate the 'banding effect' due to the non-stationarity of the ultrasonic signal.

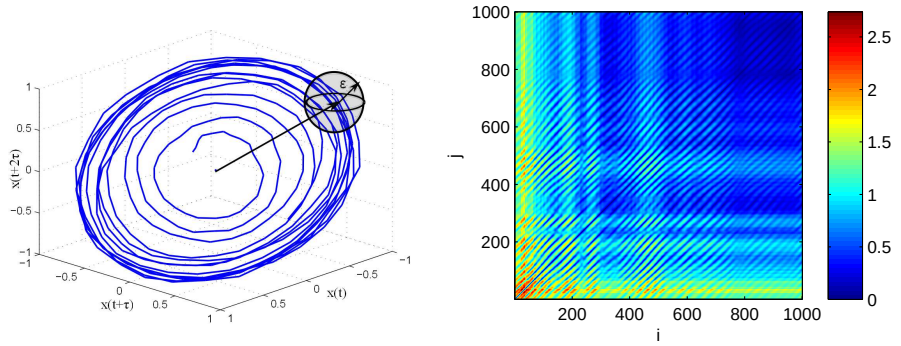

(a) (b)

Figure 3.10. RP based on the Euclidean distance. a) Graphical representation of the Euclidean distance projected over a representative phase space. b) Distance Plot based on the Euclidean distance.

Ioana et al. [48] propose a new approach for computing the *RP* based on the angular distance, which stands out for its independence from scaling effects. The proximity between points in the phase space stops being proportional to the Euclidean distance and is measured by the solid angle which they form with the origin. Its mathematical expression is given by Equation 3.18.

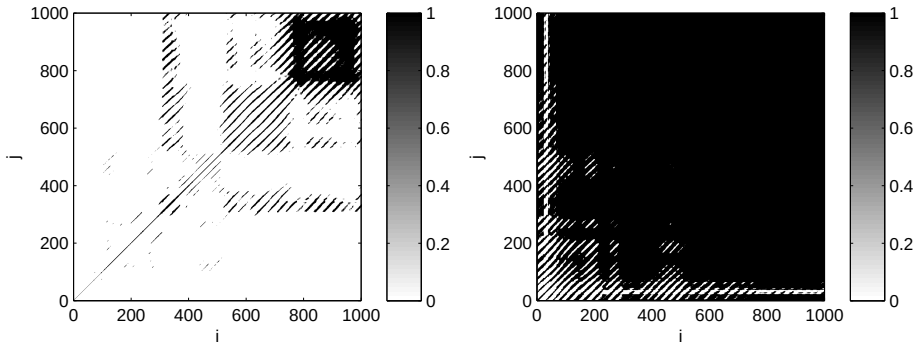

(a) (b)

Figure 3.11. RP comparison based on the threshold ε choice. a)RP applying ε equals 0.5. b) a)RP applying ε equals 1.3.

$$DP(n_1, n_2) = arccos\left(\frac{\vec{X}[n_1] \cdot \vec{X}[n_2]}{\left\|\vec{X}[n_1]\right\| - \left\|\vec{X}[n_2]\right\|}\right) \tag{3.18}$$

where $\vec{X}[n_1] \cdot \vec{X}[n_2]$ is the scalar product of two vector samples. Using this distance, it is possible to identify the points of the trajectory placed in a solid angle and that correspond to the components with different amplitudes. Unlike the Euclidean distance, the angular distance quantifies the aperture delimited by the position vectors $\vec{X}[n_1]$ and $\vec{X}[n_2]$ (Figure 3.12(a)).

Figure 3.12(b) shows the DP based on the angular distance from the same ultrasound signal whose DP was shown in Figure 3.10. At a glance, it can be noticed that the diagonal lines are now almost uniformly distributed along the time domain. This illustrates how the points corresponding to similar trajectories of the ultrasonic backscattered signal with different amplitudes are found using the angular distance, whereas in the case of the Euclidean distance, they were separated depending on the radius of the sphere. Furthermore, the angular distance not only highlights signals having similar trajectory features regardless of their amplitude, but also eases the choice of the optimal value of ε. The phase results on a uniform distribution in $[0, \pi]$ so the value of ε may be fixed to be $\pi/2$.

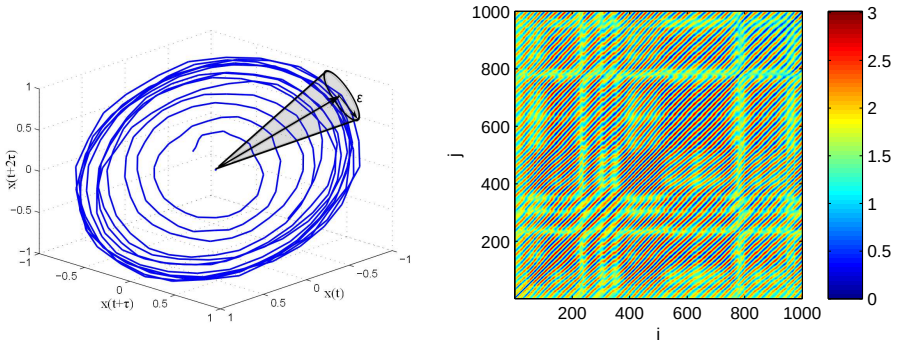

(a) (b)

Figure 3.12. RP based on the angular distance. a) Graphical representation of the angular distance projected over a representative phase space. b) Distance Plot based on the angular distance.

Figures 3.13(a) and 3.13(b) compare the resulting RP for two ultrasonic signals measured in two different specimens. The left graph corresponds to a specimen built with a w/c ratio equal to 0.4 (porosity equal to 30.73%) and the right graph corresponds to a specimen built with a w/c ratio of 0.5 (porosity equal to 37.63%). The presence of a larger number of pores results in a clear sign of randomness, seen as a deviation from the diagonal lines in the angular distance RP domain. The whole set of measurements is analysed in the following Section 3.5.2.

The use of this metric for Recurrence Plots is considered as a great asset for NDT to be less dependent on the adjustment of the gain in the course of calibration. Because this often involves a human factor, it is advisable to achieve an independence or reduced dependence on the calibration.

3.5.2 Results

In order to show the potential of the technique, this new signal processing approach is applied on the same experimental real data described in Section 3.4.1. There is a single input parameter: the aforementioned ε threshold, which is set to $\pi/2$. Figure 3.14(a) shows the resulting boxplot obtained for each specimen. Recall that the legend is the same as in Figure 3.8. The manufacturing properties of each specimen are described on the x-

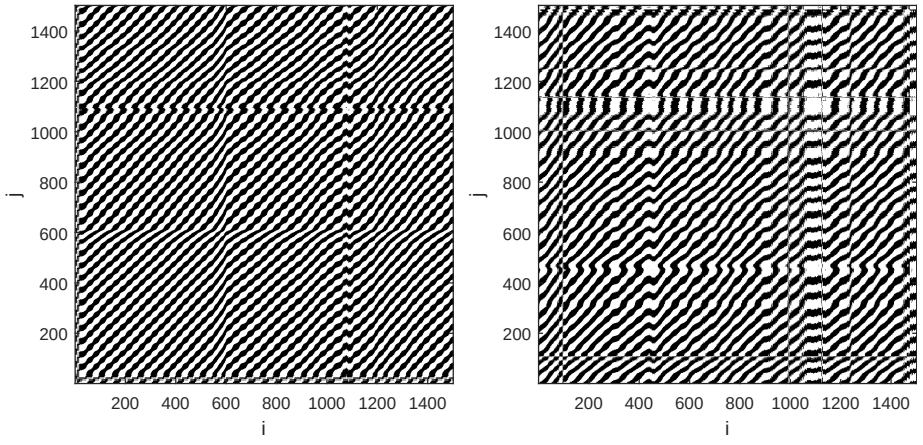

Figure 3.13. a) Recurrence Plot based on angular distances of an ultrasound signal measured in a sample with $w/c = 0.4$. a) Recurrence Plot based on angular distances of an ultrasound signal measured for a sample with $w/c = 0.5$. $E = 2$ and $L = 11$.

axis: the red line marks the mean values, and the blue box boundaries are the 25^{th} and 75^{th} percentiles. It can be observed that the specimens with same properties make up easily identifiable clusters, slightly up-biased in values of DET compared to the amplitude analysis shown in Figure 3.8(d). As expected, the determinism decreases as w/c increases, a trend which appears in both kinds of cement (for 32.5 MPa and 42.5 MPa).

Figure 3.14(b) plots a linear fitted model to the median value of the parameter DET of each category and its real porosity values. Once again, each cement makes up a clear cluster, and all together would allow computing a linear regression in order to compute the real value of the porosity as means of determinism. Furthermore, the error from the linear regression has turned out to be 0.1052, lower than any approach reviewed in Section 3.4.

In summary, for the angular distance, the RQA feature DET has been found to be appropriate porosity measurement equivalent. Amplitude effects are not taken into account with angular distance by definition, and the feature decreases with increasing porosity, showing a lower periodicity

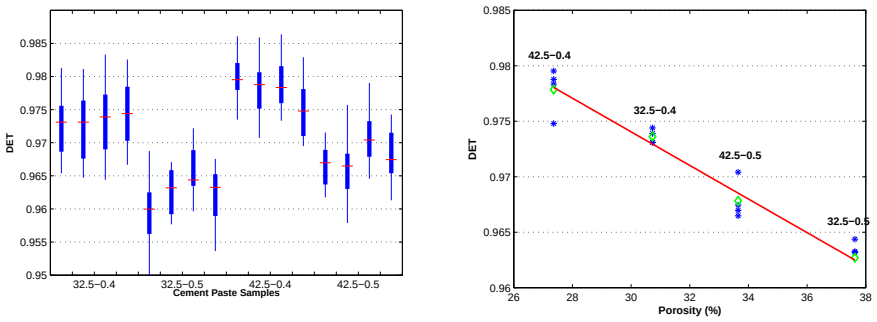

(a) (b)

Figure 3.14. a) Boxplot representation of the cement paste types and the values of determinism. b) Linear regression of the values of porosity and the values of determinism.

in the ultrasonic wave propagation caused by the pores.

3.6 Conclusions

In this chapter, we have considered the general problem of ultrasonic characterization of scattering materials from a viewpoint that is different from those seen to date. We propose the study of the nature of the signal through predictability and using this parameter as a source of information of the inner material structure.

We have reviewed some of the methods that are available in the literature to measure predictability, and we have also proposed an alternative algorithm based on higher order statistics that is easier to implement than traditional ones and that achieves equivalent results. The predictability index has been used to evaluate a theoretical ultrasound model as well as to estimate the porosity of real cement probes. The theoretical results have shown that the proposed algorithm is more robust against low SNR signals than the rest of the methods and is also less parameter-dependent. When measuring real signals, determinism is strongly related to the degree of ultrasonic scattering; in fact, it has been shown that a linear relation can be an excellent approximation for calculating the porosity of the cement paste

probes based on predictability. This new approach can complement or even be used as an alternative to other techniques when extracting information about the internal structure of scattering materials.

A recent RP approach for non-stationary signals has also been analysed in detail. Angular distance, by definition, is not affected by attenuation with depth; resulting an appropriate estimation for ultrasonic wave signals which attenuate as propagate. The results are equivalent to the previous algorithms leading to lower values of determinism with higher porosity content.

The proposed approach based on predictability could be used in other applications of characterization of scattering materials using ultrasound. In Chapter 4, we analyse its applicability on a NDT damage characterization application.

NDT Damage Characterization 4

4 NDT Damage Characterization

4.1 Introduction

In the present chapter, the signal modality concept is applied to analyse the interaction between the injected ultrasonic wave and the non-linear scatters placed at the concrete specimen under study. Figure 4.1 illustrates a typical ultrasonic inspection where the input signal has a predominant deterministic component (coherent component) and the output is the sum of many superimposed echoes scattered by the heterogeneous microstructure of the material (incoherent components). The resulting stochastic nature of the received signal comes not only from the randomly placed reflections, which cause significant changes in amplitude, but also from the echoes transmitted by non-linear coupling, which combine with different initial phases. Measuring the degree of predictability of the received signals can give information about how the coherent and incoherent components are combined as a function of the inner microstructure and, thus, about the internal damage. The aim of the proposed method is to provide a quantitative measure of the growth of the damage, assessing any change in the material integrity as a whole. The results obtained from some concrete specimens exposed to different damage processes are analysed and discussed in order to make

an initial assessment of the performance of the new proposed measurement method.

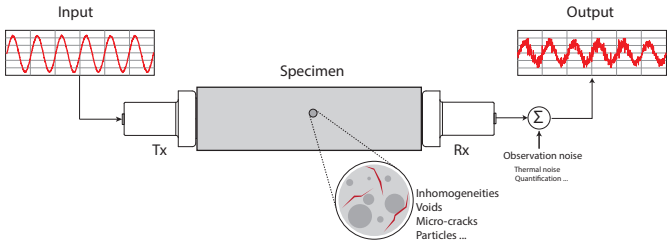

Figure 4.1. Typical ultrasonic inspection of a specimen and examples of input and output signals. The received signal results from many superimposed echoes scattered by the heterogeneous microstructure of the material.

The reminder of this chapter is organized as follows. The new approach based on the signal modality characterization is raised in Section 4.2. Section 4.3 describes the traditional ultrasonic measurements carried out on the specimens to characterized them. The results of predictability are discussed and compared to the foreknown techniques when applied on two different experiences. Section 4.4 describes a typical External Sulphate Attack (ESA) and the damage characterization results estimated by means of destructive and non-destructive techniques; traditional and the new approach. In Section 4.5, the experience of concrete cube specimens damaged under different uniaxial loads is described and characterized. Finally, the conclusions are summarized in Section 4.6.

4.2 Signal Modality Approach based on RQA

Ultrasonic wave has numerous interactions with the internal structure of the material and the data derived from such observations is related to the behaviour of materials at different structure scales (from macro to micro level). The concept of multi-scale interactions can be described starting at the level of atomic bonds, its nanometric scale (gel pores, capillary net mainly made by portlandite and calcium aluminate hydrates), and including that of the mesoscopic (microscopic and millimetric) structure, the aggregate dimension, and finally the concrete structure as a single compo-

nent [66]. The advantage of ultrasonic waves is that they allow access to every level of these interactions by changing the injected frequency, thereby providing a reliable mean of characterising the material at each scale.

The new proposed technique aims to quantify the non-coherent waves produced by echoes from edges and faces of the specimen in addition to the scattering effects from the aggregates. Both, echoes and scattering effects, strongly depend on the structure scale, and therefore, on the working frequency. Particularly, the scattering component of the global attenuation of the ultrasonic wave is well-known to be determined as function of the input frequency (or its corresponding wavelength, λ) and the average size of the aggregates ($\bar{D}$), being identified three different regions: Rayleigh field ($\lambda \ll \bar{D}$), stochastic field ($\lambda \simeq \bar{D}$), and diffusion field ($\lambda > \bar{D}$) [67] (Figure 3.6). The appearing stochastic component depends on the aforementioned ratio and, somehow, summarizes the inhomogeneities seen at the analysed scale and present in the specimen under study. Quantifying the degree of predictability of the time series based on the signal modality characterization concept [68] can provide information about the signal strength of the input deterministic component in relation to the whole time series acquired.

The variation of the degree of determinism related to the frequency of the transmitted ultrasonic wave lets characterise the heterogeneous nature of concrete. Among the different approaches to compute the degree of determinism, in this chapter the algorithm based on the Recurrence Plots is applied (Section 3.2.3). Deterministic values close to 1 mean that the received signal presents a strong deterministic component linked to the input signal which has not been hardly altered, however, deterministic values close to 0 mean that the stochastic component predominates. The evolution of the determinism (in the following called DET) along the frequency (or the equivalent wavelength) allows identifying the different structure scales of the material.

4.3 Traditional Ultrasonic Measurements

For non-continous waves of a specific frequency, f, propagation velocity (or wavefront speed), $v_p(f)$ [m/s], is defined as the speed with which the beginning of the disturbance moves. This value equals the phase velocity and the group velocity as long as they are independent of the wavelength

(non-dispersive materials). The computed $v_p(f)$ is given by Equation 4.1,

$$v_p(f)[m/s] = \frac{d_{mat}[m]}{t_a(f)[s]} \tag{4.1}$$

where $t_a(f)[s]$ is the time that the emitted wave takes to pass through the material (whose distance is d_{mat}[m]) and it is estimated as the instant of time when the received signal level exceeds 50 % of the noise level. This time is proportional to the mechanical constants of the material, and therefore, to the movement of the particles forming the material caused by the applied external forces.

The examination of the amplitude of the signals at different frequencies revealed interesting features related to the aggregate content and size. The attenuative behaviour of the material implies both, intrinsic (absorption) and extrinsic (scattering) mechanism, which cannot be directly separated. The attenuation coefficient, $\alpha_{mat}(f)$ [dB/cm], is determined by measuring the reduction of the amplitude of a sinusoidal permanent wave and is given by Equation 4.2,

$$\alpha_{mat}(f)\ [\text{dB/cm}] = \frac{P_{tx}(f)\ [\text{dB}] - P_{rx}(f)\ [\text{dB}] - \alpha_{equip}(f)\ [\text{dB}]}{d_{mat}\ [\text{cm}]} \tag{4.2}$$

$$P_{tx}\ [\text{dB}] = 10 \cdot \log_{10}\left(\frac{A_{tx}^2}{2}\right) \tag{4.3}$$

$$P_{rx}\ [\text{dB}] = 10 \cdot \log_{10}\left(\frac{A_{rx}^2}{2}\right) = 10 \cdot \log_{10}\left(\frac{\max\{s_{rx}(t)\}^2}{2}\right) \tag{4.4}$$

where P_{tx} [dB] is the transmitted power and can be obtained theoretically from the amplitude of the transmitted signal, A_{tx}, using Equation 4.3, $P_{rx}(f)$ [dB] is the received power and is obtained from Equation 4.4 being $s_{rx}(t)$ the received signal, α_{equip} [dB] is the attenuation of the equipment and d_{mat} [cm] is the total length of the specimen. Note that the transmitted amplitude A_{tx} is a priori knowledge parameters since it is fixed by the user, however, the received amplitude A_{rx} has to be estimated as the maximum of the received ultrasonic signal.

The attenuation associated to the measurement equipment (transducers, amplifier, wires, acquisition module,...), $\alpha_{equip}(f)$, requires a calibration

process [69]. The calibration process was carried out facing emitter and receiver transducers without any material between them and, applying the simplified version of Equation 4.2 which becomes into Equation 4.5. Figure 4.3 plots the resulting frequency response of the used equipment, $-\alpha_{equip}(f)$.

$$\alpha_{equip}(f)\ [\text{dB}] = P_{tx}(f)\ [\text{dB}] - P_{rx}(f)\ [\text{dB}] \tag{4.5}$$

An ultrasonic through-transmission setup was chosen since it offers good penetration and accuracy for the ultrasound measures estimated from the received signal: the p-wave velocity and the attenuation due to the material [70, 71, 72]. The transmitter transducer was excited directly by a programmable signal generator (Agilent 33120A). The received and amplified ultrasonic signal was captured by a digital oscilloscope (Tektronix DPO3014) with a sampling frequency of 50 MHz. And finally, a laptop was used to control the signal generator and to acquire and store the digitized signals by the oscilloscope (see Figure 4.2 for the schematic layout of the experiment).

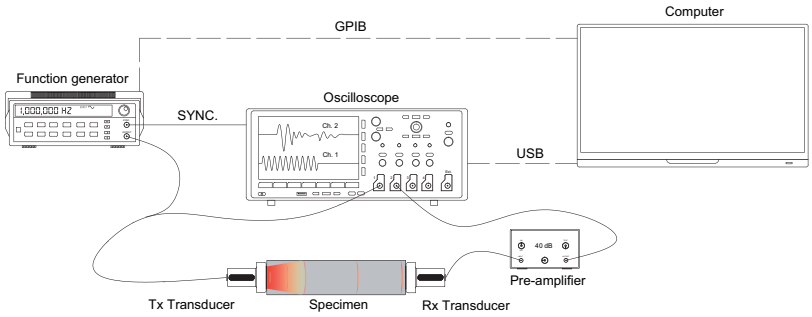

Figure 4.2. Ultrasonic equipment layout: transmission and reception transducers, programmable signal generator, pre-amplifier, digital oscilloscope and a laptop.

4.4 External Sulphate Attack

Concrete is the most widely used synthetic material all over the world in civil and building engineering and architecture. It is composed of water, cement, gravel and sand mixed in different proportions depending on the

kind of mechanical and physico-chemical properties required. This material has an excellent mechanical and structural performance. However, it has important issues in terms of durability when exposed to different environments and harsh conditions. Freeze-thawing cycles, internal sulphate attack (ISA), external sulphate attack (ESA), overload cracking and wet-drying cycles are some of the processes which require early damage detection in order to avoid serious problems involving the structural elements made with concrete.

Of all the problems previously mentioned, in the present research, ESA was selected to damage the concrete, due to its micro-cracking and expansive process (produced by the formation of secondary ettringite), which globally affects the cement paste structure, weakening the different interfaces, and consequently reducing the physical and mechanical integrity of the material.

Ettringite is an expansive compound formed during the Portland cement hydration process (primary ettringite) and also during the lifetime of the concrete structures exposed to sulphate attack (secondary ettringite) [73]. Primary ettringite has no harmful effect on concrete because expansions produced by the reaction between tricalcium aluminate and calcium sulphate in water medium (Eq. 4.6) are absorbed by fresh concrete. Secondary ettringite is formed for months, or even years after concrete has been hardened. The stresses that appear when an external or internal source of sulphate salts reacts with calcium aluminate hydrates can spoil the matrix, causing micro cracks, expansion and spalling. Additionally, gypsum is also formed by reaction of sulphate anions and portlandite (Eq. 4.7).

$$3\,CaSO_4 \cdot 2\,H_2O + Al_2O_3 \cdot 3\,CaO + 24\,H_2O \longrightarrow 3\,CaSO_4 \cdot 3\,CaO \cdot Al_2O_3 \cdot 32\,H_2O \quad (4.6)$$

$$SO_4{}^{2-} + Ca(OH)_2 + 2\,H_2O \longrightarrow CaSO_4 \cdot 2\,H_2O + 2\,OH^- \quad (4.7)$$

4.4.1 Experimental

Two concrete series with two types of cement with different C_3A content and similar mechanical properties were subjected to ESA and evaluated using the traditional ultrasonic measurements and the Recurrence Plot Quantification Analysis (Section 3.2.3).

Materials and specimens

Table 4.1 shows the chemical composition of both types of cement used in this experiment. The main difference between them is the C_3A content: the sulphate resistant cement was a Spanish Portland cement CEM I-52,5 SR (in this study is marked as G) and it has 2.33% of C_3A, and the white Portland cement, BL II A-LL 42.5 R, has 9.84% C_3A (in this study is marked as W).

A plain 0.65 water/cement ratio concrete was designed for this experiment varying the cement type in order to obtain two materials with different chemical properties against ESA. The dosage used for each series is shown in Table 4.2.

Table 4.1. Cement composition by % weight.

Cement type	LOI*	SiO_2	Al_2O_3	Fe_2O_3	CaO	MgO	SO_3	C_4AF	$\mathbf{C_3A}$	C_3S	C_2S
CEM I-52,5 SR	2.05	20.52	3.37	3.92	63.36	1.96	2.59	11.93	2.33	55.7	16.94
BL II A-LL 42.5 R	9.75	16.55	3.88	0.26	62.91	1.39	4.28	0.8	9.84	51.73	8.56

* Loss on ignition

Table 4.2. Concrete dosage in kg.

Series	Cement type	Cement	Water	Gravel 7/12	Gravel 4/7	Sand 0/4
GT0 & GT1	CEM I-52,5 SR	5.25	3.41	5.44	5.44	16.33
WT0 & WT1	BL II A-LL 42.5 R	5.25	3.41	5.44	5.44	16.33

After a properly mixing of raw materials, five 60 x 60 x 240 mm^3 moulds per each series were filled with the fresh concrete and stored into the wet chamber (20 °C and 100 % HR) during 28 days. After that, GT0 and WT0 were tested (samples before sulphate attack), and GT1 and WT1 were stored in the wet chamber immersed in tanks with a 10 % Na_2SO_4 solution for 28 days. Afterwards, GT1 and WT1 (samples after sulphate attack) were tested as the previous series.

Mechanical and Physical Tests

Traditional methods to material damage detection were used in this experimental study following the established standards, three point bending test (Instron universal testing machine, model 3382), compressive strength test (Ibertest MEH LC MD2 W) and transversal dynamic elastic modulus test (determined according to ASTM C 215 02 standard [74]), in order to compare with typical ultrasonic parameters and the new proposed technique.

Ultrasonic Test

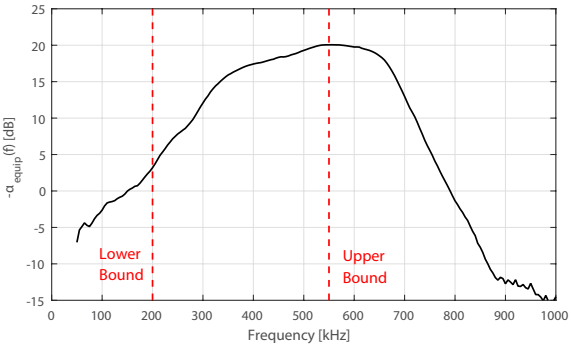

Figure 4.3. Frequency response of the measuring equipment ($-\alpha_{equip}(f)$). Red lines represent the lower (200 kHz) and upper (550 kHz) bounds of the working interval.

An ultrasonic through-transmission setup (Figure 4.2) was chosen since it offers good penetration and accuracy for the ultrasound measures estimated from the received signal: the p-wave velocity and the attenuation due to the material (Figure 4.2). The transducers employed for transmission and reception were the K05SM from General Electric. Both are broadband transducers which bandwidth is centered at 500 kHz. The transmitted signals were different in each performed analysis: a 5 cycles sinusoidal tone burst signal for time-of-flight estimation and a sinusoidal signal for attenuation and signal modality measurements. The wave parameters in both signals were: amplitude, A_{tx} equals 10 V, and the fundamental frequency, f_0, was swept from 200 kHz to 550 kHz in 5 kHz steps. Two aspects were considered for determining the lower bound (200 kHz) of the frequency range: surface waves generating and frequency response of the transducers. For the first one, the maximum ultrasound wavelength λ was chosen to be smaller than the cross section of the specimens (60 mm), so that the wave did not propagate across its entire volume. Otherwise, if the entire volume of the specimen is affected, lamb waves are generated and the propagation velocity becomes depending on the input frequency. Secondly, the frequency response of the equipment and, mainly, of the transducers, limits the working bandwidth. Regarding Figure 4.3, the transducers experimented an efficiency loss and the measurements became unstable below the 200 KHz threshold. On the other hand, the upper bound (550 kHz) of frequency range was chosen considering the amplitude level of the received

signal for the less dispersive series (GT1). For this serie (GT1), frequencies exceeding 550 kHz were highly attenuated. Therefore, the time-of-flight and, as well as, attenuation were estimated inaccurately due to low signal to noise ratio.

4.4.2 Results

Mechanical and physical properties

In Figure 4.4 mechanical results of all series were plotted. As it can be observed, W series have an important decrease on its mechanical properties denoting more weakness than G series against ESA. Figure 4.4(a) shows the compressive strength for material series before (WT0 and GT0) and after the ESA (WT1 and GT1). The differences between WT0 and GT0 are due to the strength class of the cement as described in Section 4.4.1. Moreover, the decay of the compressive strength of WT1 respect to WT0 is notorious as expected, however, this parameter in G series was virtually the same in both cases. Figure 4.4(b) represents flexural strength and a similar behaviour for W series was found. For G series, the median value of the flexural strength is practically the same for both GT0 and GT1, nevertheless, the high dispersion values for GT1 series suggest an initial change triggered by ESA.

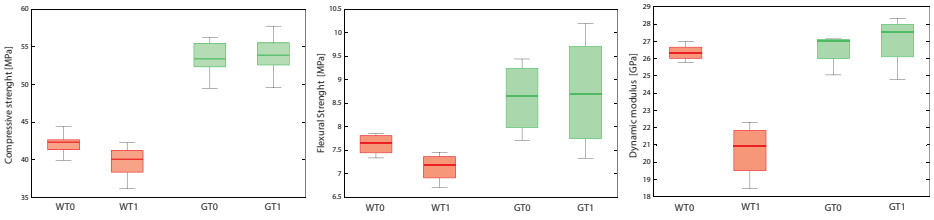

Figure 4.4. Mechanical results obtained for each series. (a) Compressive strength test. (b) Three-point bending test. (c) Transversal dynamic elastic modulus test.

Dynamic modulus of elasticity assess on the stiffness of concrete and is directly proportional to Young's modulus [75, 76]. Unlike the previous mechanical parameters, the initial dynamic modulus for W and G series was the same before ESA (Figure 4.4(c)). W series showed a marked decay from

WT0 to WT1, meanwhile G series shows no difference between GT0 and GT1. All these results confirm the expected behaviour of these concretes in terms of the action of sulphates and the chemical composition of cements.

Traditional ultrasonic measurements

Typical parameters extracted from the ultrasonic wave in time and frequency domains are represented in Figure 4.5. Figure 4.5(a) shows the propagation velocity through the different concrete series. The chosen frequency range avoids surface wave generation and the propagation velocity is equivalent to the p-wave velocity. In the initial state, GT0 had a greater propagation velocity than WT0 due to the cement type used in each mix. However, their behaviour after the ESA was completely different since G series had better durability than W ones. WT1 shows lower values of velocity than WT0 because ESA made significant damage in its internal structure, as it has been previously analysed by the mechanical results. Nevertheless, GT1 had an increment in its wavefront velocity due to the effect of initial stage of ESA. The ettringite formed into pores and capillary network filled the voids and reinforced the microstructure of the material, making it more compact. This behaviour could be supported by the results showed in Figure 4.4(c), that suggest an slightly improvement in the stiffness of the material.

Although concrete has been reported previously to exhibit dispersive behaviour in through transmission layouts, results of this work reveal that the velocity can be considered constant (differs for about 1%) at enough high working frequencies compared to the size of the inhomogeneities. Notice that standard deviation for WT1 and GT1 series is so low that shaded areas are almost undistinguishable. Hereafter, characteristic velocities (the average value) for each series are considered: $v_{p,WT0} = 4250$ m/s, $v_{p,WT1} = 4128$ m/s, $v_{p,GT0} = 4338$ m/s and $v_{p,GT1} = 4389$ m/s.

The attenuation strongly depends on the reflectivity of the material which is related to the scatters (inhomogeneities) of the microstructure. This relationship makes the attenuation a parameter that depends on the size of the reflectors respect to the input signal wavelength. The wavelength (λ) and frequency (f) of a signal are related through the expression $\lambda = v/f$, where v is the characteristic propagation velocity. Figure 4.5(b) shows the attenuation of each series versus the wavelength ranging from low to high frequencies. The corresponding wavelength has been computed using

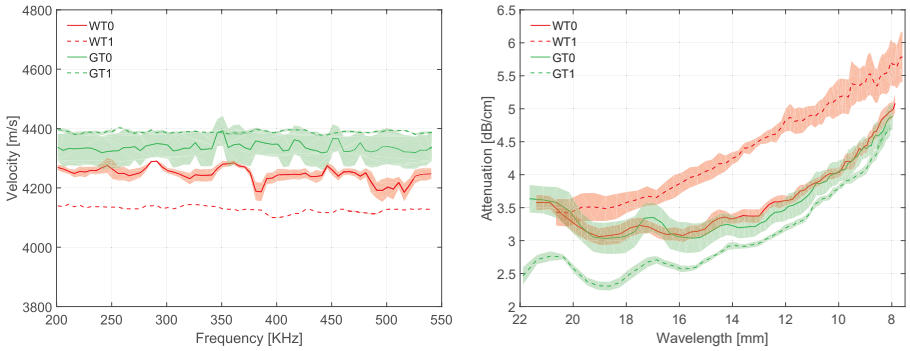

(a) (b)

Figure 4.5. Mean values (lines) and standard deviations (shaded areas) of typical ultrasonic parameters extracted from signals. The x-axis represents the frequency sweep of the input signal expressed in terms of the frequency [KHz], or its corresponding wavelength [mm] stepped by 5 kHz. (a) Ultrasonic p-wave velocity, $v_p(f)$. (b) Attenuation of the material, $\alpha_{mat}(f)$.

the characteristic propagation velocity of each serie and it is related to the size of scatters (reflectors, cracks...) of the tested material. At higher values of frequency (lower values of wavelength), the ultrasonic wave suffers greater number of interactions with the inner structure of the material and, therefore, it implies higher attenuation.

The initial attenuation for both types of cement, WT0 and GT0, is virtually the same, suggesting the integrity of the matrix of the concrete. However after ESA, each material follows a different trend. WT1 serie presents a progressively greater attenuation than WT0 as the input frequency increases (wavelength decreases). For instance, for 12 mm wavelength, WT0 presented 3.5 dB/cm, whereas WT1 presented 4.8 dB/cm. This behaviour is attributed to the appearing microcracking of the cementing matrix which becomes more significant in the case of small structures. For GT1 series, the attenuation decreases after the sulphate attack, a result which supports the aforedescribed filling effect of the capillary network by formation of sulphate bearing compounds. Since the larger pores have more weight to volume level and, therefore, greater presence in the system, the attenuation significantly decreases at low frequencies: for 21 mm wavelength, GT0

presented 3.5 dB/cm whereas GT1 presented 2.7 dB/cm.

RQA results

The degree of determinism must be proportional to the damage suffered by the material. Figure 4.6 compares the reconstructed phase spaces of four ultrasonic signals at the same excitation frequency, $f_0 = 301$ kHz, from different cement concrete series. It can be noticed that trajectories follow similar paths, but each plot has its corresponding stochastic component represented as the dispersion of points in the phase space. Both cement series, GT0 and WT0, have a similar initial stage (Figures 4.6(a) and 4.6(c)) but, due to ESA effect, each series evolved differently at the final stage depending on the effect of expansive products formation. Figure 4.6(b) shows how the serie WT1 has a predominant stochastic component, however, Figure 4.6(d) shows even a stronger deterministic path.

Accordingly, we must be able to characterize each material by applying the RQA parameter. Figure 4.7 plots the value of determinism as function of the signal wavelength. For each acquisition, the phase space has been reconstructed using its optimal embedding parameters. Figure 4.7(a) represents determinism levels for W series. Initially, the determinism (DET) for WT0 decayed from input signals with wavelengths lower than 10 mm. However after ESA, the parameter DET suffers a sudden fall from 16 mm wavelength. This result indicates a signifficant change in the inner structure of the material to which this parameter is sensitive from 16 mm. The wide spread of the standard deviation of the determinism values obtained in the range 10 mm to 16 mm are probably due to the heterogenous cracking process triggered by ESA in each specimen of the serie. Figure 4.7(b) represents determinism levels for G series, both for initial (GT0) and final (GT1) states of the experiment. Although the trends remain the same, the later series present higher values of determinism at every point.

For GT0, GT1 and WT0 series, the determinism curves sharply decreases for high values of frequency (low wavelength values) due to the characteristic inhomogeneities of the matrix-aggregate interface. Note that the ultrasonic sinusoidal signals used in the RQA analysis have not been compensated in terms of calibration. Although that, the curves keep high values of determinism, and the obtained trends cannot be attributed to the system frequency response seen in Figure 4.3. Therefore the technique seems to be robust against the used equipment involved in the measurement process.

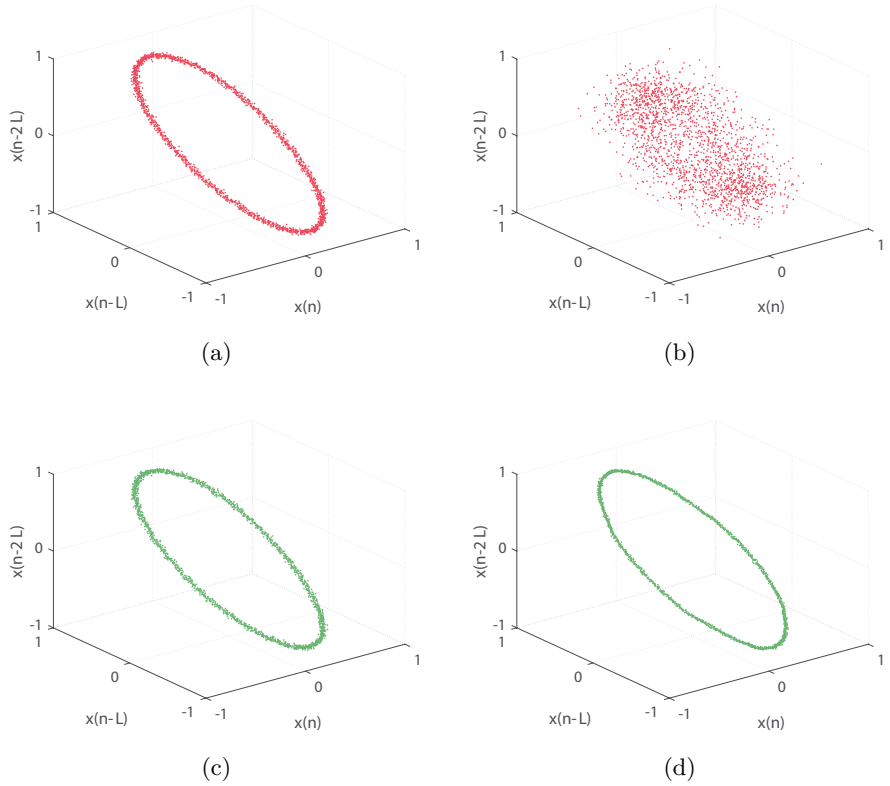

Figure 4.6. Phase space representation of four different signals acquired on four different specimens at the same frequency, $f = 301$ kHz. Each phase space is reconstructed using its optimal embedding parameters, E and L. (a) WT0, (b) WT1, (c) GT0 and (d) GT1.

The results carried out by the new proposed method based on RQA have been probed to be equivalent to the aforementioned both mechanical and ultrasonic traditional methods. The new measuring method could be used not only to characterize damage occurring in materials but also to supplement the information obtained by the attenuation curves. It has been observed that the attenuation can vary both when the frequency increases and if any heterogeneity is appearing. When damaging (or highly heterogeneous material), the injected signal not only must suffer a significant decrease in amplitude but also the random echoes are added to the travel-

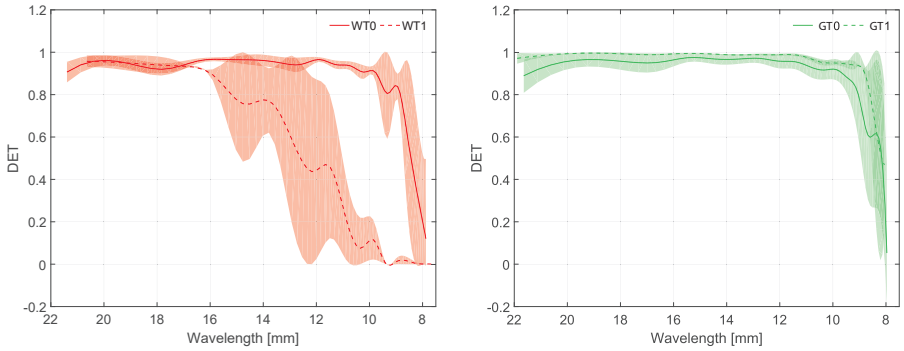

(a) (b)

Figure 4.7. Mean values (lines) and standard deviation (shaded areas) of the RQA parameter DET extracted from the acquired ultrasonic signals. The x-axis represents the frequency sweep of the input signal expressed in terms of the corresponding wavelength [mm], stepped by 5 kHz. The phase spaces are reconstructed using their optimal embedding parameters, E and L. (a) W series. (b) G series.

ling signal, therefore, the rise of the attenuation levels must be accompanied by low values of determinism.

4.5 The cube problem

In this section, a complex damage in concrete cube specimens under different axial loads was assessed using the proposed new technique and comparing the results with the traditional ultrasonic measurements.

4.5.1 Experimental

Material and Specimens

Eight cubic specimens of concrete (water/cement = 0.65) of 100 × 100 × 100 mm^3 were manufactured for this experiment. After the iron moulds were filled with the fresh concrete, they were stored in a wet chamber (20°C and 100% RH) for 24 hours. After that, the specimens were removed from

the moulds and cured under water at 20°C for 60 days. Four specimens were used to determine the ultimate compressive strength of the material and the remaining four were utilized to perform the ultrasonic NDT analysis. These four remaining specimens were subjected to 0%, 25%, 50%, 75% respectively of their ultimate compressive strength (40 MPa) using a calibrated hydraulic press following the scheme in Figure 4.8(a).

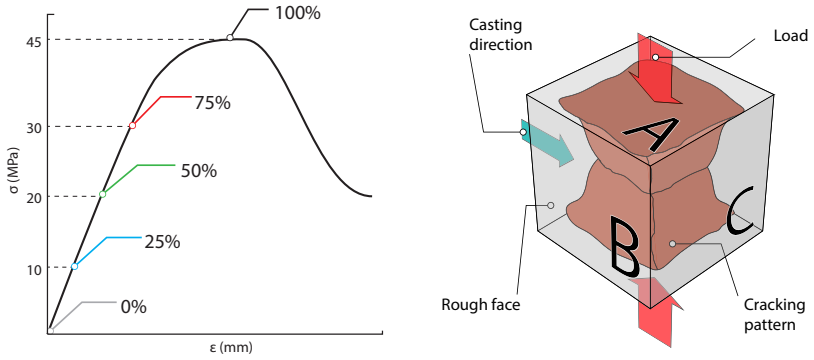

(a) (b)

Figure 4.8. Damage protocol, nomenclature and disposition of the specimens. (4.8(a)) Scheme Stress/Strain curve of concrete with the % of load used for this experiment . (4.8(b)) Nomenclature of the faces, casting and load direction and cracking pattern.

Due to the typical inverted-pyramid cracking pattern of a cube specimen under uniaxial load Figure 4.8(b), direct and indirect ultrasonic through-transmission setups were evaluated. In Figure 4.8(b) , the different faces of a particular cube have been labelled. The two direct ultrasonic configurations were named relatively to the direction of the load. A-$\bar{A}$ corresponds to measures acquired in the direction of the load and B-$\bar{B}$ corresponds to measures acquired perpendicular to the direction of the load. C-$\bar{C}$ configuration could not being measured due to the imperfection of $\bar{C}$ (casting face) generated by the manufacturing process of the specimens that leaves a rough face. The four measured indirect configurations have been classified between parallel and perpendicular to the casting planes (Table 4.3).

Table 4.3. Layout configuration. $\bar{\cdot}$ faces are the opposite parallel faces.

	Direct	Indirect
$\parallel$ Casting Face	A-$\bar{A}$, B-$\bar{B}$	A-B, $\bar{A}$-B
$\perp$ Casting Face	-	A-C, $\bar{A}$-C

Ultrasonic Layout

The layout of the experiment is plotted in Figure 4.2. The transducers employed for transmission and reception were the K1SC from General Electric. Both are broadband transducers whose bandwidth is centered at 1 MHz.

The transmitted signals were different in each performed analysis: a 5 cycles sinusoidal tone burst signal for time of flight estimation and a sinusoidal permanent signal for attenuation and signal modality measurements. The rest of the signal parameters for both cases were: amplitude, $\mathrm{A}_{tx} = 10$ V, and the fundamental frequency, f_0, was swept from 250 kHz to 1.5 MHz in 10 kHz steps (126 measures for each case).

4.5.2 Results

Traditional Ultrasonic Measures

Since the dynamic modulus of the material depends on the square of the propagation velocity, p-wave speed inside the material gives an important information about the loss of stiffness of the concrete caused by the cracking process in the loading phase. Propagation velocity extracted from the ultrasonic wave in the different direct configurations for the whole measured frequency range are represented in Figure 4.9.

At a glance, as the load percentage increments for cube specimens, the wave velocity changes to lower values due to the stiffness loss. Load direction configuration measures (A-$\bar{A}$) are plotted, showing a linear decrease in the velocity. This behaviour matches with 0%, 25% and 50% series in perpendicular configuration measurements (B-$\bar{B}$). Nonetheless, in 75 % load step, an important drop in velocity could be noticed due to the typical aforementioned cracking pattern of the specimens. This behavior makes more noticeable the differences between both dispositions.

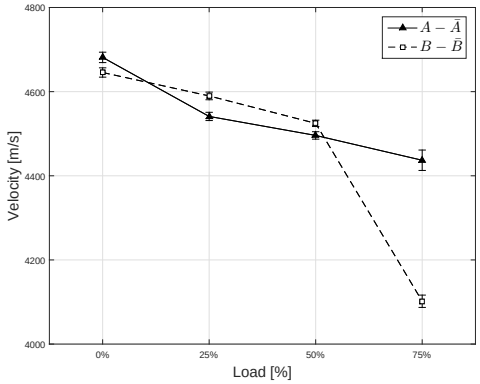

Figure 4.9. Ultrasonic p-wave velocity for direct configurations: load direction A-$\bar{A}$ (solid line), and perpendicular to the load direction B-$\bar{B}$ (dashed line).

Attenuation measures have been plotted according to the layout configurations described in Table 4.3: direct configuration, indirect parallel and indirect perpendicular. Because of inhomogeneities present in the concrete structure (gravel, sand, pore, micro-cracks, voids...), attenuation of elastic waves gives important information about the different mechanisms of absorption and reflection of the material. In this case, such mechanisms depends directly on the cracking pattern of the cubes under the axial load. The afformentioned asymmetry in loading process (and consequent heterogeneity in material state after the load) rises as the stress and subsequent deformation increases, making more noticeable the differences between different configurations. Figure 4.10(a) shows the attenuation curves for direct configuration. It can be observed that 0% series shows the lowest values of attenuation for all frequencies as expected. 25% and 50% showed very similar trends, being 50% series less attenuative than 25% in some cases. 75% series performed the most attenuative behavior in all frequency range, exhibiting a relative huge difference between both configurations. Figure 4.10(b) shows the indirect measures parallel to the rough face. Here, the 0%, 25% and 50% series are quite similar, having the same trend and similar values in all frequencies. 75% series have the highest values of attenuation in the frequency analysis. Figure 4.10(c) shows the indirect measures perpendicular to the rough face, performing quietly the same behaviour in all series and being slightly difficult to distinguish between levels of damage and dispositions.

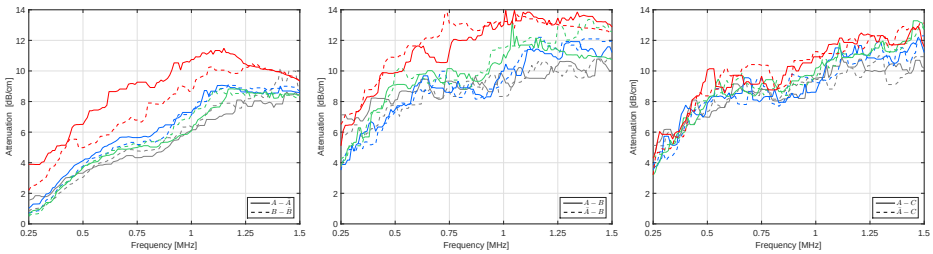

(a) (b) (c)

Figure 4.10. Ultrasonic attenuation for each configuration and level of damage: 0 % (gray), 25 % (green), 50 % (blue) and 75 % (red). (a) Direct configuration: load direction (solid line), and perpendicular to the load direction (dashed line). (b) Indirect configuration parallel to the rough face. (c) Indirect configuration perpendicular to the rough face.

Signal Modality Approach

The degree of determinism quantifies how the pressure waves combine at their propagation path as a function of the inner heterogeneities, and it must be proportional to the damage suffered by the material. Figure 4.11 shows the computed degree of determinism of continuous sinusoidal signals for all series and dispositions. Figure 4.11(a) shows the determinism curves for direct configuration. It can be observed that determinism curves of 0 % drops at high frequencies (1.4 MHz). 25% and 50% performed practically the same behavior, DET drops to 0 values at 1.2-1.3 MHz. 75% series drops under 1 MHz. Figure 4.11(b) illustrates the determinism curves for the indirect configuration parallel to the casting plane. Notable differences can be identified for each level of load, being the differences between the two dispositions bigger as the load increases. Unlike the attenuation curves, the four determinism curves are easily identificable. Lastly, Figure 4.11(c) shows the determinism curves for the indirect configurations perpendicular to rough face. Despite the attenuation curves were very similar, the determinism curves progressively drop and allow identifying the different levels of load. The differences in determinism between the indirect configurations (Figure 4.11(b) and 4.11(c)) might be attributed to the manufacturing process of the concrete cubes (wall effect, compaction process, casting direction, etc.), being the signal modality approach the most

sensitive characterization measure to distinguish between dispositions and levels of load.

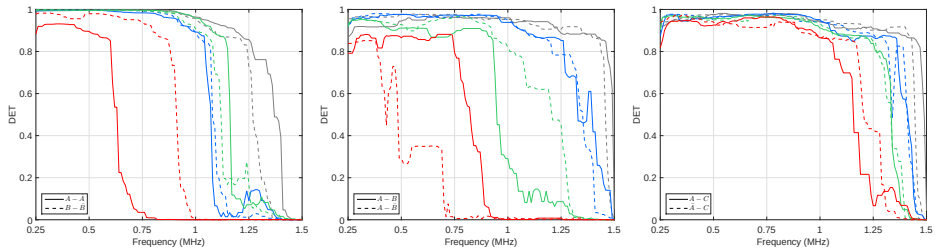

(a) (b) (c)

Figure 4.11. Ultrasonic signal modality for each configuration and level of damage: 0 % (gray), 25 % (green), 50 % (blue) and 75 % (red). (a) Direct configuration: load direction (solid line), and perpendicular to the load direction (dashed line). (b) Indirect configuration parallel to the rough face. (c) Indirect configuration perpendicular to the rough face.

4.6 Conclusions

In this chapter, the approach based on the predictability estimation has been proposed for characterizing material damage using ultrasonic waves. This brand new technique has been widely compared with several methods, such as mechanical tests (compressive and flexural strenght determination), dynamic test (dynamic modulus) measurements, and traditional measurements (propagation velocity and ultrasonic wave attenuation). Two different experiences have been evaluated in order to progressively demonstrate the high sensitivity to damage in spoiled series, improving the reliability of damage detection with ultrasonics in non-homogeneous materials compared to other non-destructive techniques.

In the first experience, two concrete series with two types of cement class with different C_3A content and similar mechanical properties were assessed in terms of External Sulphate Attack. Recurrence Quantification Analysis showed valuable information about the degradation process. In the case of W series, non-deterministic values are reached at higher wavelength values than for the concrete before the sulphate attack. Moreover, damaged W

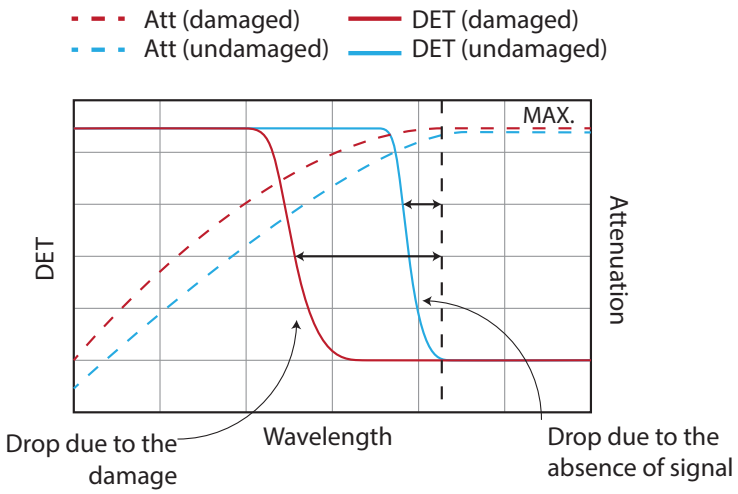

Figure 4.12. Schematic representation of complementary measures attenuation and parameter DET for an undamaged and a damaged specimen.

series showed more dispersion (high standard deviation) in the results than the W series in the initial stage. G series remained constant with slightly changes in the results dispersion.

In the second experience, a detailed ultrasonic analysis of a concrete cube under uniaxial load has been done. The degree of determinism accurately characterizes the level of damage even when many echoes are superimposed and/or the wave-front trajectory cannot be accurately estimated. It has demonstrated its ability to classify between dispositions and levels of load. The typical pyramid-cracking pattern and its exhibited asymmetry due to the concrete heterogeneity has been perfectly analysed in terms of determinism when dispositions in indirect configurations were compared.

In the following, the degree of determinism may be used not only to characterize damage occurring in materials but also to supplement the information obtained by the attenuation curves. It has been observed that the attenuation can vary both when the frequency increases and if any heterogeneity is appearing (Figure 4.12). When damaging (or highly heterogeneous material), the injected signal not only must suffer a significant decrease in amplitude but also the random echoes are added to the travelling signal, therefore, the rise of the attenuation levels must be accompanied by low

values of determinism.

Summarizing, RQA method showed a significant improvement in damage evaluation techniques (destructive and non-destructive ones) for different reasons: DET measure is normalized (0 to 1 range), a calibration process is not required, its standard deviation shows the damage dispersion, it has higher sensitivity in damage detection in some situations and highly contributes to diagnose the degree of damage of a material when is plotted versus the wavelength of the emitted signal. It can greatly contribute to the diagnosis of the degree of damage to a material, when combined with other traditional measures such as the attenuation of the material.

Complexity Characterization 5

Complexity Characterization 5

5.1 Introduction

Detecting non-linearities and complexity in time signals can be used in many situations as an indicator of changes in the underlying dynamical system responsible of the generation of those signals. In some disciplines, the study of these phenomena has been avoided and it is a common practice to model such processes using suboptimal, but mathematically tractable models. However, an adequate detection and characterization of the non-linear and deterministic nature of the signal can convey important information in a large number of situations such as: early symptoms of epileptic detection with EEG signals [77], non-linear phenomena in mammalian voice production [78], stock market predictability [79], river flow discharge rates [80], etc.

Many authors have worked on different techniques to detect and characterize non-linearities in time series. One of the most used methods rely on the Monte-Carlo approach, namely the surrogate data bootstrapping method. This approach is based on the computation of an ensemble of surrogate data which are representative realizations of the null hypothesis

under study. A statistical measure is computed for the original time series and the surrogates. If the statistic is significantly different from the values obtained for the surrogate set, the null hypothesis can be rejected. Therefore, there are three major aspects of the surrogate data method that need to be considered:

- The exact definition of the null hypothesis.
- The realization of the null hypothesis.
- The test statistic.

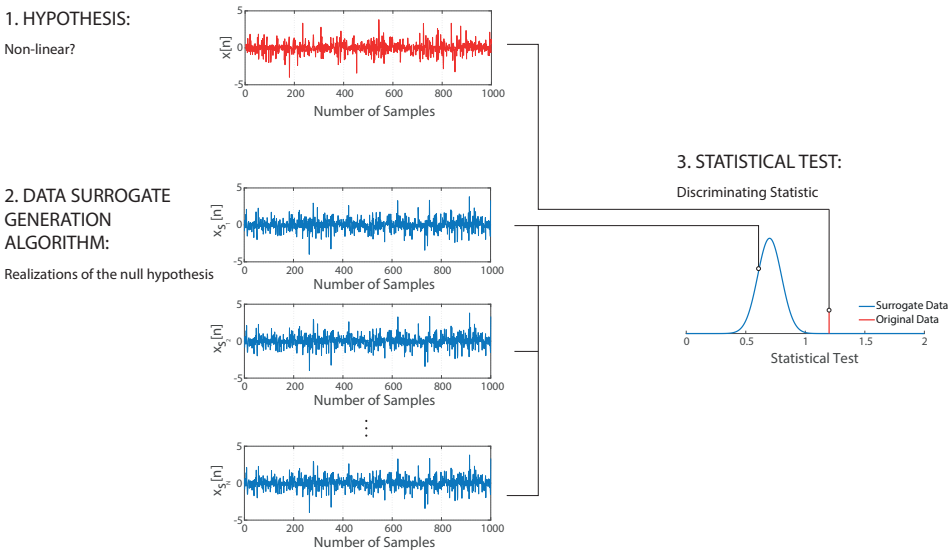

Figure 5.1. Scheme of the surrogate data bootstrapping method.

In the literature, different kinds of surrogate generation algorithms can be found according to the null hypothesis under study: stationarity/non-stationarity [81], determinism/randomness [82], linearity/non-linearity [83, 84], chaos [85], etc. A surrogate data generation algorithm for testing fluctuations and trends in the data is the Small-shuffle surrogate algorithm (SSS) [86], surrogate data generation algorithms for testing pseudo-periodic or oscillating time series are the pseudoperiodic surrogates (PPS) [87] and the twin surrogates (TS) [88] and surrogate data generation algorithms for

testing linearity are the well-known Amplitude Adjusted Fourier Transform (AAFT) [83] and its improved version, the iterative Amplitude Adjusted Fourier Transform (iAAFT) [89]. In each analysis different statistical measures are applied to quantify the differences between the original data and the surrogates. Some of the ones applied in linear analysis are the Kaplans δ-ϵ method [90], the Deterministic Versus Stochastic plots [91], or the Delay Vector Variance (DVV) [92].

Continuing with the line of though of the thesis, the use of the RP may have an important role in the signal modality characterization framework. In this work, we analyse how this visualization tool not only can be applied for the generation of surrogate data but also for the quantification of statistical differences between the original data and the surrogate data. Mainly, we have focused in two main features of signal modality: the characterization of the linear/non-linear nature of a signal and its complexity.

To explain these ideas, the phase space and the RP definitions are going to be employed in the rest of the chapter. The expression of the phase space reconstruction for a given N-point signal $x[n]$ for an embedding dimension E and a time lag L is used to compute the Delay Vectors DVs, $\vec{X}_{L,E}$ (Eq. 2.3). Every delay vector DV has a corresponding target, basically, the next sample $x_t[n] = x[n+1]$ [93]. The proper selection of E and L is done according to the procedure studied in Chapter 2.

The remaining of this work is structure as follows. In Section 5.2 we will present a selection of surrogate techniques that can be applied in real signals in order to test the linear/non-linear nature having non-stationary behaviour and to test for oscillatory signals having higher complexity than a quasi-periodic orbit. In Section 5.3 we will illustrate how by means of RQA new discriminating measures for non-linear statistical tests can be devised. In Section 5.4 some examples of signal modality characterization are summarized, both with simulated and real signals. Finally, we will present the conclusions in Section 5.5.

5.2 Surrogates

Theiler et al. [83] introduced the concept of 'surrogate data', which has been extensively used in the context of statistical non-linearity testing. A surrogate time series, or surrogate for short, is generated as a realization of

the null hypothesis under study. So given an original signal, realizations of this data must be generated only modifying the desired characteristic of the signal which is being tested remaining all the rest of properties. Care must be taken when using surrogate data to ensure that statistical differences come from the desired characteristic and not from an undesired one, such as a failure of the surrogate algorithm to mimic non-stationary data. Choosing a surrogate technique that does not mimic these fluctuations or changes the statistical distribution may lead to false positives.

We next present two techniques for the generation of surrogates which will be used later in statistical analysis based on RQA. The first one is used to detect the presence of non-linearities whereas the second one uses RP concepts to generate surrogates valid for testing high complexity in short oscillatory signals.

5.2.1 Testing non-linearity

One of the key issues in signal modality is the definition of a linear signal. The standard definition is that such a signal is generated by a Gaussian linear stochastic process. Based on this definition the null hypothesis remains on the properties of any AR-model driven by white noise. Since any AR-model can be described by its amplitude spectrum and, therefore, the phase spectrum is irrelevant, most of surrogate data generation algorithm for testing linearity are based on a phase spectrum randomization. The most common established method for generating constrained surrogates is the Iterative Amplitude Adjusted Fourier Transform (iAAFT) [89].

Iterative Amplitude Adjusted Fourier Transform (iAAFT)

Let $x[n]$ be the original time series, $s[k]$ the sorted version of $x[n]$ and $X[f]$ the Fourier transform of the original data series. The original iAAFT algorithm is based on the following steps:

1. Make a random permutation of the time samples of the original time series $x[n]$, namely $r[n]$.

2. Compute the phase spectrum of $r[n]$, namely $\phi[f]$.

3. Compute the Inverse Fourier Transform of $\{|X[f]|\cdot exp(j\phi[f])\}$, namely $c[n]$.

4. Obtain a new version of the time series $r[n]$ by rank-ordering (sort in increasing order) $c[n]$ so as to match $s[k]$.

5. Repeat steps 2-4 until the discrepancy between $|X[f]|$ and the amplitude spectrum of $r[n]$ is lower than a chosen tolerance.

This iterative algorithm has been shown to converge after a finite number of steps [89]. Each initial random permutation gives a different output surrogate data $r[n]$ with identical signal distribution and approximately identical amplitude spectra as the original signal.

Figure 5.2 shows an example of a surrogate data of the AR model seen in Eq. 2.20. Figure 5.2(a) compares the temporal evolution of the original data (blue) and the surrogate data (red). Both realization share the same statistical distribution (Fig. 5.2(b)), as well as their amplitude spectrum (Fig.5.2(c)). However, according to the algorithm, the resulting surrogate data presents a random behaviour of the spectrum (Fig. 5.2(d)).

The process of generating surrogates always starts with a finite length time series with an initial value ($x[0]$) and a final value ($x[N-1]$). Special attention must be taken when generating surrogate data of stationary signals which extremes may be different significantly ($x[0] \neq x[N-1]$). Due to the use of the Fourier Transform, the periodicity of the signal is assumed and the interval of the signal must correspond to an hypothetical periodic signal (or an integer number of it). Otherwise, the resulting surrogate data may significantly differ on its temporal domain, the discriminating test will fail, and the null hypothesis automatically accepted. An example of this is illustrated in Figure 5.3 where we show two resulting surrogate data of a sinusoidal signal for both cases: upper part of the panel, both extremes of the interval are carefully chosen to simulate a periodic interval of the signal; lower part of the panel, extremes of the original time signal significantly differ. Note that in the second case, the surrogate does not model the original data despite the amplitude Fourier Transform closely match.

The original iAAFT method has recently been refined in order not only to retain the signal distribution and amplitude spectrum of the original time series, but also the local mean and variance of the original time series [94]. This new approach uses a wavelet transform to preserve the behaviour in the time-frequency plane. It makes this new technique most suitable to non-stationary signals which time-changing properties that would be destroyed using the original iAAFT algorithm.

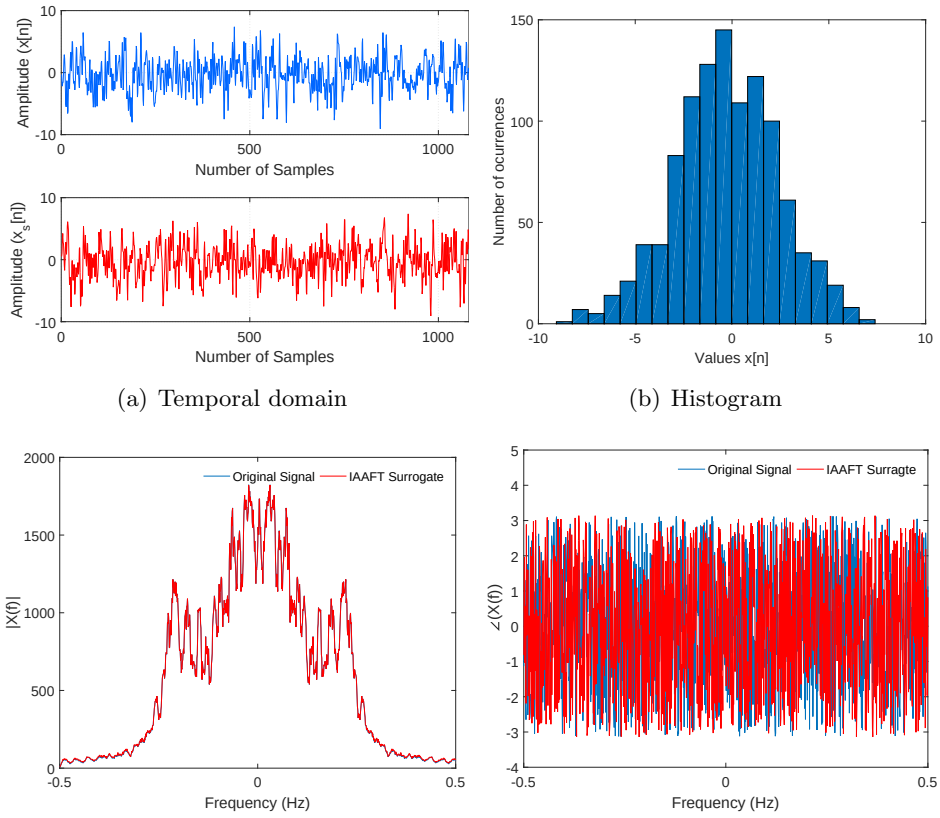

(a) Temporal domain (b) Histogram

(c) Amplitude Spectrum (d) Phase Spectrum

Figure 5.2. Example of a surrogate data generation algorithm iAAFT for a realization of Model I (Eq. 2.20).

Wavelet Iterative Amplitude Adjusted Fourier Transform (WiAAFT)

Let $x[n]$ be the N-point original time series and $s[n]$ the sorted version, $x[n]$ is decomposed in J scales, where $N = 2^J$, the scales j ranges $j = 1, 2, \ldots, J$. The WiAAFT algorithm can be summarized as follows:

1. Compute the Maximal Overlap Discrete Wavelet Transform (MODWT) of the original time series $x[n]$ using a high number of vanishing moments to deal with any potential non-stationarity in the series [95]. The result is a wavelet detail coefficients at each scale j, c_j.

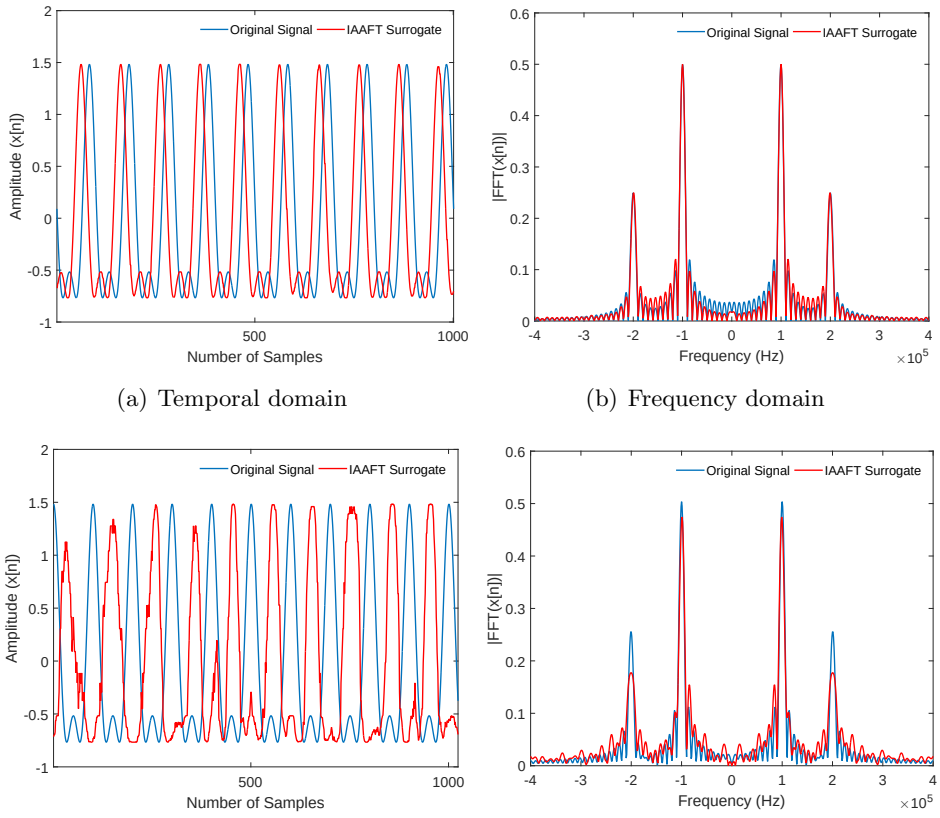

(a) Temporal domain

(b) Frequency domain

(c) Temporal domain

(d) Frequency domain

Figure 5.3. Example of the potential pitfalls one can have when using the iAAFT in sinusoidal signals.

2. Apply the iAAFT algorithm to each c_j to generate a constrained realization of the original detail coefficients, c'_j, preserving the original values and their periodicity.

3. Transpose c'_j so that the first detail coefficient in the transposed case is the last in the new variant, c''_j.

4. Find the best match in each scale between c_j and the two variants, c'_j and c''_j, by circularly rotating until an error function is minimized. In this work, least-squares is used. This will mean that the positions with high energies in the original data are mimicked in the surrogates.

5. Invert the MODWT (using the original approximation coefficients) to yield a surrogate dataset, $w[n]$.

6. Perform rank-ordering (sort in increasing order) to $w[n]$ so as to match $s[n]$.

7. Use the new time series $w[n]$ as the initialization of the described iAAFT algorithm (Step 2 where $r[n] = w[n]$).

Therefore, this new approach represents the seed for the original iAAFT giving a closer solution to the original data. Figure 5.4 compares the surrogate data computed with the original iAAFT algorithm and the new WiAAFT for a heart rate variability signal (HRV) recorded during a meditation session. HRV signals are widely used to analyse humans health, however, one of the main challenges from the signal processing point of view is the presence of many artefacts or temporal changes in the recorded time series due to different factors such as patient motion, eye blinking, etc. The blue line represents the original time series. The green line corresponds to the surrogate data computed using the iAAFT. Note that the iAAFT has almost destroyed the temporal structure of the original signal. The red line plots the surrogate data computed with the WiAAFT, which though still is a random realization compared with the original signal it highly preserves the time evolution of the original data.

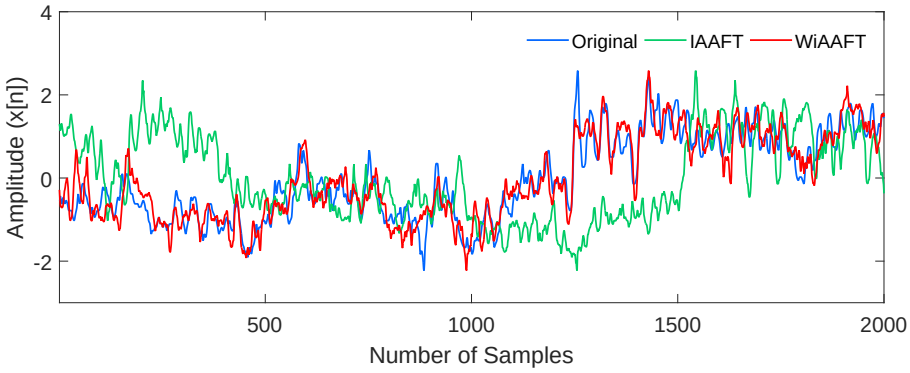

Figure 5.4. Comparison between two surrogate data generation algorithms: iAAFT and WiAAFT, for a heart rate variability signal (HRV) recorded during a meditation session.

5.2.2 Testing complexity

Oscillatory signals can be frequently found in the solution of real world problems. Sometimes these signals have a high complexity in the oscillations that may evidence the presence of non-linearities. Some examples are: the study of bi-phonation, sub-harmonics or other pathologies in animal sounds [96], the study of non-linearities in ultrasonic signals [97], etc. In most of these problems conventional surrogates have a limited use, mainly due to the finite duration of the events that need to be analysed and to the sensitivity that needs to be achieved. Some of the techniques that rely on the Fourier Transform require long data series and thus, specific algorithms for the generation of surrogates in short length oscillating data have to be devised.

In the literature, there are two methods that preserve the higher order moments for the surrogate generation of oscillatory signals [87, 98]. The first method, called pseudoperiodic surrogates (PPS), was proposed in [87] by Small et al. (2001). It mimics the phase space of the original data, by adding some dynamic noise in such a way that any existing fine dynamics (which are closely related to chaos) are destroyed. This method was first proposed to test the null hypothesis that an observed time series is consistent with an (uncorrelated) noise-driven periodic orbit. However, this method does not provide good results when applied to the problem of characterizing/ differentiating complex patterns of amplitude modulation (chaos) from quasi-periodic signals obtained as the sum of sinusoids with incommensurate frequencies. The amount of dynamic noise that needs to be added to remove the fine patterns in an oscillatory signal strongly depends on the complexity of the signal (more complex signals need more dynamic noise to remove details). Thus, the method cannot be applied to compare two low-noise oscillatory orbits that have a different degree of complexity. The second method, called twin surrogates (TS), was proposed in [98] by Thiel et al. (2006). It reproduces the trajectory of the underlying system by visiting the attractor in a different way. These surrogates were devised to test for complex synchronization problems. Importantly, this algorithm can also be used to distinguish chaos from quasi-periodicity using RQA. To this end we have to deal with some practical implementation problems when generating surrogates with the TS algorithm for short time series (such us the limited number of twins [99]). We propose combining both algorithms (PPS and TS) to introduce a new surrogate generation

algorithm to the characterization of complexity of oscillatory signals.

Pseudo-Periodic Twin Surrogates (PPTS)

The PPTS algorithm uses the phase space and RP concepts in order to obtain the surrogates. This is achieved embarking upon the idea of jumping among twin points in the same way the TS algorithm does. Twin points are points which are not only neighbors $||\vec{X}[i]-\vec{X}[j]|| < \varepsilon_{TP}$; but also share the same neighbourhood $RP(i,l) = RP(j,l)\ \forall l$. The choice of ε_{TP} is not crucial; it has been shown in [98] that a choice of ε_{TP} corresponding to 5% -10% of black points in the RP is appropriate. Twin points are indistinguishable regarding their neighbourhoods, but, in general, they have different pasts and, more importantly, different futures. Surrogates can be generated by changing the structures in the RP consistently with those produced by the underlying dynamical system. Jumping among twin points produces surrogates with very similar RP representations to the RP representation of the original signal if the time signal is periodic or quasi-periodic (similar futures). In contrast, jumping among twin points produces surrogates with quite different RP representations for a chaotic signal.

Unfortunately, jumping among twin points is not always enough to generate surrogates that allow to stablish the confidence level for null test rejection. Additionally, there exist some practical implementation problems with the TS algorithm for short time series (such us the limited number of twins [99]). Thus, the PPTS algorithm uses a second randomization technique. It consists in moving from point to point in the phase space in accordance with a probability that is inversely proportional to the distance between the two points (Eq. 5.1). The proposed PPTS algorithm is summarized as follows:

1. Compute the RP of the original signal using Eq. 2.11, with an appropriate choice of ε, denoted by ε_{TP}, and identify the twin points ($RP(i,l) = R(j,l)\ \forall l$).
2. Randomly choose an initial condition i_0 and make $i = i_0$. Initialize $n = 1$.
3. If there is a twin point for $\vec{X}[i]$, make the next point of the surrogate $\vec{X_s}[n] = \vec{X}[j]$, where j is randomly chosen among the twin points with the probability $1/T$ (T is the number of twin points for the state $\vec{X}[i]$). Let $i = j$ and $n = n + 1$.

4. For $\vec{X}[i]$, choose a neighbour $\vec{X}[j]$ from all of the elements of the phase space representation ($j = m \cdot \tau, \ldots, N-1$) with probability

$$Prob(\vec{X}[j]) \propto exp\frac{-||\vec{X}[i] - \vec{X}[j]||}{\rho} \tag{5.1}$$

where ρ is the noise radius studied in [87]. Make the next point of the surrogate $\vec{X_s}[n] = \vec{X}[j]$. Let $i = j$ and $n = n + 1$.

5. Repeat from Step (3) until $n = N$.

The surrogate is formed from the first scalar component of $\vec{X_s}[n]$.

The proposed PPTS algorithm generates surrogates that are very similar to the original signal as long as the original signal is periodic or quasi-periodic. When the original signal deviates from a periodic or quasi-periodic oscillation the PPTS generates surrogates that have quite a different RP matrix while still preserving the approximate phase space shape of the original signal. Thus, these surrogates are appropriate for testing the null hypothesis that the observed time series is consistent with a quasi-periodic orbit. This is going to be illustrated in the following example (all the PPTS examples in this work were computed using a ε_{TP} corresponding to 10 % of black points in the RP).

Consider the following signals: a quasi-periodic time series composed of the sum of two sinusoids with incommensurate frequencies [100] and a Rössler chaotic time series. The quasi-periodic signal was generated as given by:

$$x(t) = 8 \cdot sin(2 \cdot \pi \ f_1 \cdot t) + 4 \cdot sin(2 \cdot \pi \ \cdot f_2 \cdot t) \tag{5.2}$$

where $f_1 = \sqrt{3}$ Hz, $f_2 = \sqrt{5}$ Hz. The discrete time series version $x[n]$ is obtained using a sample period of $\Delta t = 0.02$. We only generate 400 samples of this signal. The Rössler signal is generated as given by Equation 2.14 seen in Section 2.4. Figure 5.5 illustrates the phase space reconstruction (with $E = 3$ and $L = 6$) of the original quasiperiodic time series, the PPS and the PPTS. When comparing the PPS and the PPTS, it can be observed that for quasi-periodic signals, both algorithms achieved similar phase space reconstructions. Note that 2-D projections have been plotted.

The phase space reconstruction of the Rössler signal is shown in Figure 5.6. In this case two examples of the PPS were compared. When comparing Figure 5.6(b) and 5.6(d), it can be observed that for the same noise

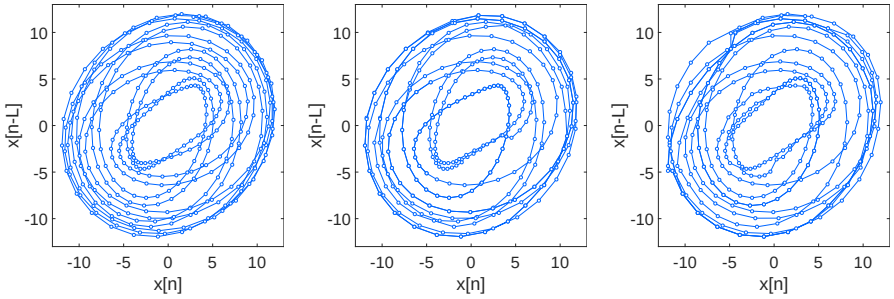

(a) Original (b) PPS (c) PPTS

Figure 5.5. Phase space reconstruction of a sum of sine waves. (a) Quasi-periodic time series. (b) Surrogates obtained with the PPS algorithm ($\rho = 0.25$). (c) Surrogates obtained with the proposed PPTS algorithm ($\rho = 0.25$).

radius ($\rho = 0.25$), the proposed PPTS algorithm achieves a phase-space representation that removes most of the details which evidence chaos (the large number of trajectories that run arbitrarily close together) while at the same time preserving the shape of the original time series. The PPS algorithm would need a higher noise radius ($\rho = 0.55$) to produce similar detail removal (Fig. 5.6(c)). However, using such a high noise radius will produce noisy surrogates, and this lowering of the signal to noise ratio is always inherent in the null test hypothesis of the PPS.

These two examples also show one of the weak points of the PPS algorithm when it is used to compare the complexity between orbits: the selection of the noise radius (ρ). The selection of the noise radius in the PPS is strongly related to the amount of detail that has to be removed. Thus, signals that have a chaotic structure require higher values of ρ than signals that do not have that structure. This makes the PPS algorithm unsuitable for distinguishing between chaotic and quasi-periodic time series with comparable noise levels. The proposed PPTS algorithm overcomes this weakness and achieves enough detail removal regardless of whether the signal is chaotic or quasi-periodic; therefore, it can be used as a feasible alternative to establish the confidence intervals when testing for quasi-periodic deviation.

All these details are also captured and represented in the structures of the RPs (see Fig. 5.7). The appropriated metrics for testing with the PPTS (or some of the rest of the presented surrogates) can then be obtained by

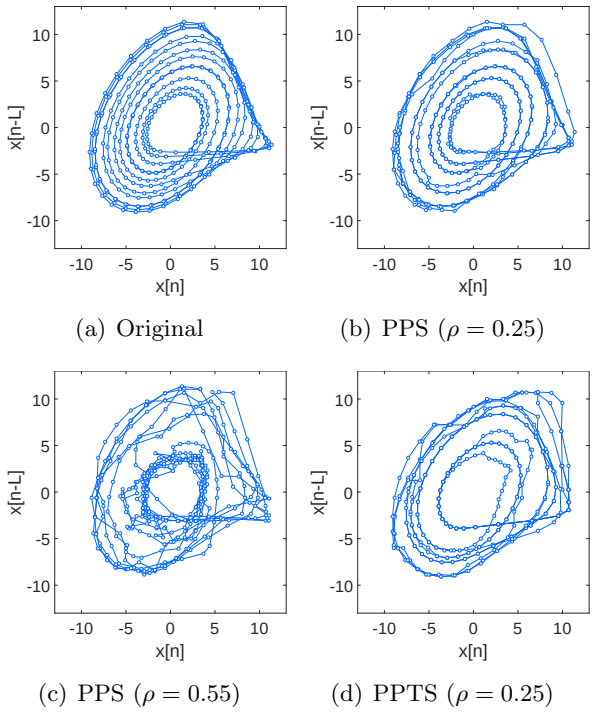

(a) Original (b) PPS ($\rho = 0.25$)

(c) PPS ($\rho = 0.55$) (d) PPTS ($\rho = 0.25$)

Figure 5.6. Phase space reconstruction of Rössler attractor. (a) Rössler chaotic time series. (b) PPS algorithm ($\rho = 0.25$). (c) PPS algorithm ($\rho = 0.55$). (d) PPTS algorithm ($\rho = 0.25$).

means of the RQA. This idea, that will be developed in the following section, will allow us to create tests to distinguish between oscillatory signals with different complex patterns of amplitude modulation.

5.3 Discriminating Statistics

In order to test the null hypothesis of linearity, a statistical discriminating measure has to be performed on both the original data and the surrogates. Many different techniques and statistical tests have been suggested for this purpose. Some of the discriminating statistics are based on computing Lyapunov exponents, return maps or some other graphs or functions representative of the topology of the underlying dynamics. The computation

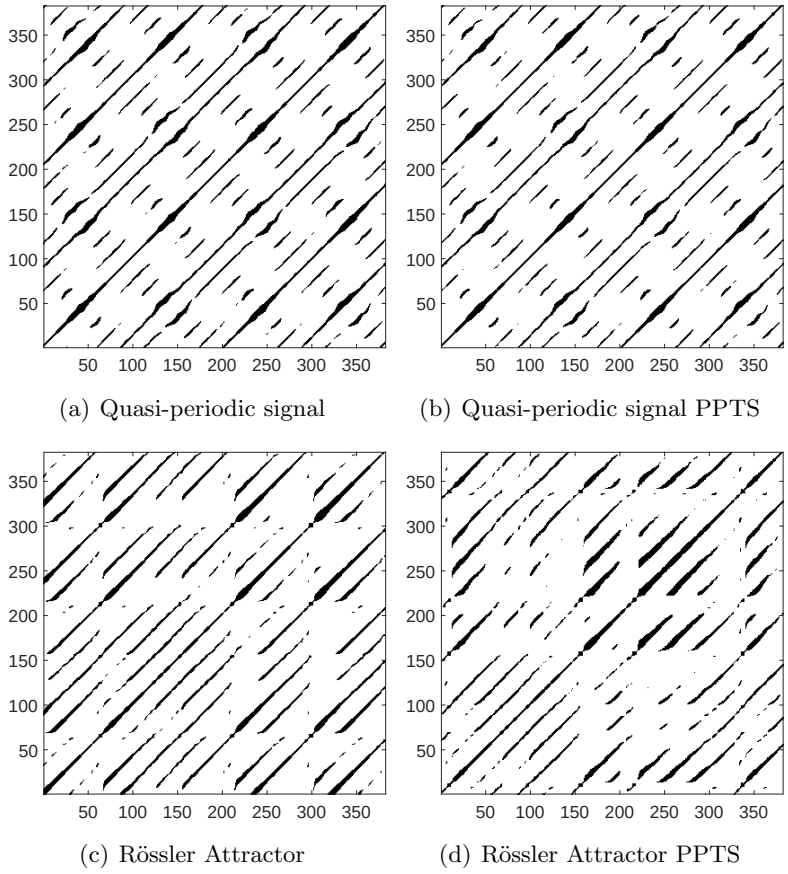

(a) Quasi-periodic signal (b) Quasi-periodic signal PPTS

(c) Rössler Attractor (d) Rössler Attractor PPTS

Figure 5.7. (a)RP representation of the Rössler attractor. (b) RP representation of the PPTS for the Rössler attractor . (c) RP representation of the quasi-periodic time series. (d) RP representation of the PPTS for the quasi-periodic time series. The PPTS were computed with ε_{TP} corresponding to 10% of black points in the RP and a $\rho = 0.25$.

of these functions may be quite complex in real world signals. As a result of this difficulty, a large number of techniques that compute a much more simple graphical representation of the underlying system have been developed. Some of the most cited methods are the Deterministic Versus Stochastic plots [91], the Kaplans - method [90], the correlation exponent [101], or the Delay Vector Variance (DVV) [92].

All these methods introduce, alongside with the already presented DVs (Eq. 2.3), the concept of the target of the DV $x_t[n]$. The idea underpinning these methods is that the study of the evolution functions $\mathbf{f}(\cdot)$ (continuous systems, Eq. 2.1) or $\mathbf{F}(\cdot)$ (discrete systems, Eq. 2.2) which maps the DVs onto their corresponding targets. The analysis is done by means of the locality of the unknown models, when combined with the method of the surrogates provides information of the non-linear behaviour of the underlying process. The degree of locality of a time series is closely related to the distribution of the nearest neighbour points, however, each method analyses the locality degree using different approaches: mean of the targets, variance of the targets, prediction error, etc. Despite of the fact, none of the techniques exploits the advantages of the RP and, therefore of the RQA.

The RPs can widely help in designing robust and less parameter dependent tests for non-linearity detection. In the following section, a detailed analysis of one of the aforementioned methods is done in order to further understand the motivation of this new approach and its potential.

5.3.1 Delay Vector Variance

The delay vector variance (DVV) method is a phase space based technique which examines the deterministic nature of a time series and when combined with the method of surrogates data provides information of the non-linear behavior of the underlying process.

The DVV method can be summarized as follows [92].

1. Given the optimal embedding parameters, E and L, generate the delay vectors (DVs) following Eq. 2.3. Every DV, $\vec{X}[n]$, has a corresponding target, namely the next sample $x_t[n]$.

2. The mean, μ_d, and the standard deviation, σ_d, are computed over all pairwise Euclidean distances between DVs, $||\vec{X}[i] - \vec{X}[j]||(i \neq j)$.

3. The sets $\Omega_k(r_d)$ are generated such that:

$$\Omega_k(r_d) = \left\{ \vec{X}[i] \mid ||\vec{X}[k] - \vec{X}[i]|| \leq r_d \right\}$$

   i.e., sets which consist of all DVs that lie closer to $\vec{X}[k]$ than a certain distance r_d, taken from the interval $[max\{0, \mu_d - n_d\sigma_d\}]$, e.g., N_{tv}

uniformly spaced distances, where n_d is a parameter controlling the span over which to perform the DVV analysis.

4. For every set $\Omega_k(r_d)$, the variance of the corresponding targets, $\sigma_k^2(r_d)$, is computed. The average over all sets $\Omega_k(r_d)$, normalized by the variance of the time series, σ_x, yields the target variance, $\sigma^{*2}(r_d)$:

$$\sigma^{*2}(r_d) = \frac{\frac{1}{N_0}\sum_{k=1}^{N_0}\sigma_k^2(r_d)}{\sigma_x^2}, \tag{5.3}$$

where N_0 denotes the total number of sets $\Omega_k(r_d)$.

5. Repeat steps 1 to 4 for the N_s surrogates.

The DVV analysis can be conveniently illustrated in the resulting DVV plots where the x-axis corresponds to the standardized distance r_d, and the y-axis corresponds to the target variance. If the surrogate data yield similar results to that of the original signal, the target variance of the original signal fall into the confidence interval and the null hypothesis cannot be rejected. Figure 5.8 shows the DVV analysis for two deterministic examples where the input parameters were $N_{tv} = 50$ uniformly spaced distances, $n_d = 3$ and $N_s = 99$ surrogates. Each signal phase space was reconstructed using its corresponding embedding parameters (E and L). The quasi-periodic signal (Eq. 5.2 , Fig. 5.8(a)) results in a linear example where the original signal target variance falls into the surrogate data distribution. However, for the Rössler atractor analysis (Eq. 2.14, Fig. 5.8(b)) the linear surrogates computed by the iAAFT algorithm yield variance vectors different from the original signal.

Due to the standardization of the intervals of r_d, both statistics from the original and the surrogates can be jointly represented in the so-called DVV plots. The x-axis corresponds to the original target variance, and the y-axis represented as an errorbar represents the surrogate target variances. When the signal under study has a linear nature, the distribution will correspond to the bisector line, otherwise, they will not match. Figure 5.9 presents both previous examples: panel a), the quasi-periodic signal; panel b) the Rössler attractor. We also present in Figure 5.9 the DVV plots of two stochastic processes. Figure 5.9(c) represents the DVV analysis for Model I (Eq. 2.20) and Figure 5.9(d) represents the DVV analysis for Model II (Eq. 2.21).

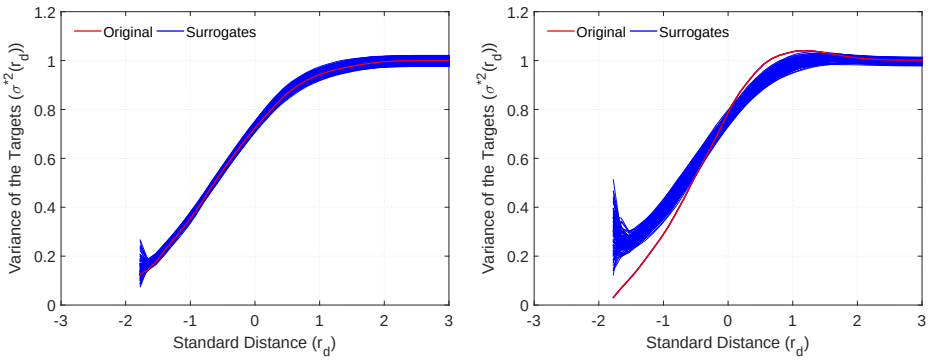

(a) Quasi-periodic signal (b) Rössler Attractor

Figure 5.8. DVV analysis for two deterministic examples. The input parameters were $N_{tv} = 50$, $n_d = 3$ and $N_s = 99$ surrogates.

The potentiality of this technique not only resides on its capability to detect non-linear behaviour but also to do it based on the randomness/ deterministic nature of the signal. In Figure 5.9, note that for the deterministic signals (upper part of the panel) the target variance vector has the lowest value under 0.2, however, in the case of stochastic signals, the lowest values (above part of the panel) are greater. Therefore, this technique is able to both characterise the degree of uncertainty and linearity simultaneously.

Despite of the potentiality of the technique both when characterising the deterministic/randomness of the signal, and its linear/non-linearity, the authors are quite critical when applying it to real signal due to two main aspects both related to the non-stationarities habitually present in real complex signal. The first issue is not strictly related to the DVV algorithm but to the iAAFT algorithm. It is mostly solved by the usage of the WiAAFT algorithm presented in Section 5.2.1. The second is related to the estimator applied on the targets points. It allows the study of the evolution function for the original signals and the surrogates, however, it might not be robust on real signals. In the following both issues are discussed:

- The original iAAFT algorithm is substituted by the recently proposed WiAAFT.
- The statistical test computed on the target domain based on the

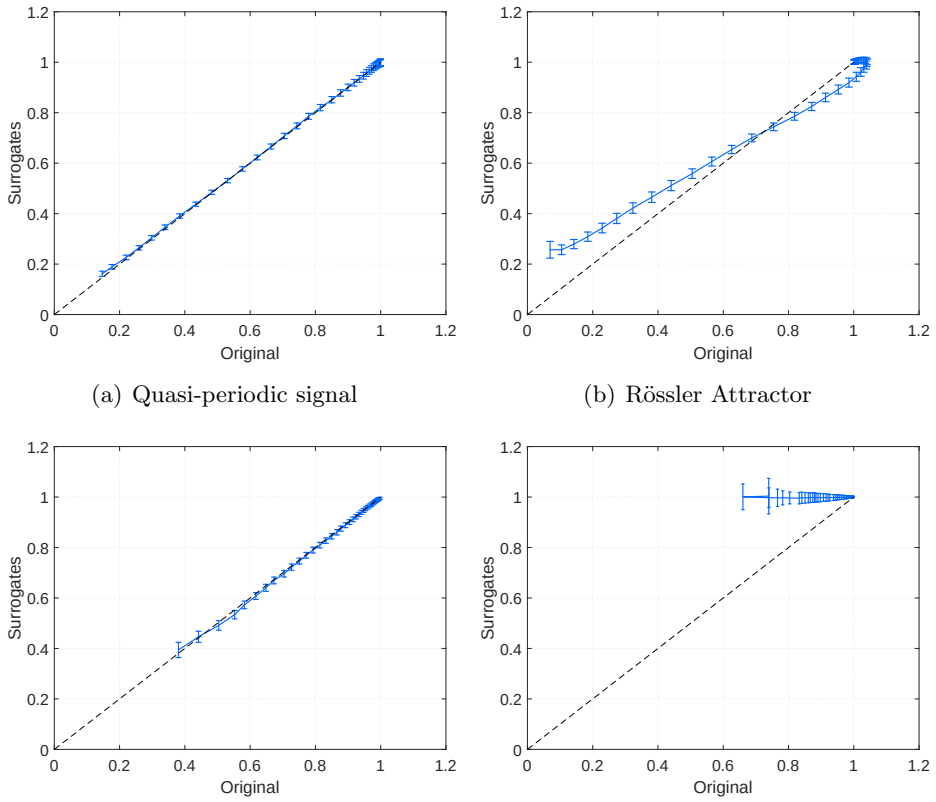

(a) Quasi-periodic signal

(b) Rössler Attractor

(c) Model I

(d) Model II

Figure 5.9. DVV plots for two deterministic (a) and b)), and two stochastic (c) and d)) examples. The input parameters were $N_{tv} = 50$, $n_d = 3$ and $N_s = 99$ surrogates.

variance estimator is modified by the usage of any RQA measure.

5.3.2 Reformulation of the DVV using RPs

Those readers familiar with the RPs may readily understand that the computation of the DVV plot can be explained by using RP concepts. The RP is a 2D plot showing, for a given moment in time, the times at which a phase space trajectory visits roughly the same area in the phase space. As a result of that, for a given DV from the RP we can easily found the DVs that are closer than a given distance r_d, completely equivalent to the so

called ε in the RP (Eq. 2.11), just by looking in the corresponding column of the RP(ε). Figure 5.10 illustrates this idea and shows how we can obtain the corresponding set of targets (horizontal red and green lines), $\Omega_k(r_d)$ in the DVV algorithm, for the later computation of its variance. The red and green vertical lines are two randomly chosen DVs ($\vec{x}(i_0)$ and $\vec{x}(i_1)$ respectively $E = 3$, $L = 1$) represented in the bottom panel using asterisks. The red and green horizontal dashed lines are their corresponding neighbours lying within the distance ε. The red circles in the left panel are the corresponding targets of $\vec{x}(i_0)$ whereas the green squares are the corresponding targets of $\vec{x}(i_1)$. The RP was computed for an ε corresponding to 14 % of black points.

In this way, for a given i_0 and ε, we obtain $l_\varepsilon \subseteq \{j\}$ s.t. $R_{i_0 j} = 1$, and $\sigma^2_{i0}(\varepsilon) = VAR[x_{l_\varepsilon}]$, where $VAR[\cdot]$ is a variance estimator and x_{l_ε} is the target of the DV $\vec{x}(l_\varepsilon)$. Averaging this variance for N_0 different DVs and dividing by the variance of the time series (σ^2_x) we obtain Eq. (5.4) which is clearly equivalent to Eq. (5.3). Notice that the plot of this normalized variance $\sigma^{*2}(\varepsilon)$ as a function of the standardized distance is the DVV plot.

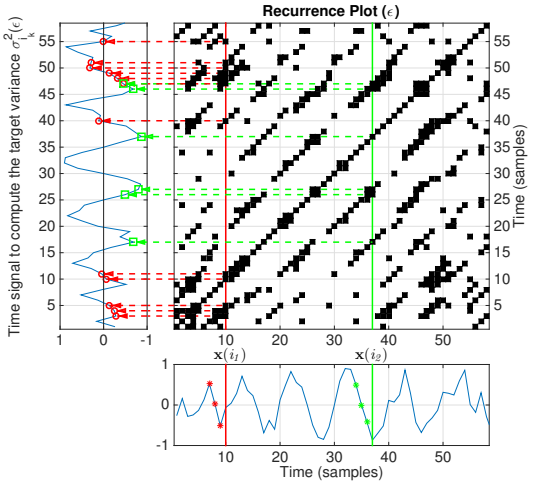

Figure 5.10. Example of how to find, using the RP(ε), the nearest DVs and the normalized variance of its targets.

$$\sigma^{*2}(\varepsilon) = \frac{\frac{1}{N_0}\sum_{i=1}^{N_0}\sigma^2_{i_0}(\varepsilon)}{\sigma^2_x} \tag{5.4}$$

The analysis of targets variance according to a distance r_d, in the DVV algorithm, or a distance ε, in the RP, is an indicator of the recurrence behaviour of the studied phase space. This is not the only way to quantify the number and duration of recurrences of a dynamical system presented by its phase space trajectory. A proper selection of a RQA measure may allow an equivalent analysis, less parameter dependent and with greater robustness.

RQA measures as discriminating statistics

The main purpose of the statistical test within the surrogate data method is being sensitive to any changes exclusively related to the null hypothesis under study. For that reason, it must be highlighted the need to understand the signal modality characteristic being studied, and its relationship with the applied surrogate data generation algorithm.

As discussed in Section 5.2, the hypothesis of non-linearity is linked to the presence of information on the phase spectrum. The randomization of the phase spectrum leads to significant changes in the structure of the signal. The surrogates of a non-linear signal (using the WiAAFT algorithm) despite preserving the probability distribution and the spectrum amplitude (and therefore, the autocorrelation function) of the original signal, have a new arrangement of closest points. The DVV algorithm detects these changes through the variance of the targets of the closest points. An equivalent measure of RQA susceptible to the distribution of the closest points is the Trapping Time (TT), a statistic linked to the length of the vertical lines. The TT is related with the laminarity of the dynamical system, i.e. how long the system remains in a specific state. The study of TT parameter as a function of the recurrence threshold ε allows to study the evolution of recurrent states with increasing percentage of nearby points. In the case of linear signals, the statistic computed for the surrogate data will coincide with the vector TT (ε) of the original signal. Otherwise, the difference between statistics allows the identification of non-linear signals.

A similar argument can be given regarding the hypothesis of complexity using the PPTS algorithm (Section 5.2.2). Jumping among twin-points when generating the surrogates, break the diagonals when the signals deviate from a quasi-periodic oscillation. This produces surrogates with different diagonal line length in the RP for temporal series having high complexity while maintaining approximately the same diagonal line length in quasi-

periodic ones. An equivalent measure of RQA susceptible to the diagonal line length distribution is the average diagonal line length (L_d), or any other parameter related to the diagonal line length (see Table 2.2). The study of L_d as a function of the recurrence threshold ε and the comparison with that of its surrogates allows the identification of complexity.

Note that in both analysis, the compared statistics (original signal and surrogates) need to be computed having the same percentage of black points in the RP matrix. In this work a swept between the 10 % and the 80 % of the black points has been done. This new proposed representation (from now on called DVRQA, Delay Vector Recurrence Quantification Analysis) avoids the problem of choosing the most appropriate threshold for computing the RP in an unknown situation. Among the advantages of statistical analysis based on RQA it must be highlighted that it uses the entire signal, unlike the aforementioned techniques that only take into account some randomly chosen points. This supposed to be a more robust technique, less parameter dependent and with smaller resultant confidence intervals. On the other hand, the use of any estimator is avoided, such as the variance which needs a high minimum number of points for correct estimation.

The modality tests done in this work will compare different kind of Recurrence Quantification metrics computed for the original signal to those obtained for an ensemble of surrogates. If the metric of the original signal is significantly different from those of the surrogate, the null hypothesis is rejected. Since the analytical form of the probability distribution of the applied metric is not known, a non-parametric rank-based test is used [102]. In this work, for every original time series, we generate $N_s = 99$ surrogates. The metric for the original signal, t_o, and for the surrogates, $t_{s,i} (i = 1, \ldots, N_s)$, are computed and the series $\{t_o, t_{s,i}\}$ is sorted in increasing order, after which the position index (rank) r of t_o is determined. A right-tailed test is rejected if rank r of the original time series exceed 90.

The metric used in the analysis is the same as in the original DVV algorithm but substituting the variance estimator for each of the applied RQA parameters, ξ, in each case:

$$t_{TEST} = \sqrt{\left\langle \left(\xi^2(\epsilon) - \frac{\sum_{i=1}^{N_s} \xi_{s,i}^2(\epsilon)}{N_s} \right) \right\rangle_\epsilon} \tag{5.5}$$

where $\xi^2(\epsilon)$ is the corresponding RQA metric at recurrence threshold ϵ for the original signal, $\xi_{s,i}^2(\epsilon)$ is the corresponding RQA metric at recurrence threshold ϵ for the $i-th$ surrogate, and the average is taken over all the threshold vector. In this way, a single test statistic is obtained, and the aforementioned right-tailed surrogate testing can be performed.

5.4 Applications

This section presents some results of signal modality characterization for the detection of non-linearities and complexity both using the surrogate data generation algorithms presented in Section 5.2 and the test statistics based on RQA measures presented in Section 5.3.

5.4.1 Non-linearity characterization

The linear and non-linear nature of time series is examined by performing the DVRQA analysis on both the original and 99 surrogates time series computed with the WiAAFT algorithm. The applied statistical measure was the parameter TT. In the following this technique is referred as DVRQA/TT. To verify the proposed technique a number of time series with different linear and non-linear natures, deterministic and stochastic are generated. Each of the generated signals consists of 1024 samples. The first set corresponds to deterministic examples: sum of two sinusoidal signals (Eq. 2.16) and the quasiperidic signal (Eq. 5.2), and two non-linear, the Rössler signal (Eq. 2.14) and the Lorenz signal (Eq. 2.15). The second set correspond to four stochastic processes: two linear, Model I (Eq. 2.20) and Model III (Eq. 5.6), respectively, and two non-linear, Model II (Eq. 2.21) and Model IV (Eq. 5.7).

$$y[n] = 0.3 + 0.7 \cdot y[n-1] + v[n] + 0.4 \cdot v[n-1] \tag{5.6}$$

where $y[0] = 0$ and $v[n]$ is a standard normal distribution, $N(0,1)$.

$$y[n] = (\sqrt{1 + 0.5 \cdot y[n-1]}) \cdot v[n] \tag{5.7}$$

where $v[n]$ is a standard normal distribution, $N(0, 1)$. For each signal, the optimal embedding parameters have been determined using the RQA/TT technique studied in Section 2.4.

The results for the DVRQA analysis are illustrated in Fig. 5.11. For the sum of sinusoidal signals (Fig. 5.11(a)) and the quasiperiodic signal (5.11(b)), the computed TT vector for the original signal coincides with the results obtained for the surrogates, therefore, the linear null hypothesis cannot be rejected. Figures 5.11(c) and 5.11(d) correspond to the simulation of the Rössler and Lorenz signals, respectively. In those cases, the resulting TT values for the original signal significantly differ from the ones for the surrogates in both extremes of the graph. The resulting value of the rank-order test, r, is 100. For the stochastics Models I and III (Fig. 5.11(e) and 5.11(f)), the values of TT fall into the confidence interval defined by the surrogates. However, in the case of the non-linear Models II and IV (Fig. 5.11(g) and 5.11(h)), original and surrogate statistics are clearly different. Undoubtedly, the variable r is equal to 100 and the null-hypothesis related to linearity can be rejected.

Note that for the continuous deterministic time systems (panels a),b), c) and d)), the maximum value of the parameter TT is higher than the one computed for the stochastic signals (panels e), f),g) and h)). High values of TT appear for continuous time systems with a fine time resolution and with a not too small recurrence threshold ε [41, 37]. Analogously to the DVV algorithm, this technique detects the presence of non-linearities based on the comparison of the locality between the original data and the surrogates. Moreover, it is interesting to see that linear surrogates in the case of deterministic signals (panels c) and d)) present larger values of TT (which is closely related to its lower complexity), compare to the linear realization of the stochastic processes (panels g) and h)) which present shorter values of TT. It might be due to the broken underlying non-linear structures.

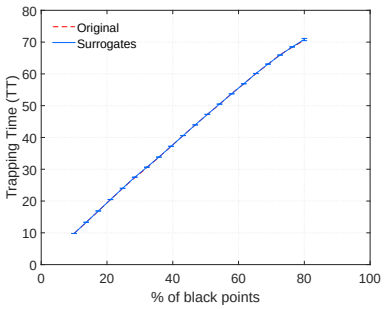

(a) Sinusoidal signal. r=51

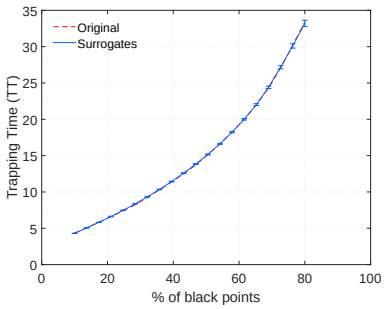

(b) Quasiperiodic signal. r=66

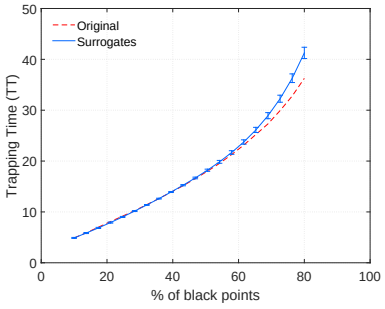

(c) Rossler signal. r=100

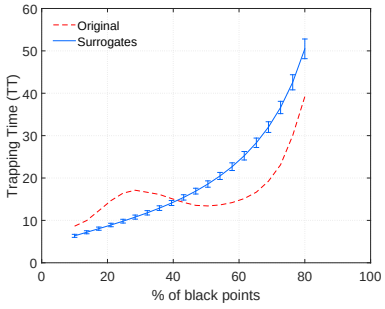

(d) Lorenz signal. r=100

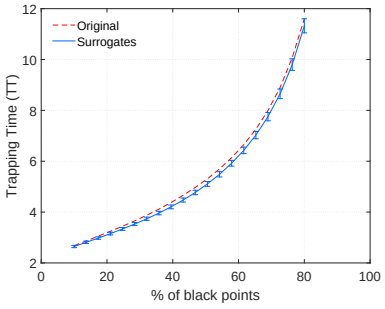

(e) Model I. r=72

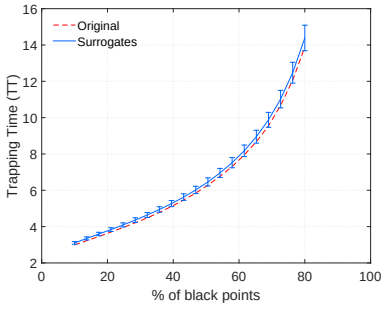

(f) Model II. r=55

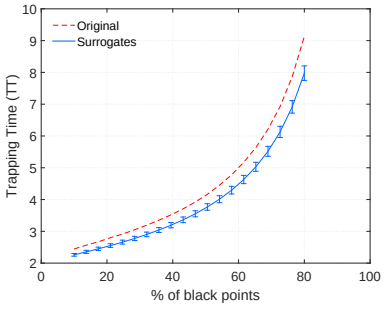

(g) Model II. r=100

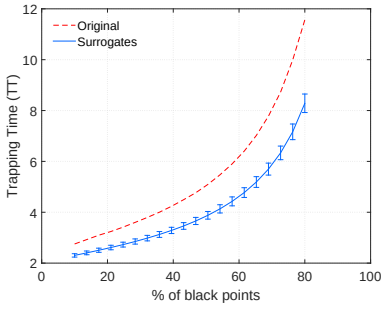

(h) Model IV. r=100

Figure 5.11. DVRQA/TT analysis with 99 WiAAFT surrogates performed on eight simulated time series using their corresponding embedding parameters.

Unfortunately we have not found any real application where applying the new propose algorithm, neither the DVV algorithm. Despite having worked on the problem of the non-stationarities of the real data, and the problem of the estimator related to the following sample, we cannot certainly claim that this blind approach may detect real linear/non-linear data. However, we have worked out the complexity characterisation by means of the new approach based on the PPTS surrogate data generation algorithm and the DVRQA method.

5.4.2 Complexity characterization

Regarding the complexity characterization, we have focused on the bioacoustic problem of irregular animal vocalizations. Being able to detect these irregular vocalizations is an important thing since they may convey information about pathologies in the voice production organs. In order to demonstrate this idea we have employed a database from [103]. The database contains dysphonic sounds from animals, and was recorded in a clinic for small animals with a sample frequency of 22050 Hz.

We analysed a recording containing dog barking sounds with different Harmonic to Noise Ratio (HNR). This parameter can be used in animal bioacoustics to quantify dysphonia. Normal sounding dogs occupy a middle HNR range, while dysphonic dogs exceed this range to higher as well as to lower HNR values [104, 105]. Figure 5.12 shows the time representation of a fragment of the sound alongside with the phase space representation (only the first two components of the DVs). It is interesting to emphasize that the phase space representation of both the original and one of the surrogates, are quite similar; although in the time domain, the surrogate sequence seems to be more homogeneous (lower complexity).

Figure 5.13 shows the three different sounds with low, medium and high HNR. We have performed the DVRQA test using the average diagonal line length (L_d) as the discriminating statistic and using a limited number of samples (400 samples). The null hypothesis is that the signal can be obtained as the sum of sinusoids with incommensurate frequencies. The confidence interval was established comparing with 99 PPTSs. The results show that the medium and high HNR dog barks reject the null test evidencing non-linear deterministic chaos (rank-order test, r=90 and r=100 respectively). The DVRQA test cannot only be employed to detected but also to quantify in accordance with the HNR.

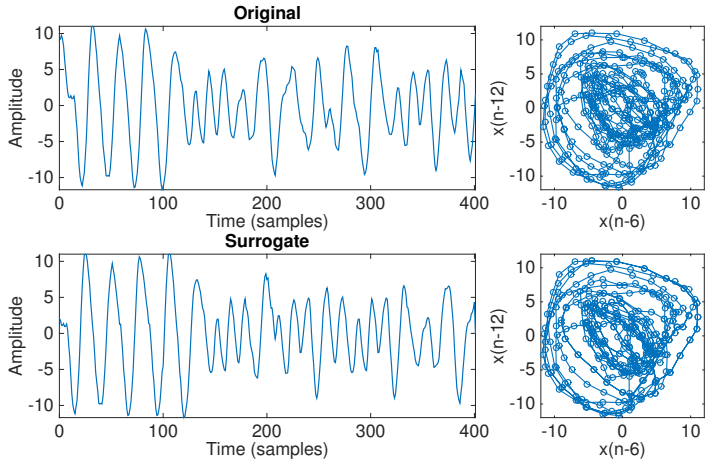

Figure 5.12. Up) Time representation of the medium HNR dog sound alongside with its phase space representation. Down) Time representation of one of the surrogates obtained with the PPTS alongside with its phase space representation.

5.5 Conclusions

In this chapter we have analysed the problem of using hypothesis testing for non-linear detection and characterization of complexity in temporal series from the RPs point of view. In order to do this we have focused on both, the generation of surrogates and the devising of statistical tests. Regarding the surrogate generation, we have worked with the WiAAFT algorithm, a technique which maintains the temporal structure of the original signal while at the same time provides enough degree of randomness to obtain valid surrogates for testing non-linearity (suitable for non-stationary signals). We have also raised a different kind of surrogates, the PPTS, that are valid for detecting non-linear determinism and complexity in short oscillating signals. In the devising of this new kind of surrogates the RPs play an important role in the definition of twin points and in the final understanding of the algorithm. We have also demonstrated that the RPs are a valid tool not only for the generation of surrogates, but also for the design of the statistical tests. This has been illustrated by reformulating the DVV method using RPs.

This analysis has led to the creation of new discriminating tests based on

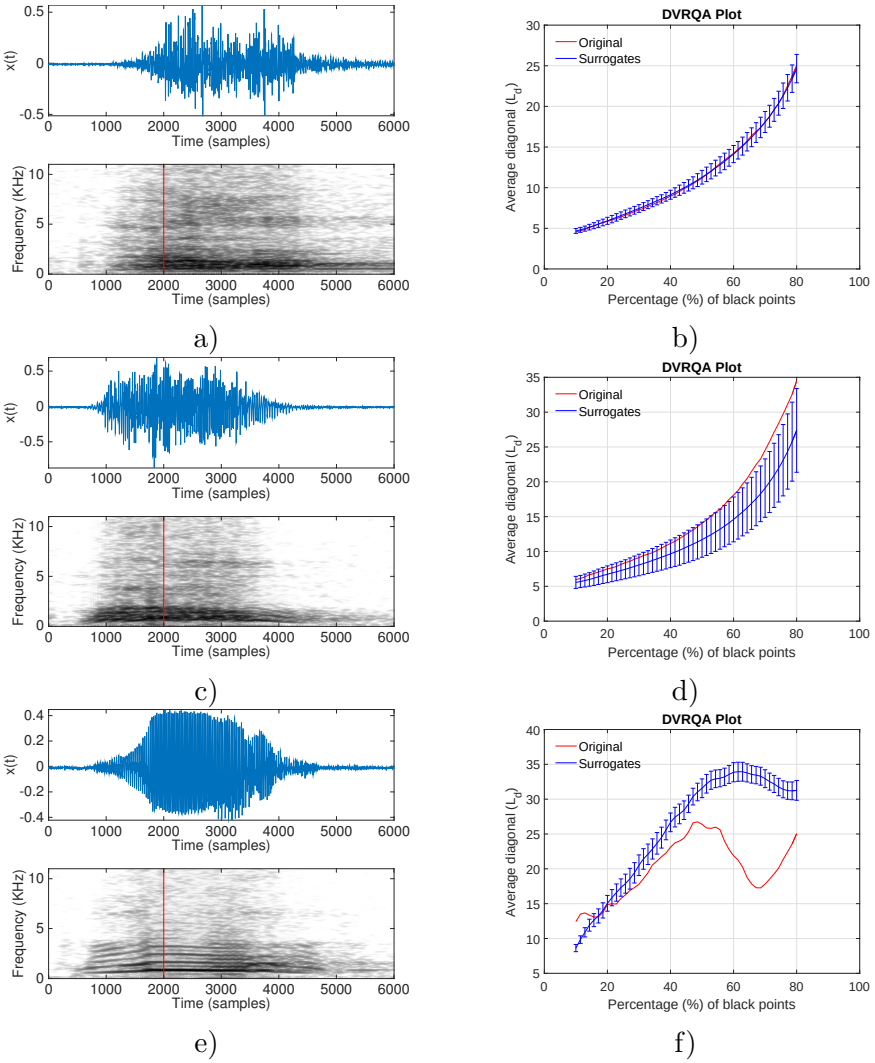

Figure 5.13. a) TFR of a low HNR dog bark, b) DVRQA analysis of the low HNR dog bark, c) TFR of a medium HNR dog bark, d) DVRQA analysis of the medium HNR dog bark, e) TFR of a high HNR dog bark, f) DVRQA analysis of the high HNR dog bark. The red vertical line indicates where the DVRQA analysis was performed (99 PPTS were used for the analysys).

RQA oriented to hypothesis testing, mainly non-linear and complexity detection. The proposed test (DVRQA) has the advantage of analysing the recurrent structures avoiding the problem of choosing the most appropriate recurrence threshold in an unknown situation. The selection of the RQA metrics has to be carefully chosen depending on the surrogates. The trapping time parameter captures significant differences in the recurrences, and therefore, it is appropriate for testing non-linearity with the WiAAFT algorithm. Whereas the PPTS has proven to be useful for testing complexity in short oscillating signals using the averaged diagonal line length.

We have demonstrated through simulations that we can detect non-linearities in signals of different nature (stochastic and deterministic) using the proposed algorithms. Moreover, we have analysed the problem of anomalies in voice production of mammals and the use of algorithms for their detection and characterization. The analysis of a database containing real-world sounds from dysphonic dogs, has shown that the L_d parameter, alongside with the PPTS, allows establishing relationships among the HNR, the complexity and the dysphonic dog barking sounds.

Non-linear Impact Acoustic Spectroscopy

6

Non-linear Impact Acoustic Spectroscopy 6

6.1 Introduction

The study of the vibration of engineered materials is obtaining high levels of interest from scientific communities due to the accuracy and facility of damage assessment [106, 107]. Concrete is an inhomogeneous material with a mesoscopic structure, multi-scaled, from nano- to millimetric sizes, where Hertzian contact between particles predominates. In this material, an anomalous resonance frequency shift appears (a change in the elastic constants) when excited by an external source.

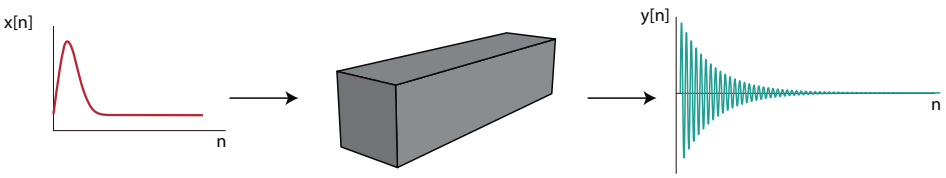

Figure 6.1. Schematic representation of a vibrational experiment, where the input $x[n]$ is an impact and the output $y[n]$ is the acceleration of the specimen proportional to its vibration.

Figure 6.1 shows an schematic representation of the experimental showing the input impact $x[n]$ and the output $y[n]$. This vibration is attenuated and finally stops, returning to its primary state, as the driving amplitude decreases and low strain values are reached [108]. The system varies its dynamical modulus, K, as a function of the input amplitude and the corresponding strain, therefore, it does not obey the linear systems property of homogeneity seen in Chapter 1.

The first studies in mesoscopic materials focusing on its dynamic behaviour were carried out for rocks and granular solids like sandstone and limestone, reporting non-linear and hysterectic responses, while trying to model this phenomenon with complex equations [109, 110]. Van Den Abeele et al. [111] presented a one-dimensional constitutive relation between the stress and strain in this new class of materials (Eq. 6.1):

$$K(\epsilon, \dot{\epsilon}) = K_0 \cdot [1 - \beta\epsilon - \delta\epsilon^2 + \alpha[\Delta\epsilon + \epsilon \cdot sign(\dot{\epsilon})]] \tag{6.1}$$

where K is the non-linear hysteretic modulus with K_0 denoting the linear modulus, β and δ the classical quadratic and cubic non-linear parameters, respectively, ϵ the strain, $\Delta\epsilon$ the strain amplitude in a cycle, $\dot{\epsilon}$ the strain rate, $sgn(\cdot)$ is the sign function and the parameter α is a measure proportional to the hysteresis of the material. Figure 6.2 shows a graphical representation of Equation 6.1. For low strain ratios, the hysteretic modulus equals the constant K_0 and the system under study behaves linearly. For higher strain ratios, the modulus varies proportional to the strain and the non-linear parameters β and δ. When the loading ($\dot{\epsilon} > 0$) and relaxing processes ($\dot{\epsilon} < 0$) do not follow the same path, the system shows a hysteretic behaviour proportional to parameter α (shadow area). Due to the proportionality between the resonance frequency of an element (f) and its elastic constants, the evolution of the non-linear hysteretic modulus of the system might be studied by mean of its resonance frequency.

In the last decade, several authors have successfully characterized the damage of materials by means of Nonlinear Elastic Wave Spectroscopy (NEWS) methods [112]. These experiments are based on the same phenomenological model and they can be categorized by the source of excitation (acoustic, ultrasonic or impact) and the number of signals injected into the system (one or several). The apparatus used in the different studies varies substantially, but the essence of the determination of the non-linear proper-

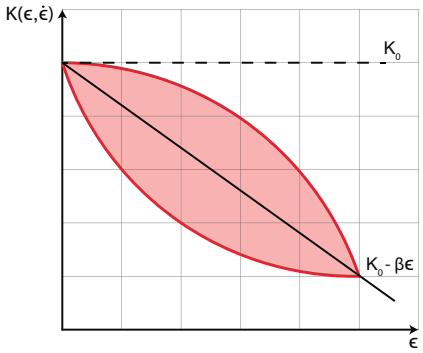

Figure 6.2. Graphical representation of hystretic modulus decribed by Equation 6.1.

ties remains the same in all cases. Some authors have used an acoustical source (electroacoustic transducer, mainly) in order to induce the element under examination into a steady state of reverberation. Some investigations have evaluated this behaviour by using several signals, involving the use of frequency sweeps around the principal mode of vibration of the element, at different input amplitudes (SIngle MOde Nonlinear Resonance Acoustic Spectroscopy, SIMONRAS [109, 113]; Nonlinear Wave Modulation Spectroscopy, NWMS [111]), and others have used one single signal and computed the attenuation of the material when the source of motion stops (Non-linear Resonance Spectroscopy, NRS[114]). The signals were recorded by accelerometers or laser vibrometers. In ultrasonic excitation, there has been used a piezoelectric transducer for signal transmission and another transducer or laser vibrometer as the receiver. In this case, frequency sweeps at different input voltages have been employed to induce the element into a steady state of vibration (SIngle MOde Nonlinear Resonance Ultrasonic Spectroscopy, SIMONRUS [111]; Nonlinear Resonance Ultrasonic Spectroscopy, NRUS [115, 116, 117, 118]). New research is focused in impact spectroscopy because of its low cost and the easy excitation of the elements under study. An impact hammer has been used to induce the vibration of the element and record the acceleration experienced by the specimen, by means of an accelerometer attached to its surface (Nonlinear Impact Resonance Acoustic Spectroscopy, NIRAS [119, 120, 121]; Nonlinear Single Impact Resonance Acoustic Spectroscopy, NSIRAS [122]; and Impact Nonlinear Reverberation Spectroscopy, INRS [123]). A summary

of NEWS methods is shown in Table 6.1.

Table 6.1. Summary of non-linear elastic wave spectroscopy (NEWS) methods according to the type of excitation source and the number of signals.

		NUMBER OF SIGNALS	
		>1	**1**
EXCITATION SOURCE	**ACOUSTIC WAVES**	SIMONRAS [109, 113], NWMS [111]	NRS [114]
	ULTRASONIC WAVES	NWMS [111], SIMONRUS [108], NRUS [115, 116, 117, 118]	-
	IMPACT	NIRAS [119, 120, 121]	NSIRAS [122], INRS [123]

As can be observed in the literature, the recent scientific research in NEWS techniques is focused on impact spectroscopy with one single signal, because of the obvious advantage in the testing time and probe conditioning. In the present chapter, a brand-new technique is developed, following the original methodology seen in NIRAS and inspired by a different signal processing procedure proposed by J. Eiras [122] and U. Dahlen [123]. The aim of this chapter is to obtain a valid technique completely equivalent to NIRAS but developed with one single impact, by means of the analysis of the signal processing procedure. This technique has been tested on the thermal damage assessment of specimens of Portland cement mortar.

The reminder of this chapter is organized as follows: In Section 6.2, mathematical background and signal processing issues of the different techniques are described. The materials, specimens, and test layout used to obtain the results of the present study are described in Section 6.3. The results obtained from the new technique and a comparison of the data obtained from the different impact resonance acoustic spectroscopic methods are found in Section 6.4. In Section 6.5 the conclusions of this study are presented.

6.2 Mathematical Background

Most of the usual threats to the durability of concrete result in distributed micro-cracking damage, which favours a hysteretic behaviour in the stress–strain relation. In typical resonance frequency tests, this hysteretic behaviour manifests itself as a downward shift of the resonance frequency with increasing amplitude of the excitation. Along with the frequency–amplitude dependence, the damping properties also become dependent on the amplitude. The origin of this behaviour appears to be in the rubbing between the interfaces of internal defects produced upon mechanical wave propagation. Besides these effects, a considerable effort has to be made to understand the underlying physical phenomena to develop new non-destructive non-linear resonance spectroscopy based techniques.

A discrete reverberation signal, $y\,[n]$, may be studied as the product of an exponentially decaying function, $a\,[n]$, and an exponential time-varying phase signal, $s\,[n]$ [124, 114]. The instantaneous frequency exponentially varies from a minimum frequency f_{min} ($f[1] = f_{min}$) up to a maximum frequency f_{max} taken at the end of the sampling interval ($f[N] = f_{max}$), resulting:

$$f[n] = f_{min} + \Delta f \cdot (1 - e^{-\gamma n T_s}), n \in \{1, \ldots, N\} \tag{6.2}$$

where $\Delta f = \frac{f_{max} - f_{min}}{1 - e^{-\gamma N T_s}}$ controls the exponential frequency swept. Therefore, a reverberation signal $y[n]$ may be modelled as:

$$\begin{aligned} y\,[n] =& a\,[n] \cdot s\,[n] \\ =& \overbrace{\left(a \cdot e^{-\gamma n T_s}\right)}^{a[n]} \cdot \overbrace{\left(sin\left(2\pi f_{max} n T_s - 2\pi \frac{\Delta f}{\gamma}\left(1 - e^{-\gamma n T_s}\right)\right)\right)}^{s[n]}, \\ & n \in \{1, \ldots, N\} \end{aligned} \tag{6.3}$$

where a denotes the amplitude and γ the attenuation, T_s is the sampling period (which is the inverse of the sampling frequency, i.e. $f_s = 1/T_s$), and N is the number of samples acquired in the sampling interval $N \cdot T_s$. The resulting signal is an exponentially decaying sine function with a

time-varying phase, which simulates the upward resonance frequency shift observed during the analysis of resonance frequency tests. The shifts in both the resonance frequency and in the attenuation properties due to non-linear effects are then studied in the frequency domain by applying the discrete-time, discrete-frequency Fourier Transform (DFT) with N_{DFT} equally spaced points:

$$\begin{aligned} Y[f] =& T_s \cdot DFT\{y[n]\} = T_s \cdot \sum_{n=0}^{N_{DFT}-1} y[n] \cdot e^{-j2\pi f n T_s}, \\ f \in& [0, 1 \cdot f_s/N_{DFT}, ..., (N_{DFT}/2-1) \cdot f_s/N_{DFT}] \simeq [0, f_s/2] \end{aligned} \tag{6.4}$$

Note that the DFT has been expressed in terms of the analog frequency (f) to ease the understanding of the variables involved in the technique, regardless of the digital acquisition process. Two corrections have been made to the expression: the discrete frequency samples have been expressed in terms of the analog frequency, and the amplitude spectrum has been weighted by T_s. The number of points over which the Fourier transform is computed, N_{DFT}, is always larger than the number of time samples, N, to improve the frequency visualization (zero padding). In order to avoid discrepancies between different sampling frequencies f_s, the graphical resolution in the frequency domain (f_s/N_{DFT}) is kept equal to 0.25.

Due to the characteristic damped non-linear reverberation signal, wherein both the frequency and the damping change as a function of time and amplitude, both these factors will influence the width and the amplitude of the resulting resonance spectral peak. Mathematically, the influence of these factors is explained by substituting Equation 6.3 in Equation 6.4 and applying the convolution theorem. This results in the following equation.

$$\begin{aligned} Y[f] =& T_s \cdot \sum_{n=0}^{N_{DFT}-1} \left(a \cdot e^{-\gamma T_s n} \cdot sin\left(2\pi f_{max} n T_s - 2\pi \frac{\Delta f}{\gamma} \left(1 - e^{-\gamma n T_s} \right) \right) \right) \cdot e^{-j2\pi f n T_s} \\ =& T_s \cdot \left(DFT\{a \cdot e^{-\gamma n T_s}\} * DFT\left\{ sin\left(2\pi f_{max} n T_s - 2\pi \frac{\Delta f}{\gamma} \left(1 - e^{-\gamma n T_s} \right) \right) \cdot e^{-\gamma n T_s} \right\} \right) \\ =& T_s \cdot (A[f] * S[f]), \qquad f \in [0, f_s/2] \end{aligned} \tag{6.5}$$

Here, $A[f]$ is the Fourier transform of the exponentially decaying signal,

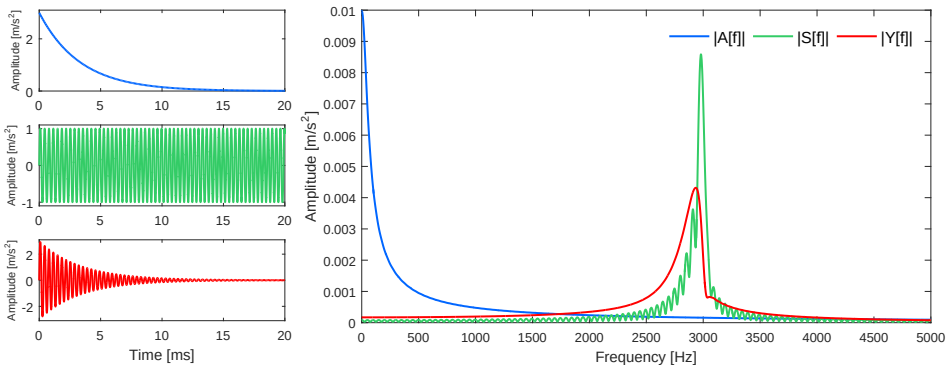

Figure 6.3. The left part of the panel represents the temporal aspect of the three involved signals, and the right part represents the three amplitude spectra. The blue lines are related to the exponential decay signal with $\gamma = 300$ and $a = 3$. The green line represents the time-varying phase sinusoidal function with $f_{min} = 2.8$ kHz, $\Delta f = 200$ Hz, $f_{max} = 3$ kHz, $f_s = 500$ kHz, $N = 10000$. The red line represents the resulting reverberation signal.

$a[n]$, and $S[f]$ is the Fourier transform of the time-varying phase sinusoidal function, $s[n]$. The Fourier transform of the resulting signal, $Y[f]$, can be seen as a weighted average of the frequency and amplitude content of both of the previous signals, resulting from the convolution.

An example is shown in Figure 6.3 with the following parameters: $a = 3$, $\gamma = 300$, $f_{min} = 2.8$ kHz, $\Delta f = 200$ Hz, $f_{max} = 3$ kHz, $f_s = 500$ kHz, $N = 10000$. The left part of the panel represents the temporal aspect of the three involved signals, and the right part represents the three amplitude spectra. The product of any two time signals is equivalent to a convolution in the frequency domain, where the maximum amplitude of the reverberation signal, $Y[f]$, corresponds to the minimum frequency of the chirp signal involved (2.8 kHz), and the peak width of the reverberation signal, $Y[f]$, is proportional not only to the bandwidth of the spectrum of the decreasing exponential signal (proportional to the attenuation γ) but also to the frequency width of the chirp signal.

Traditional non-linear resonance tests are based on the investigation of the damping variations and the shift of the resonance frequency by excitations of increasing amplitude. These effects can also be studied as results of

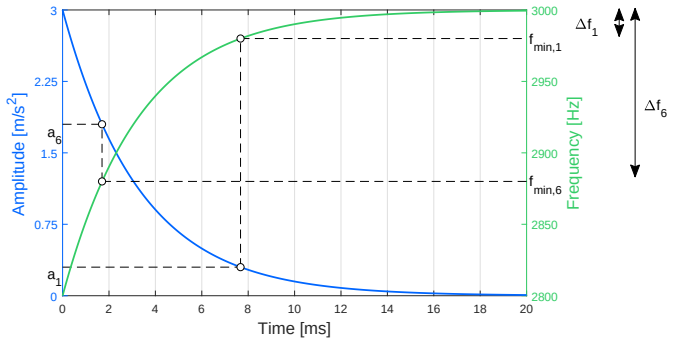

Figure 6.4. Temporal evolution of the instantaneous amplitude, $a[n]$ (blue line), and the instantaneous frequency, $f[n]$ (green line), according to Eq. 6.3 and Eq. 6.2, respectively. The parameters are with $a = 3$, $\gamma = 300$, $f_{min} = 2.8$ kHz, $\Delta f = 200$ Hz, $f_{max} = 3$ kHz, $f_s = 500$ kHz and $N = 10000$.

increasing the frequency range of the underlying time-varying phase signal: a widening of the chirp spectrum as the impact energy increases. The different reverberation signals of a resonance test are denoted by $y_i(n)$, with i the impact number and proportional to the strength (in this study, $i \in [1, 10]$). According to Equation 6.3, both the instantaneous frequency, $f\,[n]$ (Eq. 6.2), and the amplitude envelope of a reverberation signal, $a\,[n]$ (Eq. 6.3) vary according to the attenuation γ.

The attenuation γ not only controls the system instantaneous amplitude but also the frequency ranging from f_{min} to f_{max} (see Fig. 6.4). In the practice for different levels of impact, it has been checked that the attenuation γ does not change, it only varies the maximum amplitude a; and its corresponding minimum frequency f_{min} following Figure 6.4. So that, the reverberation signals acquired in a traditional resonance test at different impact levels, i, may be mathematically modelled as follows:

$$y_i\,[n] = a_i \cdot e^{-\gamma n T_s} \cdot sin\left(2\pi f_{max} n T_s - 2\pi \frac{\Delta f_i}{\gamma}\left(1 - e^{-\gamma n T_s}\right)\right),$$

$$n \in \{1, \ldots, N\} \tag{6.6}$$

$$a_i = i \cdot a \tag{6.7}$$

$$\Delta f_i = \frac{f_{max} - f_{min,i}}{1 - e^{-\gamma N T_s}} \tag{6.8}$$

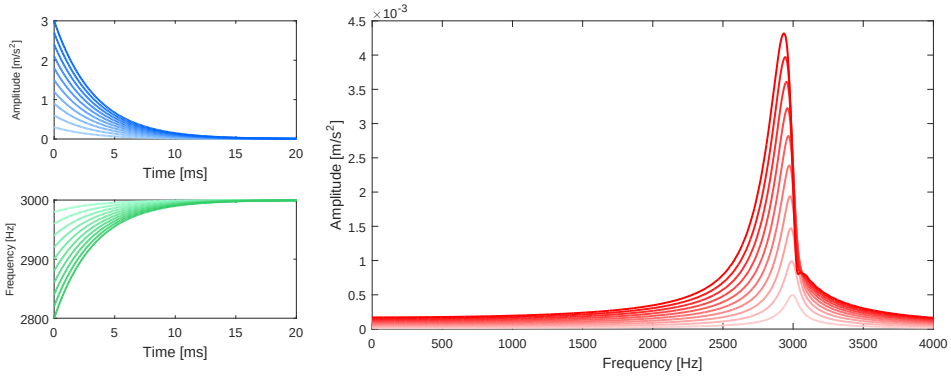

Figure 6.5. The left part of the panel represents the temporal evolution of the envelope amplitude $a_i[n]$ (blue lines) and its corresponding instantaneous frequency $f_i[n]$ with $i \in [1, 10]$ (green lines). In the right part of the panel, the different amplitude Fourier transform of the resulting simulated signals, $Y_i[f]$, are plotted in red. The color legend varies from light to dark colors as the level of impact increases. The parameters of the model are $a = 3$, $\gamma = 300$, $f_{min} = 2.8$ kHz, $\Delta f = 200$ Hz, $f_{max} = 3$ kHz, $f_s = 500$ kHz, $N = 10000$.

where a is the lowest impact amplitude, and $f_{min,i}$ is the corresponding minimum frequency according to the attenuation γ, the amplitude a_i and the relations marked in Figure 6.4. The reference amplitude and frequency functions correspond to the aforemention simulated experimental described in Figure 6.3, which corresponds to the strongest impact in a simulated resonance test. From these strogest impact curves, it is possible to determine the frequency variation for lower impacts: the corresponding first impact would have an amplitude a_1 equals to 0.3 and a $f_{min,1}$ equals to 2980 Hz. The corresponding sixth impact would have an amplitude a_6 equals to 1.8 and a initial minimum frequency $f_{min,6}$ equals to 2880 Hz. Figure 6.5 presents the temporal evolution of the envelope amplitude $a_i[n]$ with $i \in [1, 10]$ and its corresponding instantaneous frequency $f_i[n]$. In the right part of the panel, the different amplitude Fourier transform of the resulting simulated signals, $Y_i[f]$, are plotted. The color legend varies from light to dark colors as the level of impact increases. This model will be used in Section 6.2.4 to evaluate the different signal processing algorithms.

6.2.1 NIRAS

The technique of Non-linear Impact Resonance Acoustic Spectroscopy (NIRAS) relies on an impulse excitation of the specimen repeated with different impact strengths. The hysteresis parameter related to the resonance frequency shift α_f^{NIRAS} is obtained from a linear fit of the obtained peak amplitude spectrum A_i (Eq. 6.9) versus the peak normalized frequency $\tilde{f}_i$ (Eq. 6.10) of one mode from the multiple impacts at different strengths (Eq. 6.11).

$$A_i = max\{|Y_i[f]|\} \tag{6.9}$$

$$\tilde{f}_i = max_f\{|Y_i[f]|\} \tag{6.10}$$

$$\frac{\tilde{f}_0 - \tilde{f}_i}{\tilde{f}_0} = \alpha_f^{NIRAS} \cdot A_i \tag{6.11}$$

Here, $\tilde{f}_0$ is the resonance frequency obtained in the linear strain regime. The shift of the damping properties also exhibits a linear relation between the damping factor Q_i (Eq. 6.12) and the amplitude A_i (Eq. 6.9) following Eq. 6.13 [113]:

$$Q_i = \frac{\tilde{f}_i}{\tilde{f}_{i,2} - \tilde{f}_{i,1}} \tag{6.12}$$

$$\frac{1}{Q_i} - \frac{1}{Q_0} = \alpha_Q^{NIRAS} \cdot A_i \tag{6.13}$$

where $\tilde{f}_i$ is the resonance frequency of vibrations (Eq. 6.10), $\tilde{f}_{i,1}$ and $\tilde{f}_{i,2}$ are those frequencies on either side of the resonance at which the amplitude is $1/\sqrt{2}$ times the amplitude at resonance, and Q_0 is the linear regime damping factor. For low excitation amplitudes, the frequency shift $(\tilde{f}_0 - f_{min})$ is non-existent and the peak frequency and quality factor are considered to be obtained in the linear strain regime. In this study, $\tilde{f}_0$ and Q_0 are determined as the intersection with the y-axis of the linear relations between the peak amplitudes A_i and the peak frequencies $\tilde{f}_i$, and the peak amplitudes A_i and the measured damping factors Q_i, respectively [125]. One expects to find an increase in the both parameters proportional to the hysteresis, α_f^{NIRAS} and α_Q^{NIRAS}, with increasing damage of the specimen.

6.2.2 NSIRAS

A single-impact based version of the NIRAS technique was recently introduced by Eiras et al. [122]. In the so-called NSIRAS technique (Non-linear Single Impact Acoustic Spectroscopy), the reverberation from a standard impact resonance frequency test is analysed using a short time Fourier Transform (STFT), and the non-linear frequency shift as a function of the amplitude can be successfully determined over a dynamic range. The method consists of a sliding window with fixed length L, $w^L(n)$, that moves in $S-$sample steps through a single reverberation signal, $y_I(n)$, and transforms the time segment within the $p-$window, $y_{I,w_p^L}(n)$, to the frequency domain at every temporal window position (Eq. 6.14).

$$\begin{aligned} y_{I,w_p^L}(n) =& y_I(n) \cdot w^L\left(n - p \cdot S\right), n \in \{1, \ldots, N\}, \\ & p \in \left\{0, \ldots, \left\lfloor \frac{N-L}{S} \right\rfloor \right\} \end{aligned} \tag{6.14}$$

The original study was done with a Tukey window, however, the mathematical formulation of this work has been done for any kind of window $w^L(n)$. In this study, a traditional rectangular window has been used (Eq. 6.15). The window length has been chosen to ensure that at least 10 periods in the fundamental ringdown signal are captured, the window shift (S) is 30% of the window length, or a 70% overlap between consecutive windows.

$$w^L(n) = \begin{cases} 1, & 1 \leq n \leq L \\ 0, & otherwise \end{cases} \tag{6.15}$$

Figure 6.6 shows a schematic representation of the algorithm. The moving window analysis is stopped when the spectral amplitude falls below a preset threshold value (th), e.g. 5% of the maximum spectral amplitude measured in the first time window. Figure 6.6(b) represents the frequency domain at every window position. It can be seen that the shape of the resulting amplitude spectra seem similar to the spectrum of a burst signal, and not as much to that of the reverberation signal seen in Figure 6.3 (red line). This windowing breaks the underlying effect of the exponentially decaying signal and the effects are reflected in the estimation of the non-linear parameters α_f^{NSIRAS} and α_Q^{NSIRAS}. Both are estimated following the linear fit seen

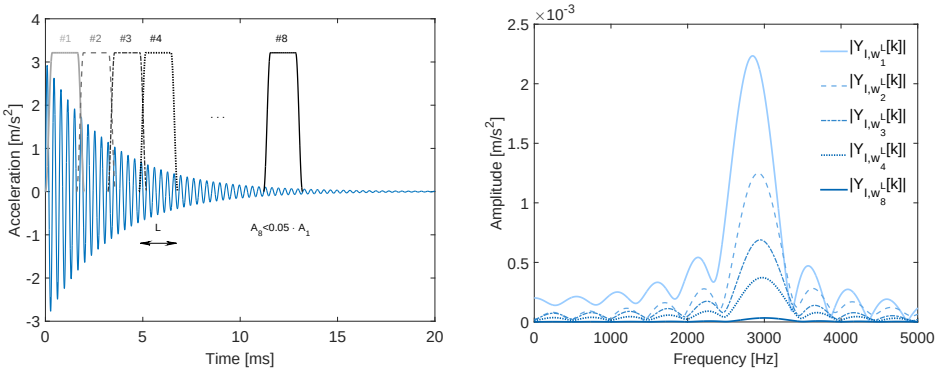

(a) (b)

Figure 6.6. NSIRAS. a) Schematic representation of the signal processing algorithm to obtain the time-varying resonance frequency shift through the NSIRAS algorithm. b) Stacked frequency spectrum representation of the time signals within the first 8 windows.

earlier; they are reformulated using the current variables according to the NSIRAS technique in Eqs 6.16, 6.17, 6.18, 6.19, and 6.20:

$$A_{I,p} = max\{|Y_{I,w_p^L}[f]|\} \tag{6.16}$$

$$\tilde{f}_{I,p} = max_f\{|Y_{I,w_p^L}[f]|\} \tag{6.17}$$

$$\frac{\tilde{f}_{I,0} - \tilde{f}_{I,p}}{\tilde{f}_{I,0}} = \alpha_{f,I}^{NSIRAS} \cdot A_{I,p} \tag{6.18}$$

$$Q_{I,p} = \frac{\tilde{f}_{I,p}}{\tilde{f}_{I,p,2} - \tilde{f}_{I,p,1}} \tag{6.19}$$

$$\frac{1}{Q_{I,p}} - \frac{1}{Q_{I,0}} = \alpha_{Q,I}^{NSIRAS} \cdot A_{I,p} \tag{6.20}$$

where $\tilde{f}_{I,0}$ and $Q_{I,0}$ are the linear approximations for the linear regime resonance frequency and the damping factor, respectively, related to the reverberation signal $y_I(n)$.

6.2.3 FANSIRAS

The proposed technique, called Flipped Accumulative Non-Linear Single Impact Resonance Acoustic Spectroscopy (FANSIRAS), is based on the NSIRAS technique but with a variable length window. As with the spectrogram-based technique, the proposed method only requires a single reverberation signal $y_I(n)$ to obtain a reliable estimate of the non-linearity. The acronym of the technique corresponds to the original idea of the algorithm, based on the equivalent reconstruction of the signals of the NIRAS technique but from a single signal: flipping the signal and windowing cumulatively. In order to ease the mathematical nomenclature, the method is described as a window of initial length equal to that of the acquired signals, N, which progressively decreases its length to the lower bound, and transforms the time segment of the impact signal within the pth window, $y_{I,w_p^{L_p}}(n)$, to the frequency domain at each window position as follows:

$$\begin{aligned} y_{I,w_p^{L_p}}(n) =& y_I(n) \cdot w^{L_p}\left(n - p \cdot M\right), \qquad n \in \{1, \ldots, N\}, \\ & p \in \left\{0, \ldots, \left\lfloor \frac{N}{M} \right\rfloor - 1\right\} \end{aligned} \tag{6.21}$$

Here, $w^{L_p}(n)$ represents the rectangular window, which shortens at each step of the algorithm. It has the same expression as in Equation 6.15, but the length of the window varies at each position p, $L_p = N - p \cdot M$. M represents the number of samples by which the window decreases at each step of the algorithm, and it is equivalent to the parameter S of NSIRAS. It is related to the number of points used in the regression, but it does not significantly affect the estimation of the non-linear parameters. In this work, it is computed as the number of samples in 4 periods of the signal.

Figure 6.7(a) shows a schematic representation of the algorithm in the time domain. This algorithm preserves the phenomena underlying a reverberation signal, as can be seen in the resulting amplitude spectra (Fig. 6.7(b)). Obviously, the first signal's amplitude spectrum coincides with the original input signal, since the whole signal is analysed. As the time window shortens, the amplitude of the signals decrease and the resulting signals are equivalent to having excited the specimen with impacts of lesser strengths. As the strength of the impact decays, the peak amplitude decreases, and the resonance frequency increases. The damping factor also increases for

each time window, as will be seen in the following (Section 6.2.3).

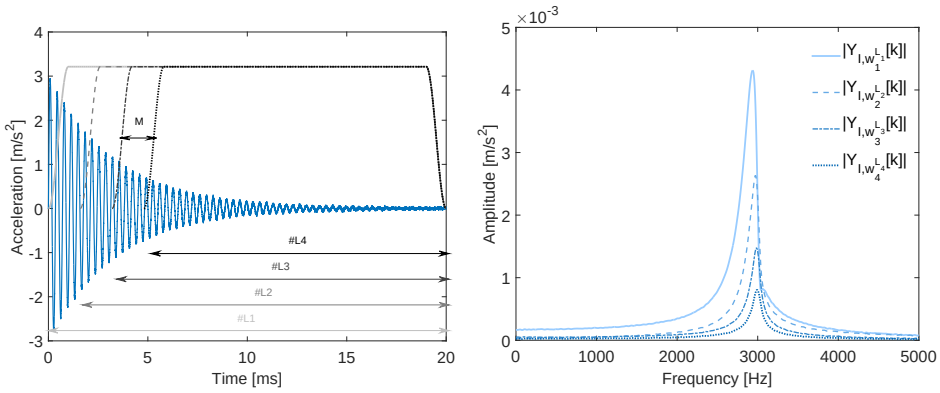

(a) (b)

Figure 6.7. FANSIRAS. a) Schematic representation of the signal processing algorithm to obtain the time-varying resonance frequency shift through the FANSIRAS algorithm. b) Stacked frequency spectrum representation of the time signals within the first 4 windows.

The non-linearity parameters $\alpha_{f,I}^{FANSIRAS}$ and $\alpha_{Q,I}^{FANSIRAS}$ are both estimated with the previous linear fits according to the NSIRAS technique in Eqs 6.16, 6.17, 6.18, 6.19, and 6.20, but splitting the time signal with the new windowing approach (Eq. 6.21).

Stop criterion

Apart from being a feature related to the hysteresis behaviour of the material, the damping factor $1/Q$ may reveal useful information for determining the final window in the FANSIRAS algorithm. The algorithm must stop before losing the signal information (too small window).

The progressive windowing done in the new proposed algorithm implies that the corresponding underlying chirp signal ranges from a larger minimum frequency up to the maximum linear frequency $\tilde{f}_0$. It supposes a lower bandwidth as $w^{L_p}(n)$ decreases its size. The mathematical expression of the damping factor controls the increasing of the peak frequency (which never stops growing) in the numerator split by the decreasing of the bandwidth as the window length decreases. What is used as the stop criterion is a

comparison of the current value of the damping factor with the previous one. The window in the FANSIRAS algorithm is decreased until the value of Q is lower than that obtained in the previous window.

Figure 6.8 represents an example of the amplitude spectrum obtained by the FANSIRAS algorithm applied to the simulated signal. The amplitude spectrum has been normalized in both axes: frequency, $(f - \tilde{f}_{I,p})$, and amplitude, $A/A_{I,p}$. The large size of the bandwidth of the largest window can be observed, which implies the lowest value of the quality factor. The decreasing window in the FANSIRAS algorithm is decreased until there occurs a value of Q lower than the previous window. In the example, the selected number of different time windows applied in the FANSIRAS algorithm would be 8.

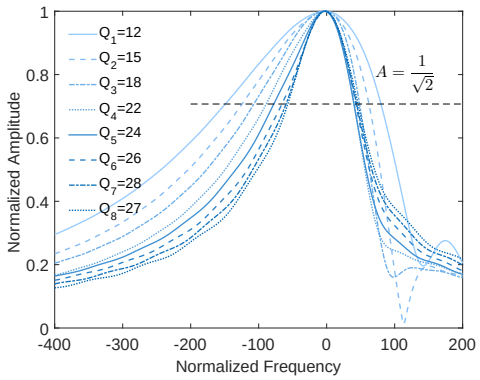

Figure 6.8. Stop criterion in the FANSIRAS algorithm. Example of the amplitude spectra obtained for consecutive windows by FANSIRAS algorithm applied to a real signal. The decreasing window is decreased until there occurs a value of Q lower than the previous window.

In the following, the non-linearity parameters for $NSIRAS$ are referred to as α_f^{NSIRAS} and α_Q^{NSIRAS}, and those for the FANSIRAS algorithm as $\alpha_f^{FANSIRAS}$ and $\alpha_Q^{FANSIRAS}$, taking into account that they are extracted from the largest impact reverberation signal in each experience.

6.2.4 Comparison

In order to fully understand the effects of the windowing on the estimation of the non-linear hysteretic parameters, the results of NIRAS, NSIRAS

and FANSIRAS algorithms applied on the simulation signal raised in Figure 6.3 are compared in Figure 6.9. The blue line represents the reference strongest original signal spectrum obtained from the simulated model seen in Figure 6.5; the NSIRAS and FANSIRAS results are obtained from it. The green lines represent the first 8 NSIRAS stacked spectra and the red lines represent the 8 first FANSIRAS spectra. This representation allows the comparison of how the resonant frequencies migrate with time and amplitude for the same measured signal depending on the applied algorithm. The short-time frequency transform (STFT) done in the NSIRAS algorithm results in a down-biased amplitude estimation. The STFT also avoids the weighted average of the whole frequency content available in the signal, allowing a ranging more widely over frequencies. The interval of frequencies ranges from a lower minimum resonance frequency, f_{min}, up to the same f_{max} than NIRAS. The new proposed FANSIRAS algorithm is able to extract equivalent amplitude spectra to the traditional NIRAS technique from a single signal. The decreasing cumulative window respects not only the decreasing exponential shape but also the frequency average along the whole ring-down.

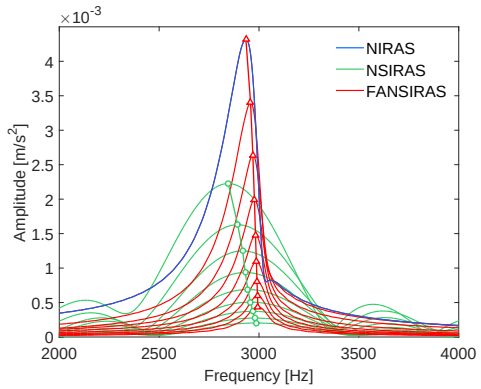

Figure 6.9. Comparison of the simulated signal amplitude spectrum computed by NSIRAS and FANSIRAS algorithms. The blue line represents the reference original simulated spectrum, the green lines represent the first 8 NSIRAS stacked spectra and the red lines represent the 8 first FANSIRAS spectra.

In Figure 6.10, the estimation of the hysteretic non-linear parameters α_f and α_Q for the simulated model and the three different techniques is graph-

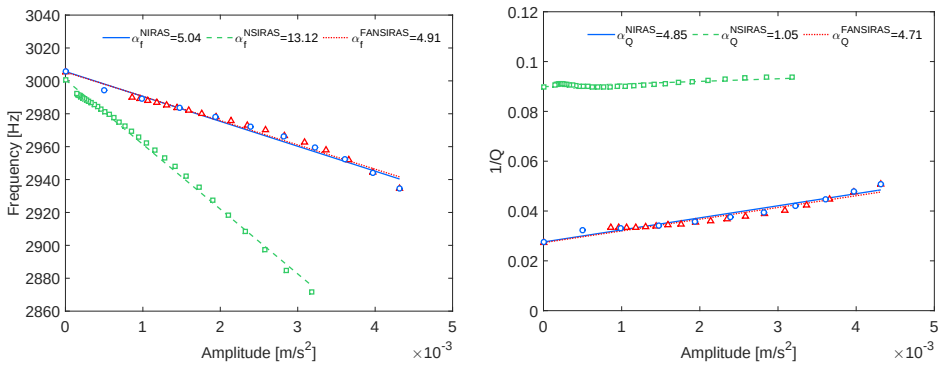

(a) (b)

Figure 6.10. Comparison of NSIRAS and FANSIRAS algorithms for a simulated signal. a) Amplitude dependent resonance frequency shift computation (α_f). b) Amplitude dependent resonance damping shift computation (α_Q). The y-axis interceptions represent the values of $\tilde{f}_0$ and Q_0 for each technique, respectively.

ically shown. The linear regime parameters $\tilde{f}_0$ and Q_0 are also marked. Remind that NIRAS algorithm is applied over the whole set of reverberation signals obtained from the mathematical model raised in Eqs 6.6, 6.7 and 6.8 (Fig. 6.5), however, NSIRAS and FANSIRAS are applied over the highest impact signal (Fig. 6.3). The parameters used in the NSIRAS algorithm were: window length equals to 10 periods of the signal, and a window shift equals to 30%. The window used in FANSIRAS algorithm progressively decreases 400 samples in each step. Due to the STFT, it can be noticed that NSIRAS varies in a bigger frequency range and a smaller amplitude interval. It results in a significantly higher value of slope α_f^{NSIRAS} than α_f^{NIRAS} for the same simulated model. The parameter $\alpha_f^{FANSIRAS}$ results equivalent to α_f^{NIRAS}. Therefore, the new windowing approach demonstrate a better estimation than the original single-based technique NSIRAS, at least, for the proposed numerical model.

As far as the authors' knowledge extends, the study of the variation of the amplitude-dependent damping had never been done before for the NSIRAS technique. It has been included in this study in order to show the importance of the kind of windowing when studying the quality factor of a rever-

beration signal. Figure 6.10(b) compares the results obtained by NIRAS and NSIRAS. At a glance, it can be observed that the α_Q^{NSIRAS} values are greater and less varying than α_Q^{NIRAS}. Although NSIRAS is able to estimate the shift of the peak frequency, the shape of the resulting time signals are almost equivalent to pure sinusoidal signals with an almost constant bandwidth bigger than in the NIRAS technique, proportional to the length of the window. Figure 6.10(b) also compares the variation of the damping factor obtained both from the NIRAS and FANSIRAS techniques. At a glance, it can be observed that FANSIRAS algorithm allows estimating the damping values equivalently to the NIRAS algorithm but from a single signal.

The shortening of the time signal from the lower bound, which is the base of the FANSIRAS technique, results on two different effects over the two involved signals. For the instantaneous amplitude, $a[n]$, it allows reducing the amplitude of the signal a but keeping constant the exponential decay factor γ. For the time-varying signal, $s[n]$, the decrease in the temporal window amounts to a narrower bandwidth (Δf). Therefore, the proposed numerical model (later verified with real experiments) shows that the variation of the damping factor Q with the amplitude is exclusively sensitive to changes on the bandwidth. There is not an amplitude-dependent attenuation. According to that, it must be noted that for the NIRAS and FANSIRAS algorithms applied over the theoretical model, the parameters of α_f and α_Q have resulted on similar numerical values. Despite having been computed by different procedures they are sensitive to the same effect: the widening of the underlying exponential phase-varying signal as the amplitude increases. In further sections, both hysteretic parameters for the three raised techniques are compared for a real dataset.

6.3 Experimental

6.3.1 Materials and specimens

Three mixes of standardized Portland cement mortar (water/cement = 0.5) made of 450 grams of Spanish cement CEM I-52.5-R (supplied by Cementval, Puerto de Sagunto, Spain), 1350 grams of 0/2 crushed quartz normalized sand and 225 grams of water were carried out in order to obtain nine 40x30x160 mm^3 specimens to perform the present study. This

geometry was chosen with the intention of avoiding two fundamental flexural modes in close frequencies coming from imperfections in the mixing and manufacturing process. Having a square cross section stimulates modal coupling between two resonance modes with similar frequencies, resulting in peak splitting in the spectra, and consequently, a decrease of accuracy in the frequency analysis. After the mixing process, filled iron moulds were stored in a wet chamber (20°C and 100% H.R.) for 24 hours, then the nine mortar pieces were released and stored in the wet chamber again for 60 days in order to reach the stabilization stage of elastic properties. Afterwards, the specimens were dried to constant mass in an oven at 40°C for 7 days and wrapped with plastic film until they reached room temperature again. These prismatic specimens were characterized by resonance impact acoustic spectroscopy, in order to determine their properties in the pristine state (TH40). Two thermal damage treatments were performed according to the chemical decomposition of Portland cement hydrates. First, the pristine specimens were thermally damaged at 400°C, achieving the decomposition of the calcium silicate hydrates (C-S-H) and calcium aluminate (C-A-H) and sulphoaluminate (Ettringite, monosulphate) hydrates, reaching this temperature in two hours, maintaining it for three hours, and slowly cooling for twelve hours inside the oven (TH400). Once room temperature was reached, the mortar bars were tested again by impact resonance acoustic spectroscopy. Second, the 400°C-treated specimens were thermally damaged at 525°C (this favours the $Ca(OH)_2$ decomposition) following the same heating–cooling procedure as explained above (TH525). This way, the same 9 specimens had been characterised for the three different treatments: TH40, TH400 and TH525.

6.3.2 Test layout

Acoustic resonance tests were performed with the elements as shown in Figure 6.11. An impact hammer (Brüel & Kjær 8206-003) was attached to an axis, located in a metallic structure. This axis, supported on two ball bearings, yields a free rotational motion in one plane with minimum friction. The specimen was placed on the metallic supports, slightly sloping, positioned for impact in the centre of the face and perpendicular to the axis of greater inertia of its cross section. In the opposite top-left corner, a piezoelectric accelerometer sensor (PCB 352A21, 0.956 $mV/m/s^2$ sensitivity) was attached in order to obtain the vibrational motion of the test

probe. The electric signal of the instrumented hammer and the accelerometer go through a signal conditioner (PCB 482A18), so as to be polarized and then transmitted to the oscilloscope (Tektronics MDO3014). The oscilloscope was configured to optimize the signal acquisition and processing with f_s equal to 250 kHz, N equal to 10000 samples, trigger voltage equal to 120 mV, and pre-trigger time equal to 4 ms. Finally, the information was transmitted via USB to a computer with a control software code developed by the authors. Taking advantage of the potential offered by the Instrument Control Toolbox of the MATLAB software package, a graphical user interface was developed, for the automation of the technique and to optimize it with respect to the test procedure requirements.

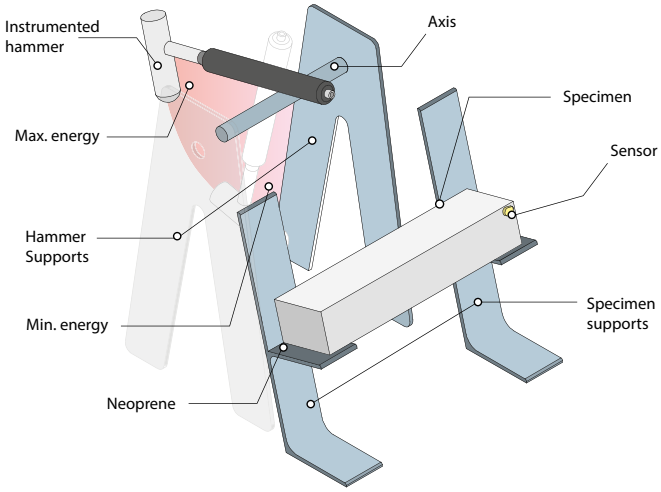

Figure 6.11. Experimental layout of the support hammer, disposition of the specimen, and location of the sensor.

6.3.3 Reproducibility test

In order to assess the robustness of the techniques, a reproducibility test of the non-linear resonance technique was performed (10 impacts of different energies were applied), making 5 repetitions in the same specimen in the bottom-up (starting with the lowest impact) configuration and the up-down (starting with the highest impact) configuration. The purpose of testing two different configurations is to make sure the discrete memory of the material does not affect the calculation of the non-linearity parameters [108,

126]. For this reason, there was a 24 hour space of time between the tests in the bottom-up configuration and those in the up-down configuration. In Figure 6.12(a) there can be seen the maximum intensity in the impact curve described by the instrumented hammer. In this graph, the repeatability of the impact energy can be seen since the 5 repetitions are in the same range and magnitude for all impact levels and both configurations. Figure 6.12(b) shows the peak amplitude spectrum versus peak frequency plot for the 5 tests made in each configuration. A very significant difference between the correlation from the first test in the bottom-up series and the rest of the correlations can be appreciated. This behaviour matches some experiments previously reported, when a specimen of mesoscopic material is conditioned with an external source of motion and it takes several hours to recover the mechanical properties of its initial state [110, 127]. Hence, the authors decided undertaking the experiment in the up-down configuration to ensure the reproducibility of the test and perform a proper comparison of the different procedures for assessing the non-linearity parameters.

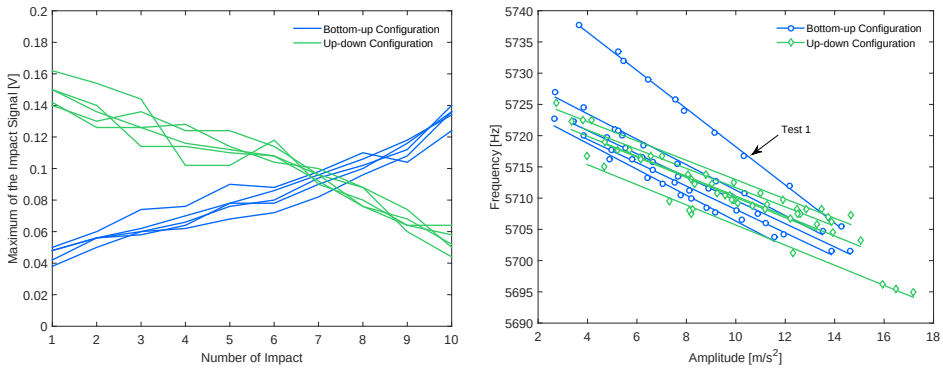

(a) (b)

Figure 6.12. Reproducibility Test. Five repetitions of the resonance test (10 different amplitude impacts) in the same specimen in bottom-up (starting with the lowest impact) configuration (blue) and up-down (starting with the highest impact) configuration (green) were carried out. 6.12(a) Maximum amplitude of the impact signal. 6.12(b) Relation between the spectral peak amplitude and the resonance frequency. The markers represent the experimental results and the straight lines represent the best fitted linear model for each test.

6.4 Results and Discussion

Figure 6.13 shows representative resonance spectra obtained at different impact energies for one mortar sample at the different damage treatments. It is important to notice how these real spectra fit to the model showed in Section 6.2. In the first instance, the TH40 specimens exhibited good performance due to the fact that the evaporated water inside the porous structure of the material had no influence on the material's mechanical properties. The second thermal treatment, the TH400 series, forced the evaporation of part of the water combined in the S-C-H, sulphoaluminates, and the A-C-H of the hydrated Portland cement, yielding a loss of stiffening and increasing the non-linearity of the system. Lastly, the TH525 series were severely damaged, greatly increasing the non-linearity and losing mechanical performance. The described damage produced by high temperatures resulted in 4 effects that can be distinguished in the spectra presented here: a progressive decrease of the resonance frequency, an increase of signal bandwidth, a downward shift of the resonance frequency with increasing impact energy, and the resonance peak became noticeably asymmetric. Although the impact energy was the same for all series and specimens, the maximum intensity reached in the spectra decreased as the damage in the specimens increased.

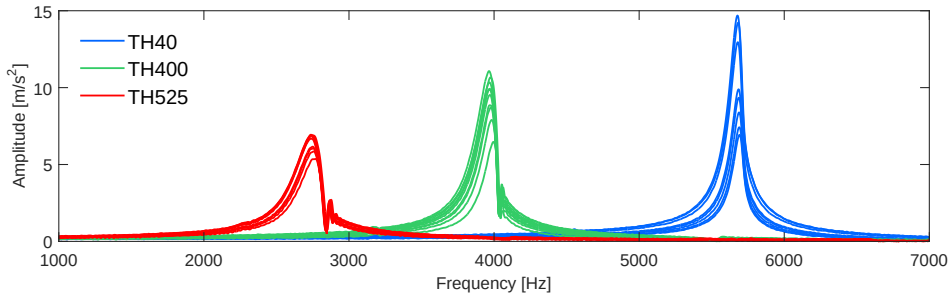

Figure 6.13. Representative resonance spectra obtained at different impact energies for one mortar sample at the temperatures $40^{\circ}C$ (blue line), $400^{\circ}C$ (green line) and $525^{\circ}C$ (red line).

6.4.1 NIRAS

To evaluate the thermal damage in the mortar specimens, the hysteretic non-linearity parameters α_f^{NIRAS} and α_Q^{NIRAS} were computed on the basis of the NIRAS technique described in Section 6.2.1. Representative results of the amplitude-dependent dynamic features (resonance frequency and damping) at different temperatures ($40°C$, $400°C$ and $525°C$) are shown in Figure 6.14.

Figure 6.14(a) shows the difference in resonance frequencies versus the peak of the spectral amplitude. The linear regime frequency $\tilde{f}_0$ is the amplitude-independent resonance frequency computed in the linear regime ($A = 0$). The parameter α_f^{NIRAS} of the thermally damaged concrete was determined by the slope of the linear regressions (solid lines) of the 10 plotted results (hollow circles), which rapidly increases with the damaging temperature. Figure 6.14(b) shows the evolution of the damping as a function of the spectral amplitude, at different damage states. The linear damping factor Q_0 is also computed in the linear strain stage ($A = 0$). These results demonstrate that both hysteretic parameters are sensitive to the internal damage of the material caused by the thermal treatment, and that shifts of resonance frequency are paired with shifts in Q values.

6.4.2 NSIRAS

Unlike the NIRAS technique, the NSIRAS method investigates the non-linearity of the material using a single impact event, which allows reducing the total number of impacts. Figure 6.15 compares the variations in resonance frequency and damping factor obtained by applying the NIRAS and NSIRAS algorithms to a representative specimen. The parameters used in the NSIRAS algorithm were: window length equal to 10 periods of the signal, and a window shift equal to 30%. Figure 6.15(a) shows the relation between the resonance frequency and spectral peak amplitude, and the best fitted linear model in every damage state. The same holds for Figure 6.15(b), in which the relation between the damping factor and spectral peak amplitude is shown. The slope of the linear regressions, α_f^{NIRAS} and α_Q^{NSIRAS}, gradually increases with thermal damage, as expected. However, the relation between the resonance frequencies and the spectral peak amplitudes differs in each technique.

As seen for the theoretical model (Section 6.2.4), the STFT applied in the

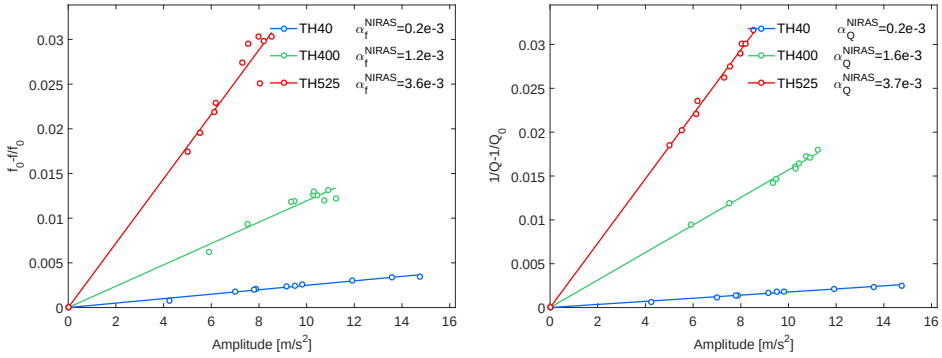

(a) (b)

Figure 6.14. NIRAS. Representative results of the amplitude-dependent dynamic features at different temperatures $40°C$ (blue), $400°C$ (green) and $525°C$ (red) computed by the NIRAS technique. The markers represent the experimental results and the straight lines represent the best fitted linear model. a) Resonance frequency shift (α_f^{NIRAS}). b) Attenuation (α_Q^{NIRAS}).

NSIRAS algorithm significantly reduces the amplitude estimation, while avoids the weighted average of the whole frequency content. It results on higher values of the linear slope α_f^{NSIRAS} than α_f^{NIRAS}. Moreover, the relation obtained from the NSIRAS algorithm between the peak amplitude values and the estimated frequencies is rather non-linear. Whereas the undamaged specimen still exhibited a fairly linear behaviour (like in the simulated model), an important deviation from the linear model is especially notable for damaged samples. According to this study, this might be due to the differences between the characteristic exponentially decaying envelope of the signal and the also exponential frequency variation (Eq. 6.2). The difference are more pronounced as the level of damage of the material increases.

Figure 6.15(b) compares the results obtained by NIRAS and NSIRAS for the amplitude-dependent damping factor. As occurred with the theoretical analysis, it can be observed that the α_Q^{NSIRAS} values are greater and less varying than α_Q^{NIRAS} due to the STFT analysis. The variable α_Q^{NSIRAS} increases with the damage although less noticeably than that observed from the NIRAS study.

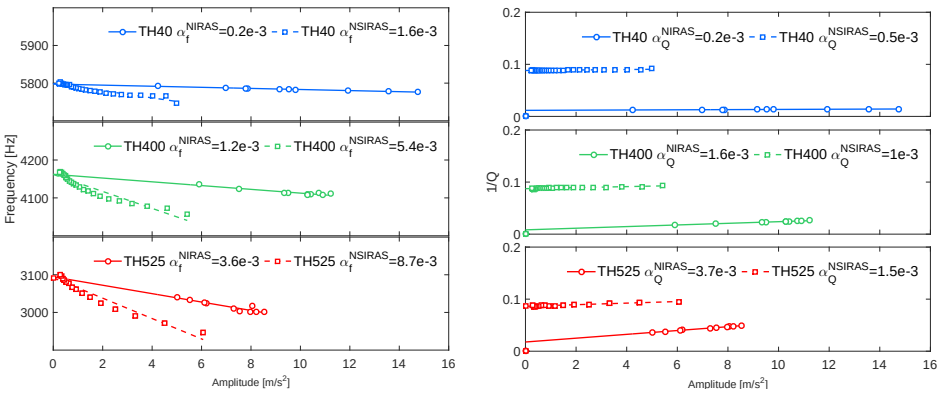

(a) (b)

Figure 6.15. NSIRAS. Comparison of representative results for the amplitude-dependent dynamic features at different temperatures $40°C$ (blue), $400°C$ (green) and $525°C$ (red) computed by NIRAS (solid lines) and NSIRAS (dashed lines). The markers represent the experimental results and the straight lines represent the best fitted linear model. a) Resonance frequency shift (α_f^{NIRAS} and α_f^{NSIRAS}). b) Attenuation (α_Q^{NIRAS} and α_Q^{NSIRAS}).

Lastly, it must be noted that this processing approach is very sensitive to the input parameters (window length) and its relation with the reverberation signal under study (f_0/f_s). A bigger window length implies lower frequency variations but greater attenuation variations due to the averaging of the frequency content in the temporal window and the corresponding bandwidth. This implies that similar studies which determine the non-linear parameters cannot be compared if the number of periods of the signal per window is not the same.

6.4.3 FANSIRAS

Like the NSIRAS technique, the new proposed FANSIRAS algorithm analyses the hysteretic behaviour of the material from the reverberation signal coming from the strongest strength impact. Figure 6.16 compares some representative results of the reference NIRAS technique and the new proposed FANSIRAS technique. The parameters used in the FANSIRAS algorithm

were a window with initial length equal to the acquired signals, N equal to 10000 samples, which progressively decreases by 400 samples until reaching a window with a quality factor lower than the previous one.

Figure 6.16(a) plots the relation between the resonance frequency and the spectral peak amplitude, and the best fitted linear model in every damage state. The starting point of the regression (highest amplitude values) obviously coincides for both techniques since the analysed signals are the same. The linear regressions are equivalent, but the FANSIRAS algorithm evolves to values of lower amplitudes and higher linear frequencies along the ringdown of the signal. This effect supposes a slight upwards bias of the slope of the estimated linear regression, as will be seen later, and this is more pronounced as the damage of the material increases. This means that the new proposed approach slightly overcomes the drawback to the analytical procedure present in the NIRAS algorithm technique, and previously noticed in [123]. It was pointed out that the frequency shift may be evaluated in a relatively limited dynamic range of amplitude values. FANSIRAS gets to increase the measurable dynamic range from smaller peak amplitudes to the same largest value, which improves the sensitivity when estimating the linear regime parameters ($\tilde{f}_0$ and Q_0).

Figure 6.16(b) compares the variation of the damping obtained both from the NIRAS and FANSIRAS techniques. It can be observed that FANSIRAS algorithm allows estimating the damping values equivalently to the NIRAS algorithm from a single signal also for real signals. The hysteretic parameter $\alpha_Q^{FANSIRAS}$ clearly classifies the level of damage following the variations of the damping factor.

6.4.4 Comparison

In this study, it has been suggested that the single signal based algorithms, NSIRAS and FANSIRAS, have to be applied to the signals from the impact of greatest strength in order to ensure that the peak frequency variable ranges up to its maximum value. Figure 6.17 compares the evolution of the non-linear hysteretic features, α_f and α_Q, for each technique (NIRAS, NSIRAS and FANSIRAS) and each impact strength on a representative example at the different studied levels of damage. In each plot, α_f^{NIRAS} and α_Q^{NIRAS} are the constant reference values obtained from the 10 impact signals. For NSIRAS (dashed lines) and FANSIRAS (dotted lines), different

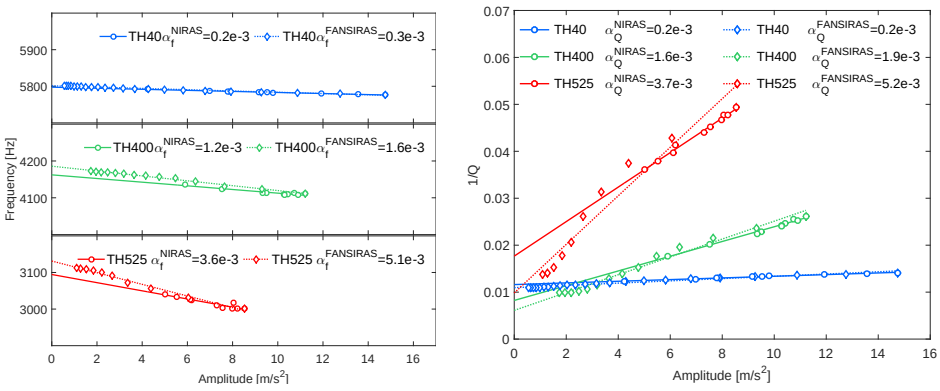

(a) (b)

Figure 6.16. FANSIRAS. Comparison of representative results of the amplitude-dependent dynamic features at different temperatures $40°C$ (blue), $400°C$ (green) and $525°C$ (red) computed by NIRAS (solid lines) and FANSIRAS (dotted lines). The markers represent the experimental results and the straight lines represent the best fitted linear model. a) Resonance frequency shift (α_f^{NIRAS} and $\alpha_f^{FANSIRAS}$). b) Attenuation (α_Q^{NIRAS} and $\alpha_Q^{FANSIRAS}$).

results are obtained for each impact signal level. For the three analysed levels of damage, α_f^{NSIRAS} and α_Q^{NSIRAS} yield closer values to the reference results for higher levels of impact. However, the results obtained by the new proposed technique, $\alpha_f^{FANSIRAS}$ and $\alpha_Q^{FANSIRAS}$, seemed to be more robust against the different impacts.

Resonance tests were performed on all the mortar pieces fabricated (9 specimens) to ensure the reproducibility of the hysteretic measurements. The robustness test results are shown in Figure 6.18, and they confirm that the non-linear resonance vibration tests can provide a consistent measure of the internal damage of the specimens. Particularly for each studied technique, the resulting trends coincides with the results seen both for the simulated model (Section 6.2.4) and for the representative example described in previous Sections 6.4.1, 6.4.2 and 6.4.3. The NIRAS technique is considered to be the reference result. The previously proposed NSIRAS technique is biased upwards when measuring the frequency shift (α_f) and significantly down biased when measuring the amplitude-dependent damping factor.

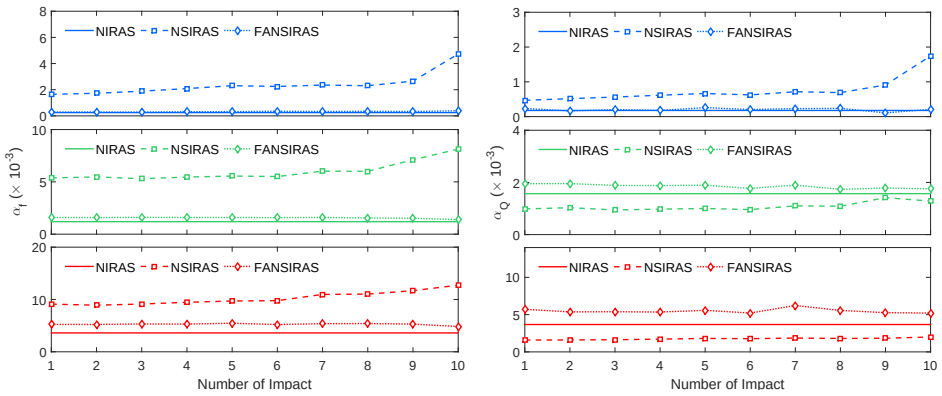

Figure 6.17. Comparison of the evolution of the non-linear hysteretic features for each technique, NIRAS (solid lines), NSIRAS (dashed lines) and FANSIRAS (dotted lines), and each impact strength, on a representative example at the different studied levels of damage, $40°C$ (blue), $400°C$ (green) and $525°C$ (red). a) α_f, b) α_Q.

The brand-new technique FANSIRAS coincides with the NIRAS results for undamaged results. However, they are slightly up biased when damage is present. This trend has previously been justified due to the analysis done by FANSIRAS up to lower amplitude values along the ring down.

Because the linear parameters $\tilde{f}_0$ and Q_0 are estimated independently of the value of the amplitude of the weaker impact, the hysteretic parameters α_f and α_Q are equivalent for both the NIRAS and FANSIRAS techniques. This is a result that has never before been diffused, as far as the authors' knowledge extends, but which is explained since both features are proportional to the same underlying hysteric behaviour of the material.

Figure 6.19 plots the root mean square error (RMSE) computed for all the experimental results versus the obtained linear fits. Whereas for undamaged specimens the regressions still exhibit fairly linear relations, the relations become rather non-linear for the damaged specimen tests. This behaviour is closely correlated to the need to use higher order coefficients in Equation 6.1. Particularly, the high value of $\alpha_Q^{FANSIRAS}$ for TH525 is due to its characteristic S-shape data distribution as the level of damage

increases (Fig. 6.16(b)). The characteristic S-shape is directly attributed to Q parameter estimation: the difference appears when computing the lowest frequency bound, f_1 (Eq. 6.19), closely related to the stiffness of the material for the highest amplitude deformations. This difference might be related to the nature of the signals used in each spectroscopy technique. NIRAS procedure estimates non-linear hysteretic parameters from original and several impact signals, however, FANSIRAS algorithm estimates the different strain levels from a single relaxing signal. The fact of f_1 being in the denominator might boost the S-shape trajectory.

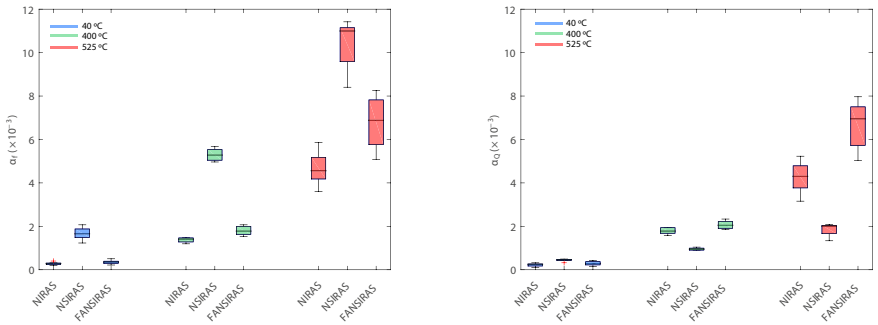

Figure 6.18. Comparing boxplots of the results of the amplitude-dependent dynamic features at different temperatures $40°C$ (blue), $400°C$ (green) and $525°C$ (red) computed by the different analysed techniques: NIRAS, NSIRAS and FANSIRAS. a) Resonance frequency shift (α_f). b) Attenuation (α_Q).

6.5 Conclusions

In this study, a new method to evaluate non-linear behaviour in materials is presented. NIRAS is the traditional resonant method to determine the non-linearity of mesoscopic materials; it uses several impacts. The proposed so-called FANSIRAS procedure is focused on obtaining the same results as the traditional technique but by analysing only a single impact. Both techniques, along with the NSIRAS procedure, have been analysed in detail,

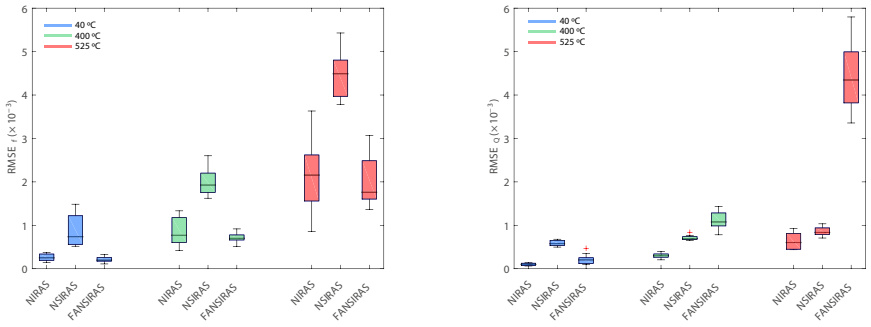

(a) (b)

Figure 6.19. Comparing boxplots of the root mean square error (RMSE) for the amplitude-dependent dynamic features at different temperatures $40°C$ (blue), $400°C$ (green) and $525°C$ (red) computed by the different analysed techniques: NIRAS, NSIRAS and FANSIRAS. a) Resonance frequency shift ($RMSE_f$). b) Attenuation ($RMSE_Q$).

based on their mathematical backgrounds, and compared in terms of their estimations for a proposed simulated model and the damage level of heat-exposed mortar.

The FANSIRAS algorithm takes advantage of the appropriate processing of a single reverberation signal to estimate equivalent acquisitions to those obtained from NIRAS with its several blow impacts. This novel procedure respects the underlying phenomena, composed of both an exponentially decaying signal and a time-varying phase signal, which results in the feasibility of using a single impact to evaluate the non-linear features of damaged materials. Both, the theoretical and the experimental results have shown that the downward frequency shifts and the damping changes are equivalent for NIRAS and FANSIRAS techniques. It has been concluded that the variation of the damping factor Q with the amplitude is exclusively sensitive to changes on the bandwidth. There is not an amplitude-dependent attenuation. Moreover, a special effort has been made to standardize the technique regardless of the acquisition equipment (accelerometer sensitivity, f_s, N) and the computation variables (N_{DFT}) in order for the results to be reproducible in further studies. The application of the FANSIRAS analysis may have important uses in industrial applications in that the quality control

can then be conducted through a single resonance frequency measurement.

7 Conclusions

7 Conclusions

The overall aim of this research has been to deepen the study of the characterization of the modality of acoustic signals, especially as applied to non-destructive applications. The motivation for this research came from the necessity of developing alternative detection/characterization algorithms, not only from the signal processing point of view, but also for civil engineers who need to improve their characterization procedures.

This chapter summarizes the findings of this research, revisiting the research objectives given in the introductory chapter. First, Section 7.1 reviews the contents of this thesis, outlining the main conclusions that were extracted from each chapter. Section 7.2 contains a list of publications during the course of work as a PhD candidate. In addition, recommendations for future research will be discussed in the final section.

7.1 Main Contributions

The initial hypothesis was to characterize the nature of the signal in a blind way, without having a priori knowledge of the input excitation of the system under study. In order to do that, the phase space reconstruction problem had to be addressed. Previously published techniques need to have

some a priori knowledge of the origin of the signal. We have proposed an alternative procedure based on RQA which allows estimating the optimal embedding parameters without any information about the nature of the signal.

Delving into the concept of determinism and quantifying its level in a given signal has turned out to be the philosopher's stone for ultrasonic material inspection applications. Firstly, this approach has been developed to estimate the level of porosity of cement paste specimens. This approach was verified by three different algorithms and an alternative index based on higher order statistics, showing a linear correlation between the amount of inner pores in the material and the degree of determinism of its pulse-echo signals. Measuring the degree of determinism has demonstrated a proportionality to the inner structure of the material. Furthermore, the same approach has been exploited to quantify the level of damage of different concrete specimens in non-destructive studies.

Two different damage treatments, an external sulphate attack and a step loading process, have been thoroughly characterized by means of traditional ultrasound measures (attenuation and pulse velocity) and the degree of determinism. This novel procedure has been shown to be more robust than the traditional approaches, particularly in indirect measurement dispositions, where the ultrasonic waves travels through different paths and may mix as a function of the internal damage. Unlike the attenuation measurement, based on the linear theory, it is able to explore the level of randomness with which the different pulses combine. This result has been properly protected under patent rights.

The study of the non-linearity/complexity of a temporal series has been addressed using hypothesis tests. To do that, we have focused both on surrogate data generation algorithms and statistical tests. The main pursuit has been the development of new tools to deal with real world non-linear signals, which habitually come with strong non-stationarities. Unfortunately, being strictly critical as to the different stages of the procedure, the authors cannot claim that this approach will work on real applications. Nevertheless, this study has involved an arduous work of research that has allowed deepening the concept and proposing an alternative surrogate data algorithm which has been proven to be useful for testing complexity in short oscillatory signals.

Due to the aforementioned lack of confidence when applying blind hypothe-

sis tests to real world signals, the non-linear approach has been significantly modified. We have deepened the non-linear resonance acoustic spectroscopy technique. A new theoretical model that explains the underlying mechanism of vibration in a concrete probe has been developed. Based on it, a new signal processing approach has been also developed (FANSIRAS). This scheme allows a single impact reverberation test compared to the ten impacts needed before, apart from the understanding of the mechanism. This approach may have significant applications in industrial quality control, where time and effort are variables to be optimized.

In short, this work provides insight into the importance and the advantages of signal modality in the signal processing field of work. Particularly for civil engineers, this study not only eased the performance, but also provides further information. The degree of determinism and the ease of employing the FANSIRAS algorithm convert this thesis to an interesting support tool for future material characterization studies.

7.2 List of Publications

A list of published work produced during the course of candidature for the degree is presented in what follows.

Refereed ISI Journals

- **Alicia Carrión García**, Ramón Miralles Ricós, Guillermo-Fernán Lara Martínez. "Measuring Predictability in Ultrasonic Signals: An Application to Scattering Material Characterization". Ultrasonics, Elsevier, vol. 54, pp. 1904 - 1911, 2014.

- **Alicia Carrión García**, Vicente Genovés Gómez, Jorge Gosálbez Castillo, Ramón Miralles Ricós, Jordi Payá Bernabeu. "Ultrasonic Signal Modality: A novel approach for concrete damage evaluation". Cement and Concrete Research, Elsevier, 101, pp. 25 - 32, 2017.

- Ramón Miralles Ricós, **Alicia Carrión García**, David Looney, Guillermo Fernán Lara Martínez, Danilo Mandic. "Characterization of the complexity in short oscillating time series: An application to seis-

mic airgun detonations". Journal of the Acoustical Society of America. 138, pp. 1595 - 1603, 2015.

- Jorge Gosálbez Castillo, W. M. D. Wright, W. Jiang, **Alicia Carrión García**,Vicente Genovés Gómez, Ignacio Bosch Roig. "Airborne non-contact and contact broadband ultrasounds for frequency attenuation profile estimation of cementitious materials". Ultrasonics, Elsevier, vol. 88, pp. 148-156 , 2018.

- Apit Hemakon, Theerasak Chanwimalueang, **Alicia Carrión García**, Lisa Aufegger, Anthony G. Constantinides, Danilo P. Mandic. "Financial Stress through Complexity Science". IEEE Journal of Selected Topics in Signal Processing. 10 - 6, pp. 1112 - 11126. IEEE, 2016.

- Vicente Genovés Gómez, Fabio Vargas, Jorge Gosálbez Castillo, **Alicia Carrión García**, M. Victoria Borrachero, Jordi Payá Bernabeu. "Ultrasonic and impact spectroscopy monitoring on internal sulphate attack of cement-based materials". Materials & Design, Elsevier, vol. 125, pp. 46 - 54, 2017.

- Vicente Genovés Gómez, Jorge Gosálbez Castillo, **Alicia Carrión García**, Ramón Miralles Ricós, Jordi Payá Bernabeu. "Ultrasonic broadband signals monitoring of glass-fiber reinforced cement (GRC) bending tests". Cement and Concrete Composites, Elsevier, vol. 80, pp. 55 - 63, 2017.

- Vicente Genovés Gómez, Jorge Gosálbez Castillo, **Alicia Carrión García**, Ramón Miralles Ricós, Jordi Payá Bernabeu. "Optimized ultrasonic attenuation measures for non-homogeneous materials". Ultrasonics, Elsevier, vol. 65, pp. 345 - 352, 2016.

- Ramón Miralles Ricós, Guillermo Fernán Lara Martínez, **Alicia Carrión García**, Jose Antonio Esteban. "Automatic Detection and Classification of Beluga Whale Vocalizations". Advances in Applied Acoustics (AIAAS), num. 2, vol. 2, pp. 61 - 70, 2012.

Peer-reviewed non-ISI Journals

- **Alicia Carrión García**, Guillermo-Fernán Lara Martínez, Ramón Miralles Ricós, Jorge Gosálbez Castillo, Ignacio Bosch Roig. "On the use of Recurrence Quantification Analysis for Signal Modality Characterization: two applications". WAVES, num. 7, pp. 5 - 14, 2015.

- Ramón Miralles, Guillermo Lara Martinez, **Alicia Carrión García** and José Antonio Esteban. "SAMARUC a programmable system for passive acoustic monitoring of cetaceans". WAVES, num. 5, pp. 5 - 12, 2013.

Papers in International Conferences

- **Alicia Carrión García**, Vicente Genovés Gómez, Ramón Miralles Ricós, Jordi Payá Bernabeu, Jorge Gosálbez Castillo. "An advanced ultrasonic method based on signal modality for structural damage characterization on concrete: the cube problem", 2017 IEEE International Ultrasonics Symposium, Washington D.C., 2017.

- Vicente Genovés Gómez, **Alicia Carrión García**, Jorge Gosálbez Castillo, Ignacio Bosch Roig, M. Victoria Borrachero, Jordi Payá Bernabeu. "Optimized ultrasonic attenuation measures for internal sulphate attack monitoring in Portland cement mortars", 2017 IEEE International Ultrasonics Symposium, Washington D.C., 2017.

- **Alicia Carrión García**, Guillermo-Fernán Lara Martínez, Ramón Miralles Ricós, Jorge Gosálbez Castillo, Ignacio Bosch Roig. "Characterizing the mechanisms of sound production in odontocetes: A signal modality approach", 22^{nd} IEEE International Conference on Digital Signal Processing (DSP 2017), London, 2017.

- Ramón Miralles Ricós, Guillermo-Fernán Lara Martínez, **Alicia Carrión García**, Jorge Gosálbez Castillo, Ignacio Bosch Roig. "On the detection of impulsive and tonal events in passive acoustics monitoring", 22^{nd} IEEE International Conference on Digital Signal Processing (DSP 2017), London, 2017.

- **Alicia Carrión García**, Theerasak Chanwimalueang, Giuseppe Giovanni Calvi, Apit Hemakom, Ramón Miralles Ricós, Danilo Mandic. "Modelling economic stress through financial systemic balance index". 2016 IEEE International Conference on Digital Signal Processing (DSP 2016). pp. 565 - 569. 2016.

International Conferences

- **Alicia Carrión García**, Ramón Miralles Ricós. "Complexity characterization based on surrogate data for short oscillation time series". International Conference on Perspectives in Nonlinear Dynamics (PNLD 2016), Berlin 2016.

- **Alicia Carrión García**, Guillermo-Fernán Lara Martínez, Ramón Miralles Ricós. "Scattering material characterization based on Recurrence Plots Quantifycation Analysis (RQA)". Sixth International Symposium on Recurrence Plots, Grenoble 2015.

- Ramón Miralles Ricós, **Alicia Carrión García** Guillermo-Fernán Lara Martínez. "Computing the Delay Vector Variance using Recurrence Plots". Sixth International Symposium on Recurrence Plots, Grenoble 2015.

- Guillermo-Fernán Lara Martínez, Ramón Miralles Ricós, **Alicia Carrión García**. "Right Whale activity detector and sound classificator using Mel-frequency Cepstral Coefficients". 6^{th} International Workshop on Detection, Classification, Localization, and Density Estimation of Marine Mammals using Passive Acoustics (DCLDE 2013), St. Andrews (Scotland), 12-15 June, 2013.

- **Alicia Carrión García**, Ramón Miralles Ricós, Guillermo-Fernán Lara Martínez. "Nonlinear phenomena based detector for passive acoustic monitoring". 6^{th} International Workshop on Detection, Classification, Localization, and Density Estimation of Marine Mammals using Passive Acoustics (DCLDE 2013), St. Andrews (Scotland), 12-15 June, 2013.

Papers in National Conferences

- **Alicia Carrión García**, Ramón Miralles Ricós, Vicente Genovés, Gómez Jorge Gosálbez Castillo, Jordi Payá Bernabeu. "Nuevo método ultrasónico basado en el determinismo. Aplicación al caso de daño térmico en morteros de cemento Portland". I Congreso Nacional PRE-CONPAT 16, Madrid, 2016.

Book Chapter

- **Alicia Carrión García**, Ramón Miralles Ricós. "New insights for testing linearity and complexity with surrogates: a Recurrence Plots approach. Recurrence Plots and their Quantifications: Expanding Horizons". 180 - 1, pp. 91 - 112. Springer Proceedings Phys., 2016.

Patents

- **Alicia Carrión García**, Vicente Genovés Gómez, Jorge Gosálbez Castillo, Ramón Miralles Ricós, Jordi Payá Bernabeu. "Método de Ensayo del Estado de Materiales", Universidad Politécnica de Valencia, P201630212, Spain, Community of Madrid, 25/02/2016.

Research Stay

- Imperial College London under the supervision of Prof. Danilo Mandic. 3 months. July 2015.

7.3 Future Work

Following the investigations described in this thesis, the main lines of research that remain open are listed below:

- Despite having been widely used in applications with concrete, the determinism parameter should be evaluated in new materials, as well

as in different measurement configurations. A possible field of application that has recently emerged would be the manufacture of pieces by 3D printing, where the design is usually unique and the piece cannot be subjected to destructive tests.

- Application of the algorithms of complexity of short oscillatory signals in modal conversion between pressure waves (also known as P-waves) and shear waves (S-waves) in the estimation of rheological properties. The main goal is detecting the setting, hardening and curing stages of the concrete, parameters correlated to physical properties of the material.
- Application of the proposed non-linear model to the acoustic resonance phenomenon in real applications. The idea is the parametrization of real experiences as a new way of non-linear characterization. The parameters to extract would be γ, and both frequencies, f_{min} and f_{max}.
- The equivalence between the algorithm of NIRAS in downward configuration, and the proposed FANSIRAS algorithm has been demonstrated. However, significant differences can be seen between the NIRAS technique in upward configuration (with the previous rest of the specimen) and the FANSIRAS algorithm. In future studies, these differences should be studied, as well as understanding the apparent memory mechanisms. Both techniques jointly (upward NIRAS and FANSIRAS) may model the hysteresis area of a non-linear material.

In short, signal modality might be the foundation for futures studies of complex non-linear phenomena. Getting knowledge about the underlying systems may provide crucial information to develop easier and optimal signal processing algorithms not only in the non-destructive testing of concrete, but also in further applications, such as biomedicine, acoustics, etc.

7.4 Institutional Acknowledgements

This work has received financial support of the following projects:

- Ayuda Subprograma de Formación de Personal Investigador (BES-2012-051960).

- Algoritmos para el Análisis de la Modalidad de la Señal: Aplicación en el procesado avanzado de señales acústicas (TEC2011-23403).

- Nuevas Aplicaciones de Ensayos No Destructivos basados en Ondas Mecánicas para la Evaluación de la Degradación en Materiales Cementantes (BIA2014-55311-C2-2-P).

Abbreviations and Acronyms

AAFT	Amplitude Adjusted Fourier Transform
AR	Autoregressive Models
ARMA	Autoregressive Moving Average Models
BWE	Back Wall Echo
DAKDS	Determinism based on the Average Kurtosis
DET	Determinism based on the Recurrence Plots
DFT	Discrete Fourier Transform
DJM	Determinism based on the Jeong Method
DMKG	Determinism based on the Kaplan-Glass Method
DP	Distance Plot
DV	Delay Vector
DVRQA	Delay Vector based on RQA
DVV	Delay Vector Variance
EEG	Electroencephalography
e.g.	for example (from the latin exempli gratia)
ENTR	Entropy
ESA	External Sulphate Attack
FANSIRAS	Flipped Accumulative NSIRAS
FNN	False Nearest Neighbour
FT	Fourier Transform
GN	Grain Noise
GOR	Grain-to-Observation-Noise-Ratio
HNR	Harmonic to Noise Ratio
HR	Humidity Relative
HRV	Heart Rate Variability
i.e.	that is (from the latin id est)
iAAFT	Iterative Amplitude Adjusted Fourier Transform
INRS	Impact Non-linear Resonance Spectroscopy
ISA	Internal Sulphate Attack
LAM	Laminarity
MI	Mutual Information
MODWT	Maximal Overlap DiscreteWavelet Transform
MSE	Mean Squared Error

NDT	Non-Destructive Testing
NEWS	Non-linear Elastic Wave Spectroscopy
NIRAS	Non-linear Impact Resonance Acoustic Spectroscopy
NRS	Non-linear Resonance Spectroscopy
NRUS	Non-linear Resonance Ultrasonic Spectroscopy
NSIRAS	Non-linear Single Impact Resonance Acoustic Spectroscopy
NWMS	Non-linear Wave Modulation Spectroscopy
ON	Observation Noise
PPS	Pseudoperiodic Surrogates
PPTS	Pseudo-Periodic Twin Surrogates
PSR	Phase Space Reconstruction
RP	Recurrence Plot
RQA	Recurrence Quantification Analysis
RMSE	Root Mean Square Error
RR	Recurrence Rate
STFT	Short Time Fourier Transform
SIMONRAS	Single Mode Non-linear Resonance Acoustic Spectroscopy
SIMONRUS	Single Mode Non-linear Resonance Ultrasonic Spectroscopy
SNR	Signal to Noise Ratio
SSM	Scaling Substraction Method
STFT	Short-time Frequency Transform
TS	Twin Surrogates
TT	Trapping Time
UPV	Ultrasonic Pulse Velocity
US	Ultrasounds
WiAAFT	Wavelet Iterative Amplitude Adjusted Fourier Transform
w/c	Water to Cement Ratio

List of symbols

t	Continuous time
n	Discrete time
$x(\cdot)$	Input signal
$y(\cdot)$	Output signal
Δt	Time step
f	Frequency
w_0	Angular frequency
λ	Wavelength
T	Period
T_s	Time sampling
f_s	Sampling frequency
N	Number of samples of a signal
$X[f]$	Fourier Transform of the signal x
N_{DFT}	Number of points used in the DFT
L	Discrete time lag
τ	Continuous time lag
m	Real embedding dimension
E	Optimal found embedding dimension
$\vec{X}(\cdot)$	Delay vector of the phase space
$\vec{X}_{L,E}(\cdot)$	Delay vector of the phase space recontructed with the embedding parameters L and E
$\mathbf{f}(\cdot)$	Continuous time evolution function
$\mathbf{F}(\cdot)$	Discrete time evolution function
$\frac{d}{dt}(\cdot)$	Differential equation
$s(\cdot)$	Measurement function
$\eta(\cdot)$	Measurement noise
$(\cdot)^{\mathrm{T}}$	Transpose
$(\cdot)^*$	Complex conjugation
$\lvert \cdot \rvert$	Absolute value
$\lVert \cdot \rVert$	2 norm
$\lVert \cdot \rVert_{max}$	Maximum norm
$\sum_i^j(\cdot)$	Summation sign
max	Maximum of a set

min	Minimum of a set
log	Natural logarithm
$\log_{10}$	Decimal logarithm
$P_x(i)$	Probability that the signal x assumes a value inside the i-th bin of the histogram
$\log_{10}$	Decimal logarithm
$\Theta(\cdot)$	Heaviside step function of $\cdot$
$sgn(\cdot)$	Sign function of $\cdot$
$\lfloor \cdot \rfloor$	The greatest integer less than or equal to $\cdot$
$\mathbb{R}$	Set of real numbers
$sin(\cdot)$	Sinusoidal function
$cos(\cdot)$	Cosine function
$arccos(\cdot)$	Inverse of the cosine function
$\exp(\cdot)$	Exponential function
$*$	Convolution
$E[\cdot]$	Expected value
$c_4^x(\cdot,\cdot,\cdot)$	Forth order cumulant function
E_j	j-th octile of the distribution of data
σ^2	Variance
$DP(i,j)$	Distance between $\vec{X}(i)$ and $\vec{X}(j)$
$RP(i,j)$	Recurrence Plot between $\vec{X}(i)$ and $\vec{X}(j)$
ε	Recurrence threshold
v	Vertical lines
l	Diagonal lines
$x_t(\cdot)$	Target value
N_S	Number of surrogates
r_d	Standard distance
N_o	Number of sets of points
D	Diameter of the aggregates
$d_{mat}[m]$	Distance of the material
$v_p[m/s]$	Ultrasonic pulse velocity
$t_a[s]$	Time of arrival
$\alpha_{mat}[dB/cm]$	Ultrasonic attenuation due to the material
$\alpha_{equip}[dB/cm]$	Ultrasonic attenuation due to the equipment
s_{rx}	Received signal
P_{tx}, P_{rx}	Transmitted and received power, respectively
A_{tx}, A_{rx}	Amplitude of the transmitted and received signal, respectively
ϵ	Strain amplitude

K	Non-linear hysteretic modulus
K_0	Linear modulus
$\tilde{f}_0$	Linear frequency
Q_0	Linear damping factor
$w^L(\cdot)$	Rectangular window of length L
α_f	Hysteretic parameter proportional to frequency shift
α_Q	Hysteretic parameter proportional to damping factor

List of Figures

List of Tables

Bibliography

[1] B. Jelfs, S. Javidi, P. Vayanos, and D. Mandic, "Characterisation of signal modality: Exploiting signal nonlinearity in machine learning and signal processing," *Journal of Signal Processing Systems*, vol. 61, no. 1, pp. 105–115, 2010.

[2] T. Schreiber, "Interdisciplinary application of nonlinear time series methods," *Physics reports*, vol. 308, no. 1, pp. 1–64, 1999.

[3] D. Mandic, M. Golz, A. Kuh, D. Obradovic, and T. Tanaka, *Signal processing techniques for knowledge extraction and information fusion*. Springer, 2008.

[4] P. Daponte, F. Maceri, and R. Olivito, "Ultrasonic signal-processing techniques for the measurement of damage growth in structural materials," *Instrumentation and Measurement, IEEE Transactions on*, vol. 44, no. 6, pp. 1003–1008, Dec 1995.

[5] V. Malhotra and N. Carino, *Handbook on Nondestructive Testing of Concrete*, ser. Civil engineering. CRC Press, 2004.

[6] F. Ghasemzadeh, R. Rashetnia, D. Smyl, and M. Pour-Ghaz, "A comparison of methods to evaluate mass transport in damaged mortar," *Cement and Concrete Composites*, vol. 70, pp. 119 – 129, 2016.

[7] R. B. Thompson, "Quantitative ultrasonic nondestructive evaluation methods," *Journal of Applied Mechanics*, vol. 50, no. 4b, p. 1191, 1983.

[8] M. Molero, S. Aparicio, G. Al-Assadi, M. Casati, M. Hernndez, and J. Anaya, "Evaluation of freeze-thaw damage in concrete by ultrasonic imaging," *NDT & E International*, vol. 52, pp. 86 – 94, 2012.

[9] "Integrated non-destructive assessment of concrete structures under flexure by acoustic emission and travel time tomography," *Construction and Building Materials*, vol. 67, pp. 202 – 215, 2014, 1. Special Issue of KIFA-6 2. Utilization of Crumb Rubber in Asphalt Mixtures.

[10] K. Van Den Abeele and J. De Visscher, "Damage assessment in reinforced concrete using spectral and temporal nonlinear vibration techniques," *Cement and Concrete Research*, vol. 30, no. 9, pp. 1453–1464, 2000.

[11] A. Moussatov, V. Gusev, and B. Castagnede, "Self-induced hysteresis for nonlinear acoustic waves in cracked material," *Physical review letters*, vol. 90, no. 12, p. 124301, 2003.

[12] P. Duffour, M. Morbidini, and P. Cawley, "A study of the vibro-acoustic modulation technique for the detection of cracks in metals," *The Journal of the Acoustical Society of America*, vol. 119, no. 3, pp. 1463–1475, 2006.

[13] C. Bruno, A. Gliozzi, M. Scalerandi, and P. Antonaci, "Analysis of elastic nonlinearity using the scaling subtraction method," *Physical Review B*, vol. 79, no. 6, p. 064108, 2009.

[14] P. Antonaci, C. Bruno, P. Bocca, M. Scalerandi, and A. Gliozzi, "Nonlinear ultrasonic evaluation of load effects on discontinuities in concrete," *Cement and Concrete Research*, vol. 40, no. 2, pp. 340 – 346, 2010.

[15] K. J. Lesnicki, J.-Y. Kim, K. E. Kurtis, and L. J. Jacobs, "Characterization of asr damage in concrete using nonlinear impact resonance acoustic spectroscopy technique," *NDT & E International*, vol. 44, no. 8, pp. 721 – 727, 2011.

[16] S.-J. Park, H. J. Yim, and H.-G. Kwak, "Nonlinear resonance vibration method to estimate the damage level on heat-exposed concrete," *Fire Safety Journal*, vol. 69, pp. 36 – 42, 2014.

[17] J. Chen, A. R. Jayapalan, J.-Y. Kim, K. E. Kurtis, and L. J. Jacobs, "Rapid evaluation of alkali-silica reactivity of aggregates using a nonlinear resonance spectroscopy technique," *Cement and Concrete Research*, vol. 40, no. 6, pp. 914 – 923, 2010.

[18] V. Genovs, L. Soriano, M. Borrachero, J. Eiras, and J. Pay, "Preliminary study on short-term sulphate attack evaluation by non-linear impact resonance acoustic spectroscopy technique," *Construction and Building Materials*, vol. 78, pp. 295 – 302, 2015.

[19] E. Tsangouri, G. Karaiskos, A. Deraemaeker, D. V. Hemelrijck, and D. Aggelis, "Assessment of acoustic emission localization accuracy on damaged and healed concrete," *Construction and Building Materials*, vol. 129, pp. 163 – 171, 2016.

[20] J. Geng, Q. Sun, Y. Zhang, L. Cao, and W. Zhang, "Studying the dynamic damage failure of concrete based on acoustic emission," *Construction and Building Materials*, vol. 149, pp. 9 – 16, 2017.

[21] R. M. May, "Simple mathematical models with very complicated dynamics," *Nature*, vol. 261, pp. 459–467, Jun 1976.

[22] F. Takens, "Detecting strange attractors in turbulence," pp. 366–381, 1981.

[23] P. Grassberger and I. Procaccia, "Characterization of strange attractors," *Physical review letters*, vol. 50, no. 5, p. 346, 1983.

[24] D. S. Broomhead and G. P. King, "Extracting qualitative dynamics from experimental data," *Physica D: Nonlinear Phenomena*, vol. 20, no. 2-3, pp. 217–236, 1986.

[25] L. Cao, "Practical method for determining the minimum embedding dimension of a scalar time series," *Physica D: Nonlinear Phenomena*, vol. 110, no. 1-2, pp. 43–50, 1997.

[26] T. Gautama, D. P. Mandic, and M. M. Van Hulle, "A differential entropy based method for determining the optimal embedding parameters of a signal," vol. 6, pp. VI–29, 2003.

[27] E. R. Deyle and G. Sugihara, "Generalized theorems for nonlinear state space reconstruction," *PLoS One*, vol. 6, no. 3, p. e18295, 2011.

[28] H. Whitney, "Differentiable manifolds," *Annals of Mathematics*, vol. 37, no. 3, pp. 645–680, 1936.

[29] M. Casdagli, S. Eubank, J. D. Farmer, and J. Gibson, "State space reconstruction in the presence of noise," *Physica D: Nonlinear Phenomena*, vol. 51, no. 1-3, pp. 52–98, 1991.

[30] J. F. Gibson, J. D. Farmer, M. Casdagli, and S. Eubank, "An analytic approach to practical state space reconstruction," *Physica D: Nonlinear Phenomena*, vol. 57, no. 1, pp. 1–30, 1992.

[31] A. Fraser and H. Swinney, "Independent coordinates for strange attractors from mutual information," *Phys. Rev. A*, vol. 33, pp. 1134–1140, Feb 1986.

[32] C. E. Shannon, "A mathematical theory of communication," *Bell system technical journal*, vol. 27, no. 3, pp. 379–423, 1948.

[33] M. B. Kennel, R. Brown, and H. D. I. Abarbanel, "Determining embedding dimension for phase-space reconstruction using a geometrical construction," *Phys. Rev. A*, vol. 45, pp. 3403–3411, Mar 1992.

[34] J. P. Eckmann, S. O. Kamphorst, and D. Ruelle, "Recurrence plots of dynamical systems," *Europhysics Letters (EPL)*, vol. 4, no. 9, pp. 973–977, Nov 1987.

[35] N. Marwan, N. Wessel, U. Meyerfeldt, A. Schirdewan, and J. Kurths, "Recurrence-plot-based measures of complexity and their application to heart-rate-variability data," *Phys. Rev. E*, vol. 66, p. 026702, Aug 2002.

[36] D. P. Lathrop and E. J. Kostelich, "Characterization of an experimental strange attractor by periodic orbits," *Physical Review A*, vol. 40, no. 7, Oct. 1989.

[37] N. Marwan, N. Wessel, U. Meyerfeldt, A. Schirdewan, and J. Kurths, "Recurrence-plot-based measures of complexity and their application to heart-rate-variability data," *Physical review E*, vol. 66, no. 2, p. 026702, 2002.

[38] C. L. Webber and J. P. Zbilut, "Dynamical assessment of physiological systems and states using recurrence plot strategies," *Journal of Applied Physiology*, vol. 76, no. 2, pp. 965–973, 1994.

[39] N. Marwan, M. C. Romano, M. Thiel, and J. Kurths, "Recurrence plots for the analysis of complex systems," *Physics Reports*, vol. 438, no. 5, pp. 237–329, 2007.

[40] J. B. Gao, "Recurrence time statistics for chaotic systems and their applications," *Phys. Rev. Lett.*, vol. 83, pp. 3178–3181, Oct 1999.

[41] J. Gao and H. Cai, "On the structures and quantification of recurrence plots," *Physics Letters A*, vol. 270, no. 12, pp. 75 – 87, 2000.

[42] K. Klimaszewska and J. J. Żebrowski, "Detection of the type of intermittency using characteristic patterns in recurrence plots," *Physical review E*, vol. 80, no. 2, p. 026214, 2009.

[43] J. P. Zbilut and C. L. W. Jr., "Laminar recurrences, maxline, unstable singularities and biological dynamics," *The European Physical Journal Special Topics*, vol. 164, no. 1, pp. 55–65, 2008.

[44] R. Hegger, H. Kantz, and T. Schreiber, "Practical implementation of nonlinear time series methods: The tisean package," *Chaos: An Interdisciplinary Journal of Nonlinear Science*, vol. 9, no. 2, pp. 413–435, 1999.

[45] O. Rossler, "An equation for hyperchaos," *Physics Letters A*, vol. 71, no. 2, pp. 155 – 157, 1979.

[46] E. N. Lorenz, "Deterministic nonperiodic flow," *Journal of the Atmospheric Sciences*, vol. 20, no. 1, pp. 130 – 141, 1963.

[47] H. Kantz and T. Schreiber, *Nonlinear Time Series Analysis*. Cambridge University Press, 2004.

[48] C. Ioana, A. Digulescu, A. Serbanescu, I. Candel, and F.-M. Birleanu, "Recent advances in non-stationary signal processing based on the concept of recurrence plot analysis," in *Translational Recurrences*. Springer, 2014, pp. 75–93.

[49] L. Vergara-Dominguez and J. M. Páez-Borrallo, "Backscattering grain noise modelling in ultrasonic non-destructuve testing," *Waves in Random Media*, vol. 1, pp. 81–92, 1991.

[50] X. Li, N. Bilgutay, and R. Murthy, "Spectral histogram using the minimization algorithm-theory and applications to flaw detection," *Ultrasonics, Ferroelectrics and Frequency Control, IEEE Transactions on*, vol. 39, no. 2, pp. 279–284, 1992.

[51] K. Donohue and H. Y. Cheah, "Spectral correlation filters for flaw detection," *Ultrasonics Symposium, 1995. Proceedings., 1995 IEEE*, vol. 1, pp. 725–728 vol.1, 1995.

[52] A. Abbate, J. Koay, J. Frankel, S. Schroeder, and P. Das, "Signal detection and noise suppression using a wavelet transform signal processor: application to ultrasonic flaw detection," *Ultrasonics, Ferroelectrics and Frequency Control, IEEE Transactions on*, vol. 44, no. 1, pp. 14–26, 1997.

[53] L. Vergara, J. Gosálbez, J. Fuente, R. Miralles, and I. Bosch, "Measurement of cement porosity by centroid frequency profiles of ultrasonic grain noise," *Signal Processing*, vol. 84, no. 12, pp. 2315 – 2324, 2004.

[54] L. Vergara, J. Fuente, J. Gosálbez, R. Miralles, and I. Bosch, "Processing of ultrasonic grain noise signals for the estimation of depth- and frequency-dependent attenuation," *Measurement Science and Technology*, vol. 14, no. 7, p. 1018, 2003.

[55] R. Wayland, D. Bromley, D. Pickett, and A. Passamante, "Recognizing determinism in a time series," *Phys. Rev. Lett.*, vol. 70, pp. 580–582, Feb 1993.

[56] J. Jeong, J. C. Gore, and B. S. Peterson, "A method for determinism in short time series, and its application to stationary EEG," *IEEE Transactions on Biomedical Engineering*, vol. 49, no. 11, pp. 1374–1379, 2002.

[57] C. Courtney, S. Neild, P. Wilcox, and B. Drinkwater, "Application of the bispectrum for detection of small nonlinearities excited sinusoidally," *Journal of Sound and Vibration*, vol. 329, no. 20, pp. 4279 – 4293, 2010.

[58] J. Mendel, "Tutorial on higher-order statistics (spectra) in signal processing and system theory: theoretical results and some applications," *Proceedings of the IEEE*, vol. 79, no. 3, pp. 278–305, Mar. 1991.

[59] J. J. A. Moors, "A quantile alternative for kurtosis," *Journal of the Royal Statistical Society. Series D (The Statistician)*, vol. 37, no. 1, pp. 25–32, 1988.

[60] T.-H. Kim and H. White, "On more robust estimation of skewness and kurtosis," *Finance Research Letters*, vol. 1, no. 1, pp. 56 – 73, 2004.

[61] M. Hernández, M. Izquierdo, A. Ibez, J. Anaya, and L. Ullate, "Porosity estimation of concrete by ultrasonic {NDE}," *Ultrasonics*, vol. 38, no. 18, pp. 531 – 533, 2000.

[62] S. M. P. S. S.N. Alekseev, F. M. Ivanov, *Durability of reinforced concrete in aggressive media*. A.A. Balkema, Rotterdam, 1991.

[63] R. A. Olson, C. M. Neubauer, and H. M. Jennings, "Damage to the pore structure of hardened portland cement paste by mercury intrusion," *Journal of the American Ceramic Society*, vol. 80, no. 9, pp. 2454–2458, 1997.

[64] J. Saniie, T. Wang, and N. Bilgutay, "Analysis of homomorphic processing for ultrasonic grain signal characterization," *IEEE Transactions on Ultrasonics, Ferroelectrics and Frequency Control*, vol. 36, no. 3, pp. 365–375, 1989.

[65] N. Marwan, "How to avoid potential pitfalls in recurrence plot based data analysis," *I. J. Bifurcation and Chaos*, vol. 21, no. 4, pp. 1003–1017, 2011.

[66] V. Garnier, B. Piwakowski, O. Abraham, G. Villain, C. Payan, and J. F. Chaix, "Acoustic techniques for concrete evaluation: Improvements, comparisons and consistency," *Construction and Building Materials*, vol. 43, pp. 598 – 613, 2013.

[67] W. P. Mason and H. McSkimin, "Attenuation and scattering of high frequency sound waves in metals and glasses," *The Journal of the Acoustical Society of America*, vol. 19, no. 3, pp. 464–473, 1947.

[68] A. Carrión, R. Miralles, and G. Lara, "Measuring predictability in ultrasonic signals: An application to scattering material characterization," *Ultrasonics*, vol. 54, no. 7, pp. 1904 – 1911, 2014.

[69] V. Genovés, J. Gosálbez, A. Carrión, R. Miralles, and J. Payá, "Optimized ultrasonic attenuation measures for non-homogeneous materials," *Ultrasonics*, vol. 65, pp. 345 – 352, 2016.

[70] J. Krautkrämer and H. Krautkrämer, *Ultrasonic testing of materials*. Springer-Verlag, 1983.

[71] T. P. Philippidis and D. G. Aggelis, "Experimental study of wave dispersion and attenuation in concrete." *Ultrasonics*, vol. 43, no. 7, pp. 584–95, Jul. 2005.

[72] M. Molero, I. Segura, S. Aparicio, M. G. Hernández, and M. a. G. Izquierdo, "On the measurement of frequency-dependent ultrasonic attenuation in strongly heterogeneous materials." *Ultrasonics*, vol. 50, no. 8, pp. 824–8, Aug. 2010.

[73] M. Collepardi, "A state-of-the-art review on delayed ettringite attack on concrete," *Cement and Concrete Composites*, vol. 25, no. 4-5, pp. 401 – 407, 2003.

[74] ASTM, "ASTM C1018-97. Standard Test Method for Flexural Toughness and First-Crack Strength of Fiber-Reinforced Concrete (Using Beam With Third-Point Loading) 1," *ASTM*, vol. 04, no. C, pp. 1–8, 2011.

[75] I. E. Shkolnik, "Evaluation of Dynamic Strength of Concrete from Results of Static Tests," *Journal of Engineering Mechanics*, vol. 122, no. December, pp. 1133–1138, 1996.

[76] X. Lu, Q. Sun, W. Feng, and J. Tian, "Evaluation of dynamic modulus of elasticity of concrete using impact-echo method," *Construction and Building Materials*, vol. 47, no. 0, pp. 231 – 239, 2013.

[77] K. Lehnertz, R. G. Andrzejak, J. Arnhold, T. Kreuz, F. Mormann, C. Rieke, A. Widman, and C. E. Elger, "Nonlinear EEG analysis in epilepsy: its possible use for interictal focus localization, seizure anticipation, and prevention," *Journal of Clinical Neurophysiology: Official Publication of the American Electroencephalographic Society*, vol. 18, no. 3, pp. 209–222, 2001.

[78] W. T. Fitch, J. Neubauer, and H. Herzel, "Calls out of chaos: the adaptive significance of nonlinear phenomena in mammalian vocal production," *Animal Behaviour*, vol. 63, no. 3, pp. 407–418, 2002.

[79] D. G. McMillan, "Non-linear predictability of UK stock market returns," *Oxford Bulletin of Economics and Statistics*, vol. 65, no. 5, pp. 557–573, 2003.

[80] F. Laio, A. Porporato, L. Ridolfi, and S. Tamea, "Detecting nonlinearity in time series driven by non-Gaussian noise: the case of river flows," *Nonlinear Processes in Geophysics*, vol. 11, no. 4, pp. 463–470, Oct. 2004.

[81] P. Borgnat, P. Flandrin, P. Honeine, C. Richard, and J. Xiao, "Testing stationarity with surrogates: A Time-Frequency approach," *IEEE Transactions on Signal Processing*, vol. 58, no. 7, pp. 3459–3470, Jul. 2010.

[82] M. Small and C. K. Tse, "Detecting determinism in time series: the method of surrogate data," *IEEE Transactions on Circuits and Systems I: Fundamental Theory and Applications*, vol. 50, no. 5, pp. 663–672, May 2003.

[83] J. Theiler, S. Eubank, A. Longtin, B. Galdrikian, and J. D. Farmer, "Testing for nonlinearity in time series: the method of surrogate data," *Physica D: Nonlinear Phenomena*, vol. 58, no. 1, pp. 77 – 94, 1992.

[84] T. Schreiber and A. Schmitz, "Improved surrogate data for nonlinearity tests," *Physical Review Letters*, vol. 77, no. 4, pp. 635–638, 1996.

[85] X. Luo, T. Nakamura, and M. Small, "Surrogate test to distinguish between chaotic and pseudoperiodic time series," *Physical Review E*, vol. 71, no. 2, Feb. 2005.

[86] T. Nakamura and M. Small, "Small-shuffle surrogate data: Testing for dynamics in fluctuating data with trends," *Physical Review E*, vol. 72, no. 5, p. 056216, 2005.

[87] M. Small, D. Yu, and R. Harrison, "Surrogate test for pseudoperiodic time series data," *Physical Review Letters*, vol. 87, no. 18, 2001.

[88] C. W. Wang, *Nonlinear phenomena research perspectives.* Nova Publishers, 2007.

[89] T. Schreiber and A. Schmitz, "Improved surrogate data for nonlinearity tests," *Phys. Rev. Lett.*, vol. 77, pp. 635–638, Jul 1996.

[90] D. Kaplan, "Nonlinearity and Nonstationarity: The Use of Surrogate Data in Interpreting Fluctuations," *Proceedings of the 3rd Annual Workshop on Computer Applications of Blood Pressure and Heart Rate Signals*, 1997.

[91] M. C. Casdagli and A. S. Weigend, *Exploring the continuum between deterministic and stochastic modeling, in Time Series Prediction: Forecasting the Future and Understanding the Past*, ser. Reading, MA: Addison-Wesley, 1994.

[92] T. Gautama, D. P. Mandic, and M. M. V. Hulle, "The delay vector variance method for detecting determinism and nonlinearity in time series," *Physica D: Nonlinear Phenomena*, vol. 190, no. 3-4, pp. 167–176, Apr. 2004.

[93] D. P. Mandic, M. Chen, T. Gautama, M. M. V. Hulle, and A. Constantinides, "On the characterization of the deterministic/stochastic and linear/nonlinear nature of time series," *Proceedings of the Royal Society A: Mathematical, Physical and Engineering Sciences*, vol. 464, no. 2093, pp. 1141–1160, 2008.

[94] C. J. Keylock, "Improved preservation of autocorrelative structure in surrogate data using an initial wavelet step," *Nonlinear Processes in Geophysics*, vol. 15, no. 3, pp. 435–444, Jun. 2008.

[95] D. B. Percival and A. T. Walden, *Wavelet Methods for Time Series Analysis (Cambridge Series in Statistical and Probabilistic Mathematics)*. Cambridge University Press, Feb. 2000.

[96] C. Tao and J. J. Jiang, "Chaotic component obscured by strong periodicity in voice production system," *Physical Review E*, vol. 77, p. 061922, Jun 2008.

[97] R. Miralles, L. Vergara, A. Salazar, and J. Igual, "Blind detection of nonlinearities in multiple-echo ultrasonic signals," *IEEE Transactions on Ultrasonics, Ferroelectrics, and Frequency Control*, vol. 55,3, pp. 1–11, March 2008.

[98] M. Thiel, M. C. Romano, J. Kurths, M. Rolfs, and R. Kliegl, "Twin surrogates to test for complex synchronisation," *Europhysics Letters*, vol. 75, no. 4, pp. 535–541, August 2006.

[99] M. C. Romano, M. Thiel, J. Kurths, K. Mergenthaler, and R. Engbert, "Hypothesis test for synchronization: Twin surrogates revisited," *Chaos*, vol. 19, no. 1, p. 015108, 2009.

[100] M. T. Rosenstein, J. J. Collins, and C. J. D. Luca, "A practical method for calculating largest Lyapunov exponents from small data sets," *Physica D: Nonlinear Phenomena*, vol. 65, no. 1-2, pp. 117–134, May 1993.

[101] P. Grassberger and I. Procaccia, "Measuring the strangeness of strange attractors," *Physica D: Nonlinear Phenomena*, vol. 9, no. 1-2, pp. 189–208, Oct. 1983.

[102] J. Theiler and D. Prichard, "Constrained-realization Monte-Carlo method for hypothesis testing," *Physica D: Nonlinear Phenomena*, vol. 94, no. 4, pp. 221 – 235, 1996.

[103] T. Riede, *Vocal changes in animals during disorders*, ser. PhD. report. Mathematisch-Naturwissenschaftlichen Fakultat I der Humboldt-Universitat zu Berlin, 2000.

[104] T. Riede, H. Herzel, K. Hammerschmidt, L. Brunnberg, and G. Tembrock, "The harmonic-to-noise ratio applied to dog barks," *The Journal of the Acoustical Society of America*, vol. 110, no. 4, 2001.

[105] T. Riede, B. R. Mitchell, I. Tokuda, and M. J. Owren, "Characterizing noise in nonhuman vocalizations: Acoustic analysis and human perception of barks by coyotes and dogs," *The Journal of the Acoustical Society of America*, vol. 118, no. 1, 2005.

[106] R. A. Guyer and P. A. Johnson, "Nonlinear Mesoscopic Elasticity: Evidence for a New Class of Materials," *Physics Today*, vol. 52, no. 4, p. 30, 1999.

[107] K. R. McCall and R. A. Guyer, "Equation of state and wave propagation in hysteretic nonlinear elastic materials," *Journal of Geophysical Research: Solid Earth*, vol. 99, no. B12, pp. 23 887–23 897, 1994.

[108] M. Bentahar, H. El Aqra, R. El Guerjouma, M. Griffa, and M. Scalerandi, "Hysteretic elasticity in damaged concrete: Quantitative analysis of slow and fast dynamics," *Phys. Rev. B*, vol. 73, p. 014116, Jan 2006.

[109] P. A. Johnson, B. Zinszner, and P. N. Rasolofosaon, "Resonance and elastic nonlinear phenomena in rock," *Journal of Geophysical Research*, vol. 101, pp. 11–553, 1996.

[110] P. Delsanto and M. Scalerandi, "Modeling nonclassical nonlinearity, conditioning, and slow dynamics effects in mesoscopic elastic materials," *Physical Review B*, vol. 68, no. 6, pp. 1–9, 2003.

[111] K. Van Den Abeele, J. Carmeliet, J. A. Ten Cate, and P. Johnson, "Nonlinear ElasticWave Spectroscopy (NEWS) Techniques to Discern Material Damage, Part I: Nonlinear Wave Modulation Spectroscopy (NWMS)," *Research in Nondestructive Evaluation*, vol. 12, no. 1, pp. 17–30, 2000.

[112] J. Jin, M. G. Moreno, J. Riviere, and P. Shokouhi, "Impact-based nonlinear acoustic testing for characterizing distributed damage in concrete," *Journal of Nondestructive Evaluation*, vol. 36, no. 3, p. 51, Jun 2017.

[113] K. Van Den Abeele, P. A. Johnson, and A. Sutin, "Nonlinear Elastic Wave Spectroscopy (NEWS) Techniques to Discern Material Damage, Part II: Single-Mode Nonlinear Resonance Acoustic Spectroscopy," *Research in Nondestructive Evaluation*, vol. 12, no. 1, pp. 17–30, 2000.

[114] K. Van Den Abeele, P. Y. Le Bas, B. Van Damme, and T. Katkowski, "Quantification of material nonlinearity in relation to microdamage density using nonlinear reverberation spectroscopy: Experimental and theoretical study." *The Journal of the Acoustical Society of America*, vol. 126, no. 3, pp. 963–72, 2009.

[115] C. Payan, V. Garnier, J. Moysan, and P. A. Johnson, "Applying nonlinear resonant ultrasound spectroscopy to improving thermal damage assessment in concrete," *The Journal of the Acoustical Society of America*, vol. 121, no. 4, p. EL125, 2007.

[116] C. Payan, T. J. Ulrich, P. Y. Le Bas, T. Saleh, and M. Guimaraes, "Quantitative linear and nonlinear resonance inspection techniques and analysis for material characterization: Application to concrete thermal damage." *The Journal of the Acoustical Society of America*, vol. 136, no. 2, p. 537, 2014.

[117] G. J. Kim, S. J. Park, and H. G. Kwak, "Experimental characterization of ultrasonic nonlinearity in concrete under cyclic change of prestressing force using Nonlinear Resonant Ultrasonic Spectroscopy," *Construction and Building Materials*, vol. 157, pp. 700–707, 2017.

[118] S. J. Park, G. J. Kim, and H. G. Kwak, "Characterization of stress-dependent ultrasonic nonlinearity variation in concrete under cyclic loading using nonlinear resonant ultrasonic method," *Construction and Building Materials*, vol. 145, pp. 272–282, 2017.

[119] J. Chen, A. R. Jayapalan, J. Y. Kim, K. E. Kurtis, and L. J. Jacobs, "Rapid evaluation of alkali–silica reactivity of aggregates using a nonlinear resonance spectroscopy technique," *Cement and Concrete Research*, vol. 40, no. 6, pp. 914–923, jun 2010.

[120] K. J. Leśnicki, J. Y. Kim, K. E. Kurtis, and L. J. Jacobs, "Characterization of ASR damage in concrete using nonlinear impact resonance acoustic spectroscopy technique," *NDT & E International*, vol. 44, no. 8, pp. 721–727, dec 2011.

[121] V. Genovés, L. Soriano, M. V. Borrachero, J. Eiras, and J. Payá, "Preliminary study on short-term sulphate attack evaluation by nonlinear impact resonance acoustic spectroscopy technique," *Construction and Building Materials*, vol. 78, pp. 295–302, 2015.

[122] J. N. Eiras, J. Monzó, J. Payá, T. Kundu, and J. S. Popovics, "Nonclassical nonlinear feature extraction from standard resonance vibration data for damage detection," *The Journal of the Acoustical Society of America*, vol. 135, no. 2, pp. EL82–EL87, 2014.

[123] U. Dahlen, N. Ryden, and A. Jakobsson, "Damage identification in concrete using impact non-linear reverberation spectroscopy," *NDT & E International*, vol. 75, pp. 15–25, 2015.

[124] L. Cohen, *Time-frequency analysis*. Prentice Hall, 1995, vol. 778.

[125] S. J. Park, H. J. Yim, and H. G. Kwak, "Nonlinear resonance vibration method to estimate the damage level on heat-exposed concrete," *Fire Safety Journal*, vol. 69, pp. 36–42, 2014.

[126] M. Scalerandi, M. Bentahar, and C. Mechri, "Conditioning and elastic nonlinearity in concrete: Separation of damping and phase contributions," *Construction and Building Materials*, vol. 161, pp. 208–220, 2018.

[127] J. A. TenCate, E. Smith, and R. A. Guyer, "Universal slow dynamics in granular solids," *Physical Review Letters*, vol. 85, no. 5, p. 1020, 2000.